New Methods for the Calculation of Dynamical Properties of Many-Particle Systems

by

Kyeongjae Cho
M.Sc., Seoul National University
B.Sc., Seoul National University

Submitted to the Department of Physics
in partial fulfillment of the requirements for the degree of

Doctor of Philosophy

at the

MASSACHUSETTS INSTITUTE OF TECHNOLOGY

May 1994

Author .....
Department of Physics
April 11, 1994

Certified by .....
John D. Joannopoulos
Professor of Physics
Thesis Supervisor

Accepted by .....
George F. Koster
Chairman, Departmental Committee on Graduate Students

New Methods for the Calculation of Dynamical Properties of Many-Particle Systems

by

Kyeongjae Cho

M.Sc., Seoul National University

B.Sc., Seoul National University

Submitted to the Department of Physics
on April 11, 1994, in partial fulfillment of the
requirements for the degree of
Doctor of Philosophy

Abstract

The main theme of my thesis research is to develop computational tools to solve the Schrödinger equation for the many-particle system of nuclei and electrons and apply them to the *first principles* study of condensed matter systems. From the beginning, I introduce the adiabatic (Born-Oppenheimer) approximation to separate the many-particle system into the problem of classical dynamics of nuclei and the problem of the inhomogeneous electron fluid in the static ionic potential. The Newton equation describes the dynamics of nuclei, and the Schrödinger equation describes the electrons as an interacting quantum system.

First, I study the computational techniques for solving both the Newton equation and the Schrödinger equation. For the Newton equation, I investigate the erogdicity and the dynamical properties of the constant-temperature molecular dynamics which was introduced to generate a canonical ensemble instead of a microcanonical ensemble of the conventional molecular dynamics. I also study the constant-temperature molecular dynamics with the momentum conservation.

For the Schrödinger equation, I use the density functional theory which reduces the system of interacting electrons to a system of non-interacting electrons (or Kohn-Sham orbitals) in an effective potential. I introduce the *wavelet* basis for an efficient representation of the Kohn-Sham orbitals which are conventionally represented either by local atomic orbitals or by the plane wave basis.

Second, I apply the computational techniques to the first principles study of the semiconductor surfaces. For the Si(100) surface, I investigate tip-surface interactions in the scanning tunneling microscopy (STM) and the atomic force microscopy (AFM). The STM study leads to a new understanding of the microscopic STM measurement process. The AFM study leads to a discovery of the mechanical hysteresis effect at an atomic scale and the microplastic deformation of the Si(100) surface. I propose to

apply the plastic deformation to make an ultra-high density memory device. I also examine the intrinsic dynamical properties of the Si(100) surface at finite temperature and the phase of the vicinal Si(100) surface structure under external strain. For the Si(113) surface, I calculate the surface energy of the (3×1) reconstruction and show that its stability is intrinsic.

Thesis Supervisor: John D. Joannopoulos
Title: Professor of Physics

Acknowledgments

I wish to express my sincere appreciation to Professor John Joannopoulos for what he has given me during my thesis research. John has given me much of his valuable time as well as financial support. In addition, I was able to learn from John many academic skills encompassing reading, writing, presentation, and publication skills. I was very fortunate to have an advisor who knows how to bring out the best out of a person.

I also appreciate Tomás' help in learning many valuable programming skills, Bob in using the Macintosh, Andy in understanding pseudopotentials, Karl and Brond in programming on CM-2 and CM-5. I have enjoyed working with Tomás, Bob, Oscar, Rodrigo, Karl, Brond, Professor Leonard Kleinman, Professor Pui K. Lam, and I have high expectations in working with Professor E. Kaxiras, Professor H. Lim, Ickjin, Shanhui, and Pierre. I have benefited from the discussions with Marcelo, Professor S. Nosé, Professor S. G. J. Mochrie, Dr. D. L. Abernathy, and Dr. D. J. Chadi.

I wish to thank the CMT secretary Imadiel and the consultants of MIT Cray XMP, San Diego Supercomputing Center, Pittsburgh Supercomputing Center, and MIT CM-5 for their help. My thanks to the Korean Government Overseas Scholarship, Moojin Science and Technology Schlarship Foundation, and MIT Industrial Liason Fellowship for their financial support.

I am deeply indebted to my parents. Without their understanding, love, and sacrifice, my academic career would not have been possible. I also appreciate the love and understanding of Jiweon. She has provided great support and critical stimuli for improving myself. I thank my parent-in-laws for their emotional support.

Finally, I thank Professor A. Nihat Berker and Professor Barton Zwiebach for their critical reading and thoughtful questions on this thesis.

Contents

List of Figures

List of Tables

Chapter 1

Introduction

The rapid development of the electronic computers in these days provides a very powerful tool for quantitative investigations of science and engineering problems. The increasing computation power allows the scientists and engineers to study increasingly more complicated systems which could not be studied quantitatively within the conventional analytic approach since the fundamental equations for the systems are generally too difficult to solve analytically.

The fundamental equations for most condensed matter systems are the Newton equation for classical particles [1], the Schrödinger equation for nonrelativistic electrons [2], and the Maxwell equations for electromagnetic waves [3]. These three equations, in principle, provide the microscopic descriptions of a wide range of condensed matter systems including the chemical systems and the biological systems. In fact, the conventional division of science into separate fields such as physics, chemistry, biology, or geology does not represent a fundamental difference from a microscopic point of view since the above three fundamental equations apply equally to all the fields of science. However, it should be emphasized that most chemical, biological, or geological systems are too large and complex for a first principles investigation based on the current computational power. Nevertheless, first principles investigations can provide an understanding of the microscopic processes in chemical, biological, or geological phenomena, complement the current knowledge in each field, and lead to a unified quantitative and microscopic description of natural phenomena in the future.

The computational study of these fundamental equations and many phenomenological equations derived from them are based on the *finite difference calculus* just as the conventional analytic approach is based on the differential calculus. Since most equations are differential equations, it is very important to construct finite difference equations which faithfully represent the original differential equations. Once the difference equations are constructed, one has a finite number of variables and can develop computer programs to solve them [4]. Therefore, the efficient representations of the equations with smaller number of variables and the efficient methods of solving the difference equations become very important for practical computational problems.

In this thesis, I will focus on the computational techniques for the Newton equation and the Schrödinger equation, and the computational study of the semiconductor surface problems. In the following sections, I briefly review the basic techniques used for the study of the Newton equation and the Schrödinger equation, and introduce to the surface problems.

1.1 Newton Equation

For a given N-particle system, the Newton equation is a second order differential equation,

$$m_i \frac{d^2}{dt^2} \mathbf{r}_i = \mathbf{f}_i. \tag{1.1}$$

For a conservative potential system, the force $\mathbf{f}_i$ is derived from the interaction potential $V(\{\mathbf{r}_i\})$ as

$$\mathbf{f}_i = -\nabla V(\{\mathbf{r}_i\}), \tag{1.2}$$

and generally it is impossible to generate an exact trajectory of the system as a function of time starting from a given initial condition. However, this impossibility is not caused by the limitation of the computational techniques, but by the intrinsic chaotic nature of the many-particle systems. Therefore, in a computational study one

generates a physically meaningful trajectory instead of an exact trajectory, and this generation is achieved by keeping the conservative quantities (the total energy, the total momentum, and the total angular momentum) constant during the simulations.

In order to solve the Newton equation, one transforms the equation into a finite difference equation with an introduction of a finite timestep δt and generates a discrete time trajectory through the finite difference equation. The general procedure is to calculate the quantities at $(n+1)$th timestep $\{\mathbf{r}_i(n+1),\ \mathbf{v}_i(n+1),$ and $\mathbf{f}_i(n+1)\}$ from the quantities at nth timestep $\{\mathbf{r}_i(n),\ \mathbf{v}_i(n),$ and $\mathbf{f}_i(n)\}$. For this procedure, the Verlet algorithm and the Gear predictor-corrector algorithm are generally used in the molecular dynamics simulations [1].

From the discrete time trajectory, one obtains a sequence of the states of the N-particle system, $\{\mathbf{r}_i(n),\ \mathbf{v}_i(n)\}$, which is a sequence of points in 6N dimensional configurational space, and these points are on the microcanonical ensemble surface in the configurational space. If the N-particle system is ergodic, then the discrete time trajectory corresponds to a discrete sampling of the microcanonical ensemble of the N-particle system, and one can calculate thermodynamic quantities from the sampling. If the N-particle system is not ergodic, then the discrete time trajectory represents a physical trajectory of the system within a subset of the microcanonical ensemble surface.

Because of the difficulties of calculating thermodynamic quantities in a microcanonical ensemble, many new techniques have been developed to generalize the discrete time sampling for various ensembles of statistical mechanics. Specifically, many techniques are available for the canonical ensemble sampling, and the *extended system* method is one of the most widely used method [5, 6, 7]. The extended system method introduces a dynamic variable to represent the physical heat reservoir, and the Nosé theorem guarantees the exact canonical ensemble sampling for an ergodic extended system.

1.2 Schrödinger Equation

For most practical purposes, the Schrödinger equation is the fundamental equation of condensed matter systems. In principle, the solutions of the Schrödinger equation should be able to explain the diverse phenomena in physics, chemistry, and biology: however, in most cases the system under consideration contains extremely large number of atoms which are clusters of nuclei and electrons themselves, and consequently solving the corresponding Schrödinger equation for the nuclei and the electrons is extremely difficult. Because of this difficulty, one can simply approach the problem of many-particle systems from a phenomenological viewpoint. In this approach, the atoms are regarded as point particles rather than as clusters of nuclei and electrons, and the interaction between the point particles is a classical potential and determined from the parameter fitting to experimental data. Hence, all the quantum mechanical effects are reduced to the experimentally fitted classical potential parameters, and the many-particle systems are studied with the Newton equation as we discussed in the previous section.

However, the classical potential description of the many-particle systems has a limited range of validity corresponding to experimental data used for the parameter fitting, and under the environment beyond this range the classical potential cannot provide an accurate description. This situation corresponds to the breakdown of the assumption that the atoms can be regarded as a point particle with an effective interaction between them derived from the interactions between two clusters of particles. Therefore, in order to study the many-particle systems in most general situation, one has to treat an atom as a cluster of nucleus and electrons which are described by the Schrödinger equation.

Generally, one atom has many electrons so that the quantum mechanical study of a single atom is already a very complicated many-particle problem. The complexity of the problem comes from the difficulty of solving the many-electron wave function of an atom. Consequently, the quantum mechanical study of a many-atom system becomes extremely complicated, and it is not practical to solve the problem for the

most general situation. One can rather solve the problem with several simplifying approximations which are accurate within a wide range of applications.

The most important approximation is the adiabatic approximation (or the Born-Oppenheimer approximation) which assumes that the nuclei are classical point particles and the electrons are described by the Schrödinger equation within the external potential of the nuclei. In this approximation, the electronic degrees of freedom are decoupled from the ionic degrees of freedom and adiabatically follow the change of the ionic positions.

Another frequently used approximation is the pseudopotential approximation which combines the core electrons of an atom with the nuclei to form an *ion*. The interaction between an ion and valence electrons are described by the pseudopotential, and the interaction between ions is a static Coulomb potential. Therefore, a neutral N-atom system has N ions with charge $z_\alpha e$ and $N_e = \sum_\alpha z_\alpha$ electrons, and the Hamiltonian for the system is

$$\hat{H}(\{\mathbf{R}_\alpha\}) = \sum_i \frac{\mathbf{p}_i^2}{2m} + \sum_{i>j} \frac{e^2}{|\mathbf{r}_i - \mathbf{r}_j|} - \sum_{i,\alpha} \frac{e^2 z_\alpha}{|\mathbf{r}_i - \mathbf{R}_\alpha|} + \sum_{\alpha,\beta} \frac{e^2 z_\alpha z_\beta}{|\mathbf{R}_\alpha - \mathbf{R}_\beta|}, \qquad (1.3)$$

and the Schrödinger equation is $\hat{H}\Psi = E\Psi$ where Ψ is the electron wave function.

Even though the complexity of the problem is greatly reduced by the Born-Oppenheimer approximation and the pseudopotential approximation, the remaining problem is still very difficult to study since the electron wave function Ψ is a complex function of N_e electron variables. In order to overcome this difficulty, the density functional theory (DFT) is introduced which proves that there is a one-to-one correspondence between the electron density $n(\mathbf{r})$ and the external ionic potential, and consequently there is a one-to-one correspondence between the electron density $n(\mathbf{r})$ and the electron wave function Ψ. Furthermore, in the DFT the electron ground state can be reached variationally in the general electron density functional space so that the problem of finding the electron ground state reduces to the minimization problem in the electron density functional space.

The energy functional $E[n(\mathbf{r})] = < \Psi|\hat{H}|\Psi >$ can be divided into five terms: the

non-interacting electron kinetic energy term, the static electron-electron interaction term (Hartree term), the electron-ion interaction term, the ion-ion interaction term (Ewald term), and the exchange-correlation term. Within this formulation of the DFT, the ground state energy functional is obtained as the ground state of N_e non-interacting electron system in the effective potential generated from the Hartree term, the electron-ion interaction term, and the exchange-correlation term.

The non-interacting electron wave functions (Kohn-Sham orbitals) are described by a self-consistent equation (Kohn-Sham equation) [1] , and only the total electron density and the total ground state energy are physically meaningful quantities in a strict sense. However, these quantities already contain enough information to calculate many physical and chemical properties such as the equilibrium lattice constants, the bulk moduli, the ground state geometric and electronic structures of the surfaces and the interfaces, the dynamical evolution of the geometric and electronic structures, and so forth.

1.3 Surface Problems

The surface of an N-atom condensed matter system has approximately $N^{\frac{2}{3}}$ surface atoms, and for the calculation of the bulk properties the surface effects can be safely neglected since the surface contribution is $N^{-\frac{1}{3}}$ smaller. However, a surface itself is a many-particle system which generally has a quite different structure from the underlying bulk, and the study of surface structure is necessary for a full understanding of any finite condensed matter system.

In the study of a surface problem, one is generally interested in both the intrinsic properties and extrinsic properties of the surface. For the intrinsic properties, one studies the reconstruction and the relaxation of the surface structure from the bulk structure. One also studies the dynamical properties of the surface such as the surface phonons and the surface self-diffusion.

[1] The efficient representation of Kohn-Sham orbitals is an important step for the implementation of the many-body problem as a finite dimensional matrix equation [8, 9, 10].

For the extrinsic properties, one studies the structures added to the intrinsic surface such as surface defects (both point defects and line defects) and surface adatoms[2]. A surface defect can be an isolated defect on a surface or a termination of bulk defects (for example, dislocations or grain boundaries) at the surface. The structure of surface defects and adatoms and their dynamical behaviors at finite temperature are very complicated problems, and the study of these is important for understanding the microscopic processes of material fabrications and the surface chemical processes such as the catalysis.

The experimental tools for studying the surface phenomena are probes which are sensitive only to the surface. Most of the tools such as the X-ray diffraction[3] or the low energy energy diffraction probe an average property of a surface rather than a local property of a surface. The scanning microscopes provide an surface image with atomic resolution, and the interpretation of this image is crucial for the understanding of the microscopic processes on the surface [18, 19, 20].

1.4 Organization of Thesis

The main body of the thesis is divided into two parts, the part of the new techniques and the part of the application to surface problems. The first part includes Chapters 2, 3, and 4, and the second part includes Chapters 5, 6, 7, 8, 9, and 10.

In the first part, I discuss the techniques for the classical molecular dynamics (Chapters 2 and 3) and the wavelet basis for the electron wave functions (Chapter 4). In Chapter 2, I perform a detailed investigation of the equilibrium and dynamical properties of the constant-temperature molecular dynamics [5, 6]. In Chapter 3, I extend and test the constant-temperature molecular dynamics with the momentum conservation [7]. In Chapter 4, I introduce the wavelet basis in the electronic structure calculations, and apply to the calculation of hydrogen atom, 1s core states of hydrogen

[2]For example, the interaction between an anticite bulk defect and the GaAs(110) surface shows how the interaction changes the properties of the defect and the surface [11]

[3]The microscopic many-body processes in the X-ray photoemission experiment complicate the interpretation of the experimental data [12, 14].

to uranium, and hydrogen molecule ion [8, 9].

In the second part, I discuss the tip-surface interactions in scanning microscopy (Chapters 5, 6, and 7) [15, 16, 17], the properties of the Si(100) surface (Chapters 8 and 9), and the structure of the Si(113) surface (Chapter 10). In Chapter 5, I discuss the tip-surface interactions in scanning tunneling microscopy (STM) experiment, and investigate the microscopic process of an STM measurement [18]. In Chapter 6, I discuss the tip-induced mechanical hysteresis which is predicted to be present at low temperature atomic force microscopy (AFM) experiment [19]. In Chapter 7, I discuss the tip-induced microplastic deformation of the Si(100) surface and its application to an ultra-high density memory device [20, 21]. In Chapter 8, I perform an ab inito dynamics simulation of the Si(100) surface, and discuss the dynamical properties of the surface structure [22]. In Chapter 9, I discuss the macroscopic phases of the vicinal Si(100) surface under external strain [23]. In Chapter 10, I discuss the stability of the Si(113) surface, and show that its stability is intrinsic [24].

In the last chapter, I discuss the future development of the research both in the computational techniques and in the applications to condensed matter systems.

Chapter 2

Ergodicity and Dynamical Properties of Constant-Temperature Molecular Dynamics

The assumption of ergodicity in Nosé's original formulation of the constant temperature molecular dynamics is tested for a Lennard-Jones potential system. With the performance of very long simulations, it is shown that the extended system of a Lennard-Jones potential system is ergodic for all values of thermostat parameters tested. It is also shown, however, that the rate of convergence to the canonical ensemble strongly depends on the value of thermostat effective mass, Q. The dynamical properties of the extended system are also studied using the velocity autocorrelation function and the power spectral density. From the analysis of the simulations, it is found that the dynamical properties are *not* correctly represented for arbitrary values of thermostat parameters. A prescription and a set of quantitative criteria are introduced to generate physically meaningful dynamics. Thus, the results of this work show that with a special choice of thermostat parameters it is possible to obtain *both* the correct canonical ensemble and physically meaningful dynamical behavior of the physical system.

2.1 Introduction

Molecular Dynamics(MD) is a very versatile simulation method because it generates physically meaningful trajectories [1]. Thus, in addition to describing equilibrium properties, MD can be used to study non-equilibrium processes and dynamical behavior in general. However, the fact that conventional MD generates a microcanonical ensemble instead of a canonical ensemble makes MD inappropriate for simulations of small physical systems. In a simulation, it is physically reasonable to assume that a small physical system is embedded in a larger physical system, so it satisfies a canonical ensemble. For this reason, there have been many efforts to devise methods to perform constant temperature or constant pressure MD simulations in place of constant energy or constant volume MD simulations [1, 25, 84, 27, 28, 29]. One of the most widely used constant temperature or constant pressure MD simulation methods is the Extended System Method (ESM) [30, 31, 32, 33, 34].

The ESM introduces an additional dynamical variable to represent a heat reservoir or a pressure reservoir. It has been proved that the constant temperature ESM (which is the method we shall focus on in this paper) generates a canonical ensemble *if* the extended system including the additional variable is *ergodic* [32]. However, it is well known that the ESM exhibits unphysical behavior in many cases. The sources of this behavior are thought to be the extremely long relaxation time to get a typical canonical ensemble state from an extremely nontypical initial state, or the nonergodicity of an extended system for extremely small or large values of the thermostat effective mass, Q [1]. Even if the extended system is ergodic with a short relaxation time, it is not clear whether the extended system can describe the correct *dynamical* behavior of the original system. Thus it is important to determine whether this is indeed possible, or to what extent it is possible, and to determine the thermostat parameters that are responsible for the correct dynamical behavior.

In this paper, we perform very long simulations which demonstrate that an extended system with a Lennard-Jones potential (or the extended LJ system) is ergodic for any value of the thermostat effective mass, Q. We also establish the fact that

the ensemble average value of the thermostat variable, $< s >$, plays a crucial role to obtain physically meaningful dynamics within the virtual variable formalism of the ESM.

This paper is organized in the following way: In section II, we review the constant temperature ESM of Nosé. In section III, we study the ergodicity of the ESM. In section IV, we study the dynamical properties of the extended LJ system, and introduce the criteria needed to obtain meaningful results out of an ESM simulation. Finally in section V, we summarize and present concluding remarks.

2.2 Constant Temperature Extended System Method

In this section, we review the original formulation of Nosé's constant temperature MD [32, 33, 34], and derive the equations of motion which are used in the simulations. We also review the relationship of the original formulation with two equivalent formulations: the real variable formalism and the Nosé-Hoover friction variable formalism.

We begin with a description of the construction of the extended system (ES) Hamiltonian, H_{ES}, from a Hamiltonian of a physical system, H_0. First, one expresses H_0 in terms of its real canonical variables, the canonical coordinates $\mathbf{r}_i'$, and the canonical momenta $\mathbf{p}_i'$, as follows:

$$H_0(\mathbf{r}_i', \mathbf{p}_i') = \sum_{i=1}^{N} \frac{\mathbf{p}_i'^2}{2m_i} + \phi(\{\mathbf{r}_i'\}). \tag{2.1}$$

Second, one introduces the thermostat variable s and the conjugate momentum P_s. Now, the thermostat Hamiltonian is the following:

$$H_s = \frac{P_s^2}{2Q} + gk_BT_{ext}ln(s), \tag{2.2}$$

where $g = 3N + 1$, and T_{ext} is the externally set temperature. Up to this point, there is no coupling between H_0 and H_s. Finally, to couple the thermostat to the physical system, one introduces a new set of canonical variables $\mathbf{r}_i$ and $\mathbf{p}_i$, which are

the virtual variables, as follows:

$$\begin{aligned} \mathbf{p}_i' &= \frac{\mathbf{p}_i}{s} \\ \mathbf{r}_i' &= \mathbf{r}_i. \end{aligned} \tag{2.3}$$

Then, the ES Hamiltonian is expressed in terms of its own canonical variables as follows:

$$\begin{aligned} H_{ES}(\mathbf{r}_i, \mathbf{p}_i, s, P_s) &= H_0(\mathbf{r}_i, \frac{\mathbf{p}_i}{s}) + H_s(s, P_s) \\ &= \sum_{i=1}^{N} \frac{\mathbf{p}_i^2}{2m_i s^2} + \phi(\{\mathbf{r}_i\}) + \frac{P_s^2}{2Q} + g k_B T_{ext} ln(s). \end{aligned} \tag{2.4}$$

From this Hamiltonian, one can get the following set of Hamilton's equations:

$$\frac{d\mathbf{r}_i}{dt} = \frac{\mathbf{p}_i}{ms^2} \tag{2.5}$$

$$\frac{d\mathbf{p}_i}{dt} = -\nabla_i \phi \tag{2.6}$$

$$\frac{ds}{dt} = \frac{P_s}{Q} \tag{2.7}$$

$$\frac{dP_s}{dt} = \sum_{i=1}^{N} \frac{\mathbf{p}_i^2}{ms^3} - g k_B T_{ext} \frac{1}{s}. \tag{2.8}$$

By combining these equations, one is led to the following equations of motion for $\mathbf{r}_i$ and s:

$$\frac{d^2\mathbf{r}_i}{dt^2} = -\frac{1}{ms^2}\nabla_i \phi - 2\frac{1}{s}\frac{ds}{dt}\frac{d\mathbf{r}_i}{dt} \tag{2.9}$$

$$\frac{d^2 s}{dt^2} = \frac{1}{Q}\sum_{i=1}^{N} sm(\frac{d\mathbf{r}_i}{dt})^2 - \frac{g k_B T_{ext}}{Q}\frac{1}{s}. \tag{2.10}$$

By solving these two equations of motion using the standard MD technique, one can generate a sequence of states of the physical system at each time step. The collection of these states constitutes a canonical ensemble if the ES is *ergodic*. This method of generating a sequence of physical states is called the virtual variable formalism of the ESM.

On the other hand, one can generate physical states using the real variables by replacing the virtual variables in the equations of motion by the real variables as follows [34]:

$$\begin{aligned} \mathbf{p}_i' &= \frac{\mathbf{p}_i}{s} \\ \mathbf{r}_i' &= \mathbf{r}_i \\ P_s' &= \frac{P_s}{s} \\ s' &= s. \\ dt' &= \frac{dt}{s} \end{aligned} \tag{2.11}$$

The equations of motion are now expressed as follows in terms of the real variables:

$$\frac{d^2\mathbf{r}_i'}{dt'^2} = -\frac{1}{m}\nabla_i\phi - \frac{1}{s'}\frac{ds'}{dt'}\frac{d\mathbf{r}_i'}{dt'} \tag{2.12}$$

$$\frac{d^2s'}{dt'^2} = \frac{s'}{Q}[\sum_{i=1}^{N} m(\frac{d\mathbf{r}_i'}{dt'})^2 - gk_BT_{ext}] + \frac{1}{s'}(\frac{ds'}{dt'})^2, \tag{2.13}$$

where $g = 3N$.

These equations can also be expressed in the Nosé-Hoover form [35] by introducing the Nosé-Hoover friction variable ζ:

$$\zeta = \frac{1}{s'}\frac{ds'}{dt'}.$$

Then the Nosé-Hoover equations of motion are the following:

$$\frac{d^2\mathbf{r}_i'}{dt'^2} = -\frac{1}{m}\nabla_i\phi - \zeta\frac{d\mathbf{r}_i'}{dt'} \tag{2.14}$$

$$\frac{d\zeta}{dt'} = \frac{1}{Q}[\sum_{i=1}^{N} m(\frac{d\mathbf{r}_i'}{dt'})^2 - gk_BT_{ext}] \tag{2.15}$$

The relationships among these three equivalent methods of performing a ESM simulation are summarized in Figure 2-1. The virtual variable formalism is also known as the Hamiltonian formalism, whereas the real variable formalism and Nosé-Hoover form are known as the non-Hamiltonian formalism. In the non-Hamiltonian formal-

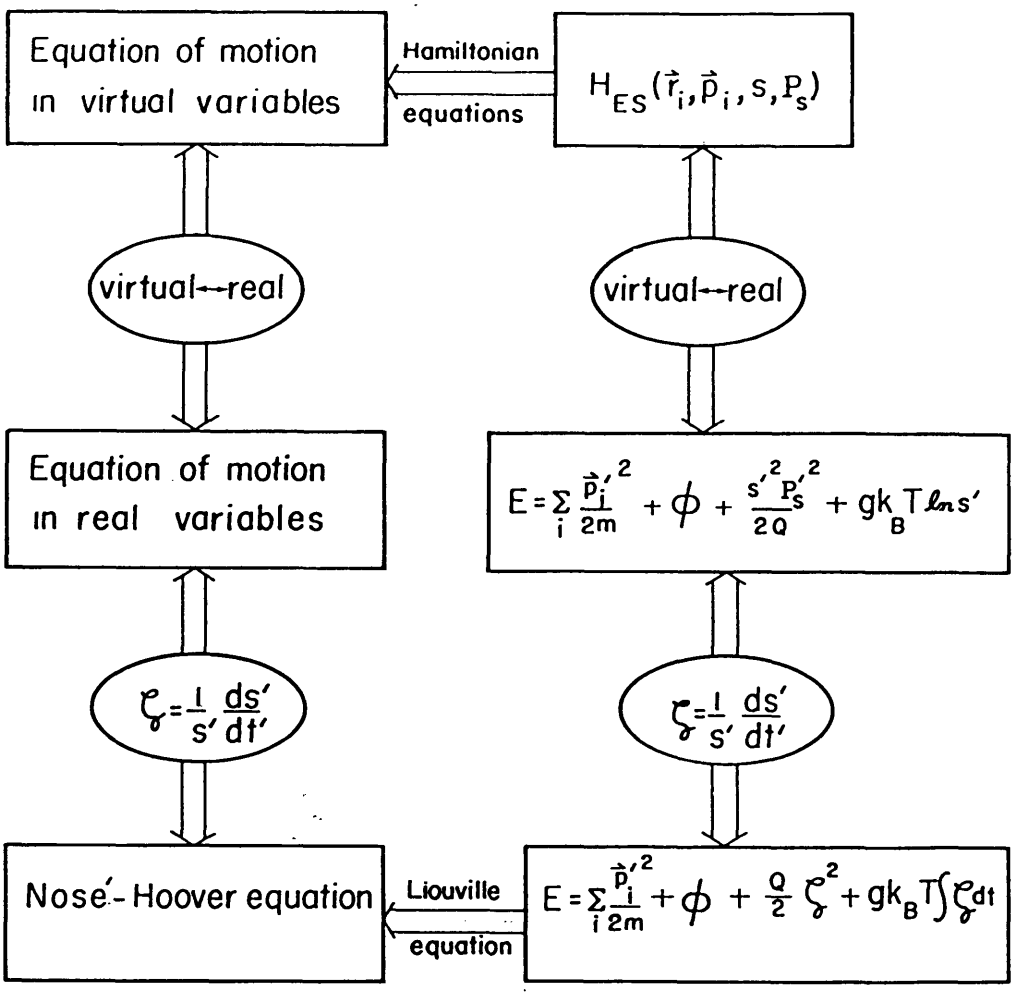

Figure 2-1: Schematic diagram which explains the relationship of the virtual variable formalism, the real variable formalism and the Nosé-Hoover formalism. These three formalisms are related to each other by the change of variables indicated.

ism, the equation of motion cannot be derived from the conserved energy. However, the Nosé-Hoover equations can be derived as a Liouville equation by applying the Liouville theorem to the ESM [35]. This Nosé-Hoover form is easily generalized to include more than one friction variable [36].

Figure 2-1 shows that the ergodicity of the ES Hamiltonian enables both the Hamiltonian formalism and non-Hamiltonian formalism to generate a canonical ensemble. Therefore, the proof of the ergodicity of an ES Hamiltonian also guarantees that the Liouville equation generates a canonical ensemble.

2.3 Ergodicity of the Extended System

In the previous section it was stated that the ergodicity of the ES Hamiltonian is essential for the generation of a canonical ensemble. This ergodicity, however, is not automatically guaranteed even for the extended system of an *ergodic* physical system! The hard sphere potential system and single harmonic oscillator system [35] are examples that fall into this category. In this section, therefore, we perform a test of the ergodicity of the extended Lennard-Jones potential system. Our choice is motivated by the extensive use of the Lennard-Jones potentials in numerical simulations. We proceed in two steps. In part A, we review the original proof of obtaining the canonical ensemble for an ergodic extended system, and discuss the quantities that need to be calculated in order to test the ergodicity. In part B, we present the results of our simulations.

2.3.1 Theory

For any given physical system, one can construct a corresponding ES Hamiltonian following the procedure in section II. If the extended system is ergodic, the following theorem guarantees the generation of the canonical ensemble of H_0 starting from the microcanonical ensemble of H_{ES} [32]. The partition function of the extended system has the microcanonical ensemble form for an ergodic system:

$$Z = c \int d\mathbf{r}_i d\mathbf{p}_i \int ds dP_s \delta(H_{ES} - E). \tag{2.16}$$

Integration over s yields the partition function:

$$Z = c' \int d\mathbf{r}_i' d\mathbf{p}_i' e^{-\beta_{ext} H_0} \int dP_s e^{-\beta_{ext} \frac{P_s^2}{2Q}}, \tag{2.17}$$

where β_{ext} is the inverse of $k_B T_{ext}$. In this form the partition function is the product of two integrals of Boltzmann factors. Therefore, both the energy of the physical system and the thermostat kinetic energy satisfy canonical ensembles.

Even though this theorem has a general form that does not depend on the nature

of H_0, the ergodicity of ES does depend on it. For example, in the appendix we prove analytically that the extended hard sphere (HS) potential system is not ergodic even though the HS potential system itself is. Another example is the extended single harmonic oscillator (HO) system, which is known to be nonergodic even though the HO system itself is a non-mixing ergodic system [35]. Therefore, the ergodicity of an extended system needs to be tested for each physical system.

As shown in the appendix, the simulations of a HS system show a remarkable agreement between the average of the instantaneous temperature (or average temperature in short) and the externally set temperature, even though the ES is nonergodic. This indicates that correctness of the average temperature alone is not enough to guarantee the ergodicity of an extended system. So in order to test the ergodicity of an extended system, one needs to examine the higher moments of the distribution function.

The most obvious quantities are the higher moments of the instantaneous temperature fluctuations where the instantaneous temperature is defined as follows:

$$T = \frac{2}{3Nk_B}K. \tag{2.18}$$

The theorem also predicts that the kinetic energy of s will follow the canonical ensemble so that we can use the moments of the kinetic energy of s to test the ergodicity of ES. Both classes of fluctuations can be calculated analytically and compared with the results of simulations.

In particular, the analytic expressions of the moments of kinetic energy for a system with f degrees of freedom satisfying the canonical ensemble are the following:

$$< K > = \frac{f}{2}k_B T_{ext} \tag{2.19}$$

$$< K^2 >_c = \frac{f}{2}(k_B T_{ext})^2 \tag{2.20}$$

$$< K^3 >_c = f(k_B T_{ext})^3 \tag{2.21}$$

$$< K^4 >_c = \frac{f}{2}(\frac{3f}{2} + 6)(k_B T_{ext})^4 \tag{2.22}$$

$$< K^5 >_c = f(5f + 12)(k_B T_{ext})^5, \tag{2.23}$$

where K is the kinetic energy; $< \cdots >$ represents an ensemble average; and $< K^m >_c = < (K - < K >)^m >$.

The moments of temperature fluctuations are obtained by using $f = 3N$ and equation (3.3). The moments of the K_s fluctuations are obtained by using $f = 1$.

2.3.2 MD Simulations

In this section, the ergodicity of the extended Lennard-Jones system is tested using the virtual variable formalism. In the numerical simulations the reduced units of a LJ system are used, and the equations of motion are solved using the sixth order Gear predictor-corrector method[1] [1]. To eliminate boundary effects a periodic boundary condition is adapted, and to avoid self-interactions due to the long range interaction, the LJ potential is cut at r_c ($r_c = 2.5$). To compensate the cutoff effect, a long range correction is made by adding the average of the interaction beyond r_c. The precision of the calculation is monitored by preserving the Hamiltonian to $5 - 6$ significant figures.

The simulations are performed with different numbers of particles, and it is found that a test of ergodicity requires a very long simulation time, much more than the typical maximum simulation time of a few hundred thousand time steps. Since the number of physical states or configurations needed to generate a canonical ensemble increase exponentially as a function of particle number, it is essential to reduce the particle number to test the ergodicity of a system with a tractable simulation time. A choice of a 32 particle LJ system is made, with a simulation cell containing eight face centered cubic (fcc) lattice unit cells in the solid phase and a maximum simulation time of 8×10^6 time steps.

Even though the initial conditions of each simulation are slightly different from each other, they all begin with a fcc lattice structure and initial velocities that are randomly assigned with a given mean value determined by T_{ext}. Initially the system

[1]This algorithm is non-symplectic and can cause irreversible drifts in some instances. To assure that this was not occurring in certain quantities that are calculated, additional calculations were performed using the symplectic leap-frog algorithm.

is annealed for $1000 - 3000$ time steps using the velocity rescaling technique. Here, the externally set temperature is used to rescale the velocities.

Other important initial conditions are the initial values of the thermostat s and the thermostat velocity. Both initial values of thermostat and thermostat velocity are chosen to be 1. The value of the thermostat effective mass, Q, is chosen to vary between 0.01 and 50. The size of the time step is adjusted so that the simulation is stable for given simulation parameters. By choosing a different simulation cell size and temperature, simulations are done for various phases of the LJ system.

In order to test the ergodicity of the extended LJ system, simulations are first done with 3×10^5 time steps with Q values equal to 0.01, 0.1, 1.0, 10, 30 and 50 for a liquid phase ($T_{ext} = 1.5, \rho = 0.8$). The first two moments of the kinetic energy of the LJ system and the first two moments of the kinetic energy of s are given in Table 2.1. The most striking result is the behavior of the average kinetic energy of s: even though its initial values vary from 0.005 to 25 depending on the value of Q, its average values after 3×10^5 time steps satisfy the equipartition theorem of the canonical ensemble with less than 20% deviation[2]. This result strongly indicates that the extended LJ system is *ergodic*. Table 2.1 also shows that as Q becomes either smaller than $O(1)$ or bigger than $O(1)$, the convergence to the canonical ensemble becomes worse. However, there is no abrupt change in the convergence which may indicate a transition from an ergodic system to a nonergodic system [34].

It is generally believed that for a very small Q an extended system does not equilibrate (the kinetic energy fluctuation is too small), and fast oscillations of the kinetic energy of a LJ system do not disappear [1] [34]. In our simulations for $Q = 0.01$, however, although rapid oscillations are observed over the entire run, we also find that the extended system appears to be equilibrating or converging to the canonical ensemble after 3×10^5 time steps (Table 2.1).

However, since there are still noticeable deviations (about 20%) from the prediction of the canonical ensemble, an extremely long simulation (8×10^6 time steps) is

[2]For the case of extended hard sphere potential system the kinetic energy of s does not satisfy the equipartition theorem.

Table 2.1: External temperatures T_{ext}^{cal} as calculated from the average temperature, the second moment of temperature fluctuation, the average kinetic energy of s, and the second moment of the kinetic energy fluctuation of s for the 32 particle extended LJ system in a fluid phase ($T_{ext} = 1.5, \rho = 0.8$). The number of time steps is 3×10^5, and the values in the parentheses are the temperatures obtained from an 8×10^6 time step simulation. The initial values are $T = T_{ext}$ and $K_s = \frac{Q}{2}$.

Q	T_{ext}^{cal} of $< T >$	T_{ext}^{cal} of $< T^2 >_c$	T_{ext}^{cal} of $< K_s >$	T_{ext}^{cal} of $< K_s^2 >_c$
0.01	1.4977 (1.5002)	1.6010 (1.4890)	1.7158 (1.4793)	1.742 (1.413)
0.1	1.4994	1.4970	1.5290	1.6600
1.0	1.5012	1.4746	1.4078	1.3010
10	1.4998	1.5280	1.5208	1.7317
30	1.4979	1.4740	1.3730	1.1430
50	1.4960	1.5930	1.6838	1.134

performed to test rigorously the ergodicity for $Q = 0.01$ (Table 2.2). Five moments of the instantaneous temperature and the kinetic energy of s are calculated. In Figure 2-2 we show the average temperature and the average kinetic energy of s as a function of time. We note that both are converging to their equipartition values with the largest error being in the average kinetic energy of s of less than 1.5% error. The fluctuations in temperature as a function of time are shown in Figure 2-3. These fluctuations are also found to be converging to their canonical ensemble values after about 2×10^6 time steps. However, the fluctuations of the kinetic energy of s, which are shown in Figure 2-4, do not exhibit the same rapid convergence to the canonical ensemble values, and in fact may appear to be diverging. We believe this latter interpretation is incorrect and that the convergence to the canonical ensemble values for the fluctuation of the kinetic energy is much slower. We are led to this conclusion by the comparison of the averages in Figure 2-2 which indicates clearly that the average kinetic energy of s converges *much* slower than the average temperature. Moreover, this overall slower convergence is very reasonable due to the small number of degrees of freedom (only one) associated with the kinetic energy of s.

There are two time scales that are important in understanding the relaxation to equilibrium of an extended system. One time scale is that associated with molecular collisions, t_{coll}, and the other time scale is a characteristic time associated with the thermostat variable s, t_s. For small Q the thermostat variable s changes very rapidly,

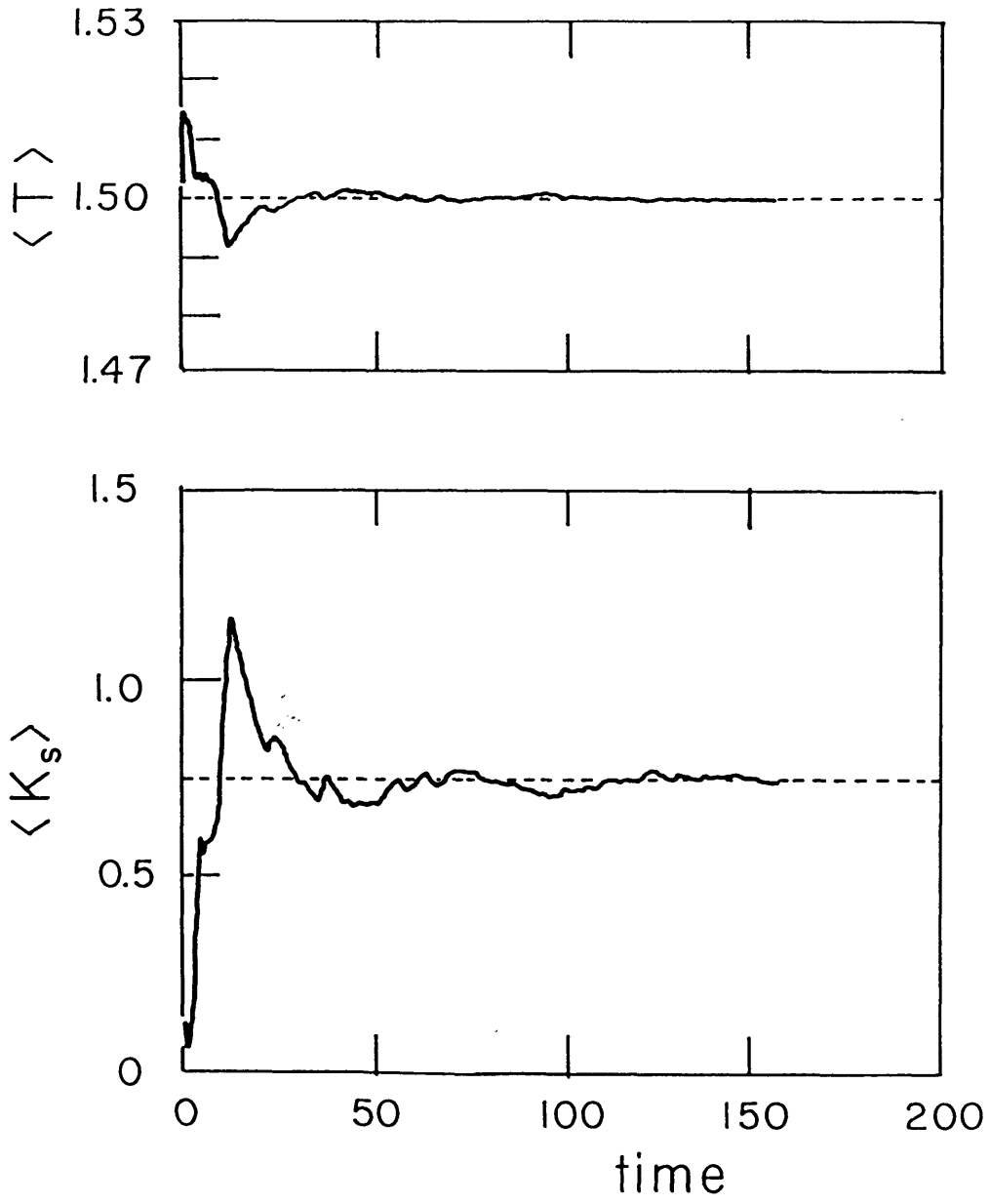

Figure 2-2: Average temperature and average thermostat kinetic energy for an extended 32 particle LJ system in the fluid phase ($T_{ext} = 1.5, \rho = 0.8$) for the thermostat effective mass, $Q = 0.01$. The time step is $\Delta t = 2 \times 10^{-5}$, and the total number of time steps is 8×10^6. T is the instantaneous temperature of the LJ system, and K_s is the thermostat kinetic energy. Horizontal dashed lines are the theoretical values of the canonical ensemble.

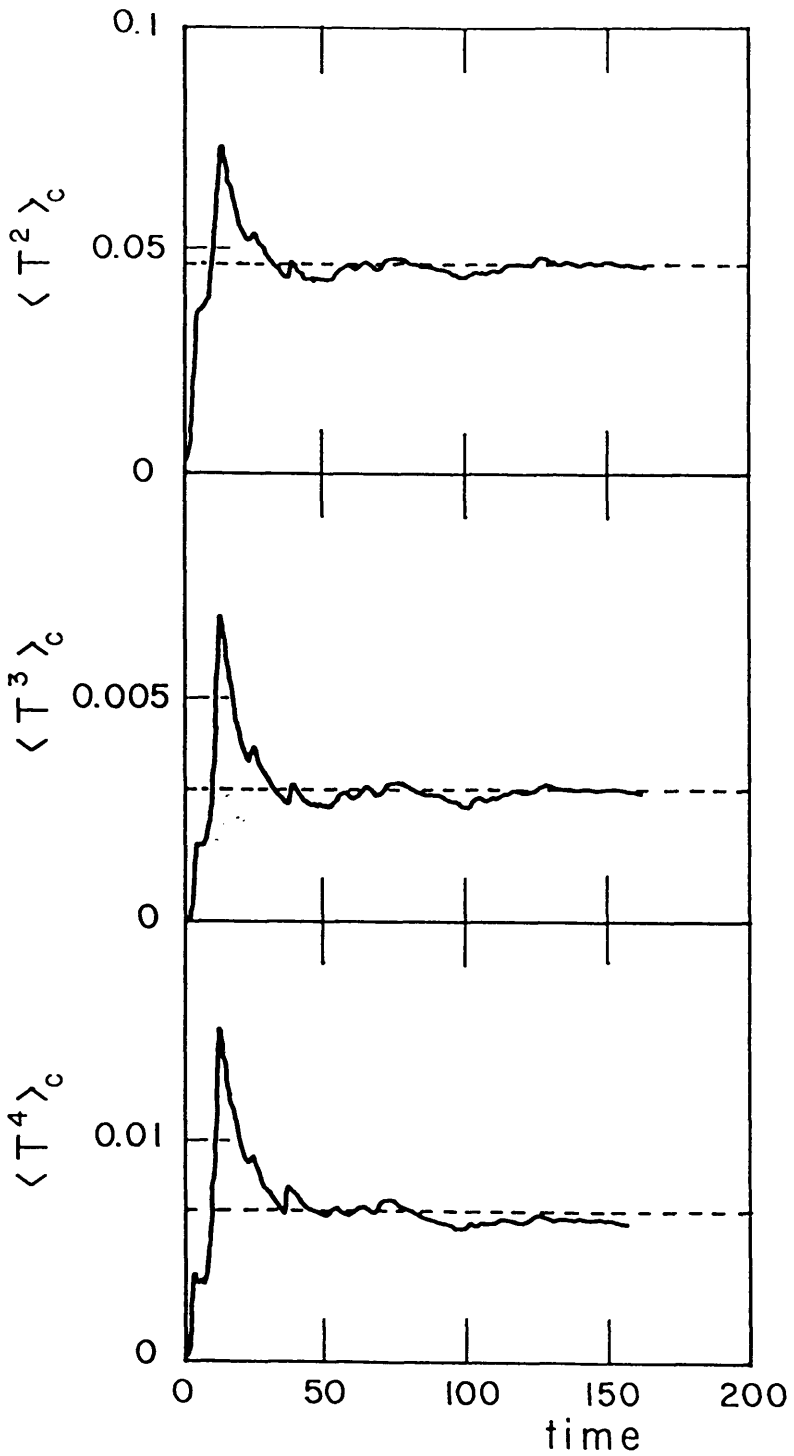

Figure 2-3: The 2nd, 3rd, and 4th moments of the temperature fluctuations of an extended 32 particle LJ system in the fluid phase ($T_{ext} = 1.5, \rho = 0.8$) with $Q = 0.01$ and $\Delta t = 2 \times 10^{-5}$ up to 8×10^6 time steps. T is the instantaneous temperature of the LJ system. Horizontal dashed lines are the theoretical values of the canonical ensemble.

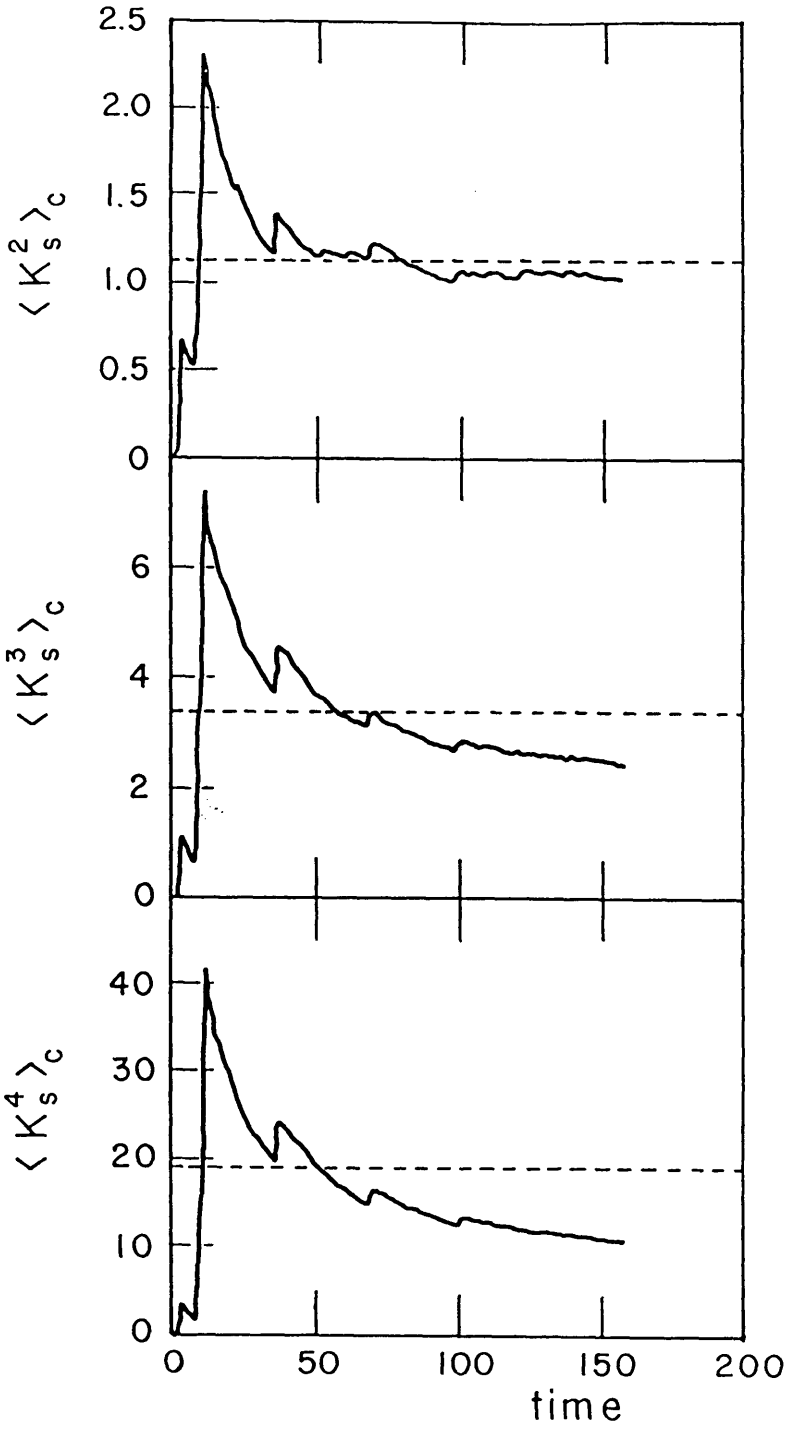

Figure 2-4: The 2nd, 3rd, and 4th moments of the thermostat kinetic energy fluctuations of an extended 32 particle extended LJ system in the fluid phase ($Text = 1.5, \rho = 0.8$) with $Q = 0.01$ and $\Delta t = 2 \times 10^{-5}$ up to 8×10^6 time steps. K_s is the thermostat kinetic energy. Horizontal lines are the theoretical values of the canonical ensemble.

Table 2.2: Five moments of the instantaneous temperature of the LJ system, and five moments of the kinetic energy of s are compared with the predicted values of the canonical ensemble. The results are for simulation in the fluid phase ($T_{ext} = 1.5$, $\rho = 0.8$) of the LJ system. The number of time steps is 8×10^6 and $Q = 0.01$.

	Simulation	Theory	Error	Corresponding T_{ext}^{cal}
$< T >$	1.50022	1.5	0.01%	1.50022
$< T^2 >_c$	0.04619	0.04688	-1.46%	1.48900
$< T^3 >_c$	0.00282	0.00293	-3.75%	1.48100
$< T^4 >_c$	0.00626	0.00687	-8.88%	1.46570
$< T^5 >_c$	0.00117	0.00141	-17.02%	1.4451
$< K_s >$	0.73965	0.75	-1.38%	1.4793
$< K_s^2 >_c$	0.99583	1.125	-11.48%	1.4113
$< K_s^3 >_c$	2.41225	3.375	-28.53%	1.3411
$< K_s^4 >_c$	10.7710	18.984	-43.26%	1.3018
$< K_s^5 >_c$	53.2694	129.094	-59.02%	1.2548

much faster than the molecular collision time, so that a very small time step is required to perform an accurate MD simulation. Thus to generate a reasonable number of molecular collisions one needs a very large number of time steps (e.g. for $Q = 0.01$, 8×10^6 time steps corresponds to about a thousand molecular collisions). On the other hand, for large Q the thermostat variable s changes slowly, and the time step is limited by the molecular collision time. In this case, however, a longer total simulation time is needed in order to include enough fluctuations in s. In short, to obtain the convergence to a canonical ensemble, the following conditions need to be satisfied:

$$\Delta t \ll min(t_{coll}, t_s)$$
$$t_{sim} \gg max(t_{coll}, t_s),$$

where Δt is the time step and t_{sim} is the total simulation time. This explains the results in Table 2.1 consistently, and this also justifies the empirical criterion of making t_s equal to the molecular collision time to obtain fast convergence [34].

2.4 Dynamical Properties of Extended System

In this section we investigate the dynamical behavior of the ES which is commonly termed "Nosé Dynamics" (ND). Velocity autocorrelation functions and power spectral densities are calculated and compared with those of the conventional MD. We find that ND leads to dynamical behavior that is *not* correct in general. Of course, one could side-step this entire problem by performing simulations in the *real* variable formalism (the Nosé-Hoover formalism). We will show, however, that a scaling method can be introduced that significantly reduces the error in ND. In what follows, we present the simulation results first, and then introduce a theory to explain these results.

2.4.1 MD Simulations

In order to study the dynamical properties of the extended LJ system, the velocity autocorrelation function and the power spectral density [1, 4, 37] are calculated and compared within conventional MD and the ESM. The results of the simulations using the virtual variable formalism for a solid phase ($T_{ext} = 1.0, \rho = 1.1$) of a 32 particle Lennard-Jones system are shown in Figure 2-5 and Figure 2- 6. The total number of time steps is $10,000$ and for the ESM simulation $Q = 1$.

The velocity autocorrelation functions as a function of simulation time for MD and ND are presented in Figure 2-5. We note that there exists a significant amount of disagreement between the different simulation techniques. In order to assure that this disagreement does not arise from an insufficient number of time steps, the values of both velocity autocorrelation functions at $t = 0.888$ are tracked as the number of time steps is increased up to 1×10^6. We find that these values change only by a few percent in this exercise so that the disagreement does not improve.

This disagreement in velocity autocorrelation functions carries over to the power spectral densities shown in Figure 2-6. The results in Figure 2-6 are obtained by applying a fast fourier transform (FFT) [4, 37] to the data in Figure 2-5. Since there are a large number of data points, the spectrum is smooth so that additional smoothing techniques like the Maximum Entropy Method are not necessary. The results in

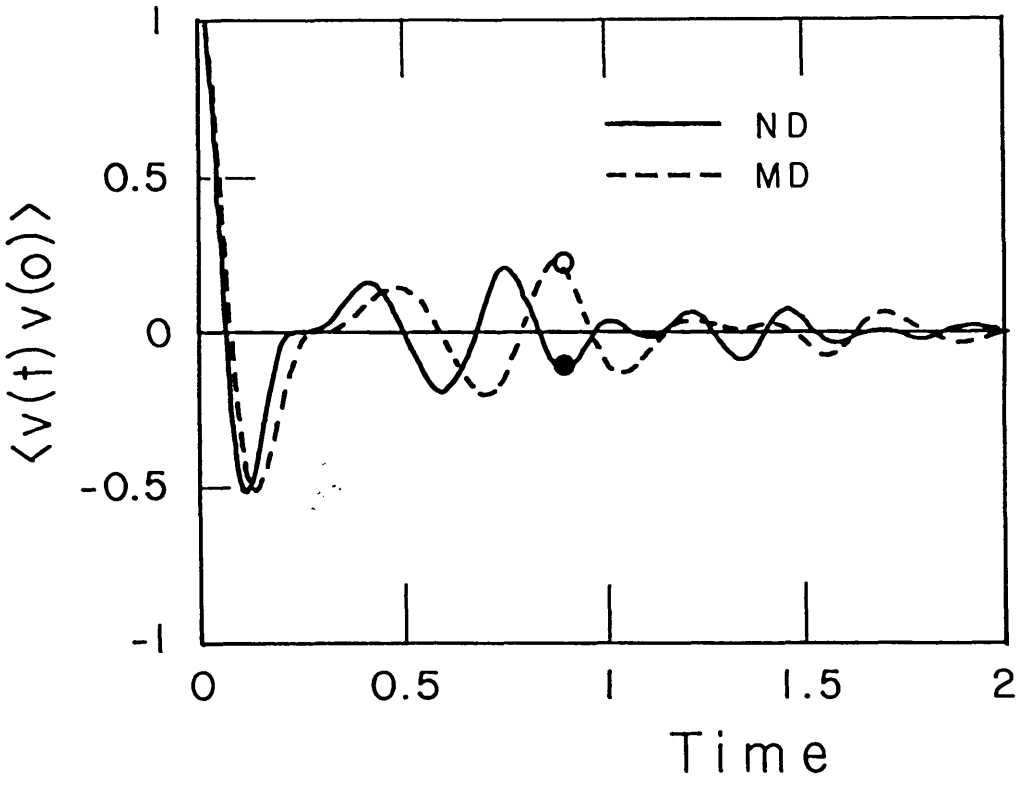

Figure 2-5: Velocity autocorrelation functions using conventional MD (dashed line) and the ESM (solid line) for an extended 32 particle LJ system in the solid phase ($T_{ext} = 1.0.\rho = 1.1$). The total number of time steps is 10^4. For the ESM, $Q = 1$. The filled and open circles at $t = 0.888$ correspond to a run of 10^6 time steps.

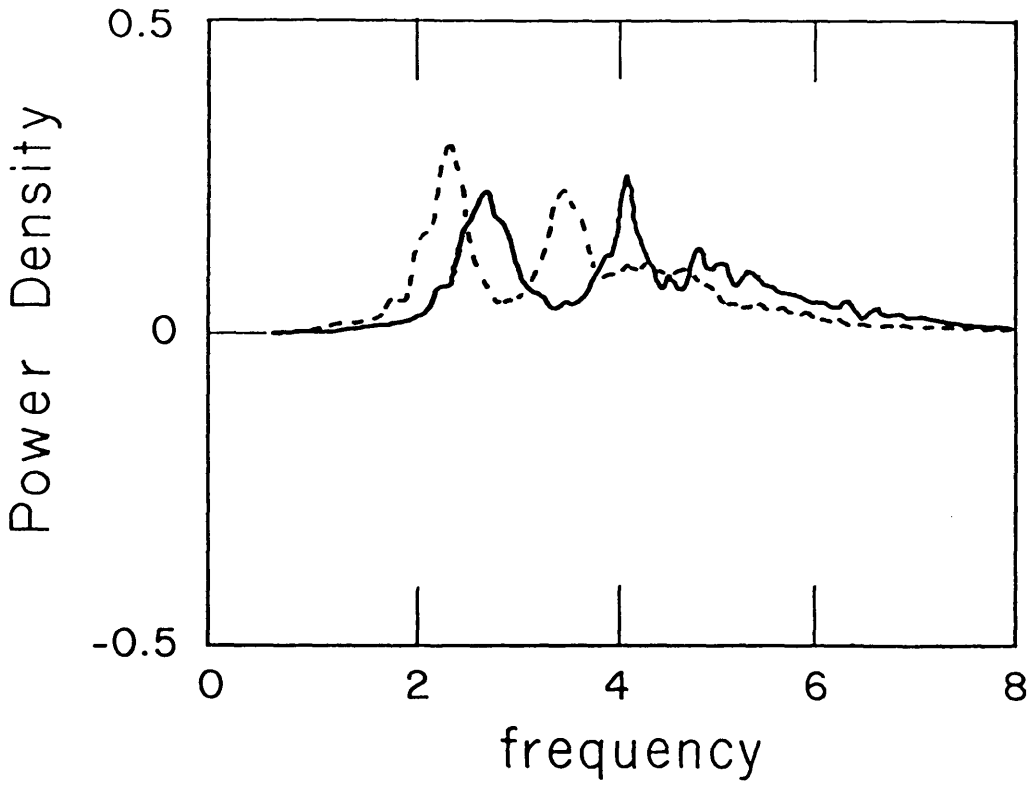

Figure 2-6: Power spectral densities of the conventional MD (dashed line) and the ESM (solid line). The results are obtained from the corresponding velocity autocorrelation functions shown in Figure 2-5 using the classical Blackman-Tukey FFT method.

Figure 2-6 clearly indicate that phonon frequencies are not correctly reproduced in general using ND.

In the top panel of Figure 2-7 we show a plot of the times associated with the first two minima and maxima of velocity autocorrelation function using ND. as a function of the corresponding times with MD, for different values of $< s >$. The results clearly show that the velocity autocorrelation functions can be stretched or shortened according to the value of $< s >$. This suggests that $< s >$ can be used to scale the time in ND. The results of this exercise are shown at the bottom of Figure 2-7. We note that now maxima and minima of the ESM agree very well with those of the conventional MD.

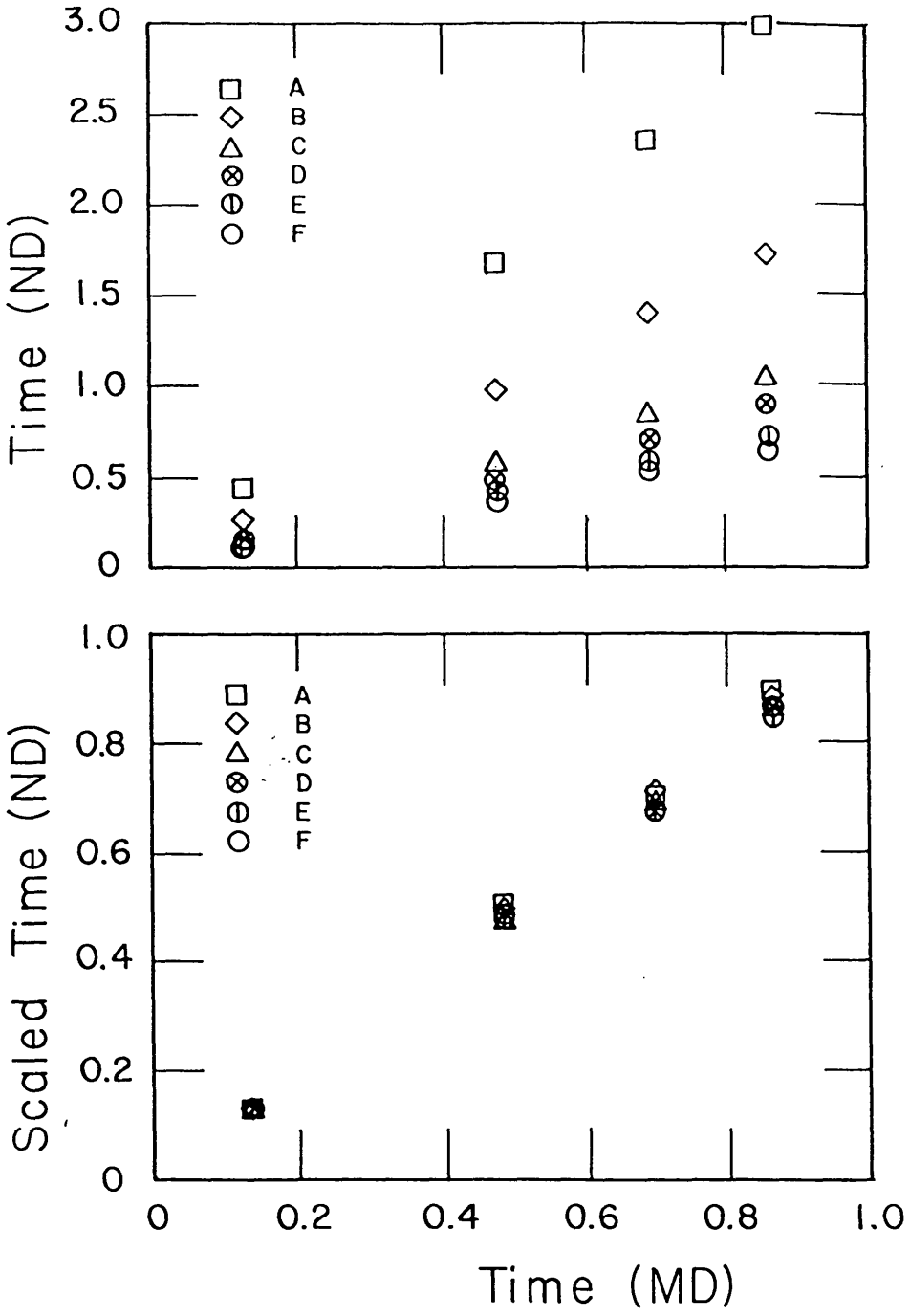

Figure 2-7: The vertical axis shows the times associated with the first two maxima and minima of the velocity autocorrelation functions using ND, before (top) and after (bottom) time rescaling. The horizontal axis shows the corresponding times for these extrema using MD. The labels A, B, C, D, E, and F correspond to $< s >= 3.337, 1.941, 1.21, 1.026, 0.852$ and 0.736 respectively.

2.4.2 Theory

The simulation results in the previous section show that the dynamical properties are not correctly reproduced in general in the virtual variable formalism of the ESM. However, we find that the errors in the dynamical properties can be significantly reduced by rescaling the ND time by $< s >$. In particular

$$t' = \frac{t}{< s >}. \tag{2.24}$$

We now show that this rescaling leads to dynamical properties that are calculated within an error of $(s - < s >)/ < s >$ which is inversely proportional to the square root of the number of degrees of freedom [34].

The equation of motion in the virtual variable formalism is

$$\frac{d}{dt}(s^2 \mathbf{v_i}) = \mathbf{f_i}. \tag{2.25}$$

Replacement of the velocity by the real velocity, $\mathbf{v_i'} = s\mathbf{v_i}$, and integration over t gives the velocity evolution as

$$s(t)\mathbf{v_i'}(t) = s(0)\mathbf{v_i'}(0) + \int_0^t \mathbf{f_i} dt. \tag{2.26}$$

If we now let $s(t) =< s > +\delta s(t)$ and change from t to $t/ < s >$. we obtain

$$(1 + \frac{\delta s(t)}{< s >})\mathbf{v_i'}(t) = (1 + \frac{\delta s(0)}{< s >})\mathbf{v_i'}(0) + \int_0^{\frac{t}{<s>}} \mathbf{f_i} dt'. \tag{2.27}$$

Note that the fluctuation, $\delta s/ < s >$, arises from the s dynamics which does not have direct physical meaning, and its magnitude is small for a large extended system (for the 32 particle system it is about 10%). If one neglects this fluctuation, s is equal to the average value, $< s >$, and the time evolution of the velocity is given as follows:

$$\mathbf{v_i'}(t) = \mathbf{v_i'}(0) + \frac{1}{< s >} \int_0^t \mathbf{f_i} dt, \tag{2.28}$$

or upon rescaling:

$$= \mathbf{v}_i'(0) + \int_0^{\frac{t}{<s>}} \mathbf{f}_i dt'. \tag{2.29}$$

Thus (4.5) can be interpreted as the equation of motion of the conventional MD with the time rescaled as $t/ < s >$ and, therefore, the time evolution of the velocity, $\mathbf{v}_i'(t)$ is equal to $\mathbf{v}_i{}^{MD}(t/ < s >)$.

The velocity autocorrelation function is given by

$$C_{vv}(t) = \frac{\sum_i < \mathbf{v}_i'(t)\mathbf{v}_i'(0) >}{\sum_i < \mathbf{v}_i'(0)\mathbf{v}_i'(0) >}. \tag{2.30}$$

If the fluctuation of s is neglected, $C_{vv}(t)$ of the ESM corresponds to $C_{vv}^{MD}(t/ < s >)$. This then explains the results in Figure 2-7. After time rescaling all the velocity autocorrelation functions agree with that of the conventional MD. The amount of error in the velocity autocorrelation function is on the order of $\delta s/ < s >$ and from Figure 2-7 we see that this error is not significant.

2.5 Conclusion

We have shown that the extended Lennard-Jones potential system is ergodic for Q values from 0.01 to 50 which leads us to the speculation that the extended system is ergodic for any value of Q. The dependence of the rate of convergence to the canonical ensemble on the value of Q can be explained simply from the existence of two time scales in the ES. These are the molecular collision time, t_{coll}, and the time scale of s dynamics, t_s. The time step, Δt, should be much smaller than both time scales, and the total simulation time should be much longer than both time scales. Thus a larger number of time steps is needed for large Q or small Q where the two time scales, t_{coll} and t_s, are very different. This explains the behavior of the ES for small Q and large Q without the need to assume the non-ergodicity of the ES for those cases, and agrees with the results of very long simulations.

The dynamical properties of the LJ system calculated from the ESM are not

rigorously correct. However, for all practical purposes, they can be brought into good agreement with the dynamics of the conventional MD if one perform the proper rescaling. The rescaling procedure has an error on the order of $\delta s / < s >$ which is inversely proportional to the square root of the number of degrees of freedom. Within this amount of error, i.e. to the lowest order in s, the ESM generates meaningful physical dynamics, and the error can be reduced by increasing the number of degrees of freedom. Furthermore, in the virtual variable formalism the rescaling of time is essential in order to obtain results that do *not* depend on the thermostat parameters, Q and $< s >$.

Chapter 3

Constant-Temperature Molecular Dynamics with Momentum Conservation

The Nosé theorem of the extended system method of the constant temperature molecular dynamics is generalized by including the conservation of the total virtual momentum. It is proved that a canonical ensemble of an $N-1$ particle system is generated from an extended system of an N particle system *only if* the total virtual momentum is zero. It is also shown that the resulting $N-1$ particle system has a slightly different mass spectrum than that of the original N particle system. The consequences of this new mass spectrum is relevant in the calculation of dynamical properties and the relaxation times of the system, but irrelevant to thermodynamic averages. For practical considerations, numerical simulations are performed and tested against this new theorem. The differences in application of the Nosé theorem and the generalized-Nosé theorem are discussed.

3.1 Introduction

Molecular dynamics (MD) is a computational method that numerically solves Newton's equations of motion by performing a discrete time integration [1]. According to

the assumption of ergodicity, one can generate an ensemble by collecting the physical states at each discrete time step. The ensemble generated by the MD method depends on the boundary conditions [38]. For *particles in a box* the ensemble generated is the traditional microcanonical ensemble where only the total energy of the system is conserved. For periodic boundary conditions (which are preferred in simulations) the ensemble is no longer strictly microcanonical because in this case the total linear momentum is also conserved[1].

In some cases, the neglect of the conservation of the total momentum will introduce only a small amount of error in the interpretation of MD simulation results [1]. However, there are cases where the conservation of the total momentum should play a crucial role in determining the nature of an ensemble generated by the MD method. We have discovered that the extended system method of Nosé is precisely such a case.

The extended system method (ESM) introduces an extra dynamical variable to simulate the effect of the heat reservoir or the pressure reservoir [30, 31, 32]. The ESM of the constant temperature molecular dynamics is known to generate a canonical ensemble of a physical system if the extended system (ES) is ergodic [32, 33, 34, 5]. This generation of a canonical ensemble from an ergodic ES is guaranteed by the Nosé theorem within the Hamiltonian formalism [32]. However, in this theorem, only the conservation of the total ES energy is used, and the conservation of the total virtual momentum and the total virtual angular momentum are ignored [32].

One can safely ignore the conservation of the total virtual *angular* momentum because it is not conserved during the simulation if a periodic boundary condition is used [38]. However, one cannot ignore the conservation of the total virtual momentum because this *is* conserved during numerical simulations. Therefore, the Nosé theorem is no longer strictly valid for actual ESM simulations. Consequently, any theoretical proof which will determine the conditions under which one can obtain the canonical ensemble of a physical system from the ESM must include the conservation of the total virtual momentum as well as the conservation of the total ES energy.

[1]Even though Newton's equations also satisfy the conservation of the total angular momentum, periodic boundary conditions destroy the conservation of the total angular momentum.

In this paper, we generalize the Nosé theorem by including the conservation of the total virtual momentum and prove analytically that a canonical ensemble is generated from the ES *only if* the total virtual momentum is *zero*. This generalized Nosé theorem shows that the physical system satisfying a canonical ensemble is a $N-1$ particle system with a different mass spectrum from that of the original N particle physical system.

We also perform simulations with zero and nonzero total virtual momentum in order to demonstrate, in a practical way, the consequences of the generalized Nosé theorem. Finally, we discuss the practical considerations related to the difference of these two theorems.

This paper is organized as follows. In Sec. 3.2, we prove the generalized Nosé theorem. In Sec. 3.3, we study the effect of nonzero total virtual momentum using numerical simulations. In Sec. 3.4, we discuss the practical considerations related to the generalized Nosé theorem. In Sec. 3.5, we summarize and conclude.

3.2 Generalized Nosé theorem

In this section, we prove the generalized Nosé theorem by calculating the ES partition function with both the energy conservation and the total virtual momentum conservation which are the valid conditions for practical applications. The following is the generalized Nosé theorem: *if ES is ergodic and if the total linear virtual momentum of N particle physical system is* zero, *then the ESM will generate a canonical ensemble for an $N-1$ particle system with a* different *mass spectrum.*

For the proof, we assume the ergodicity of the ES so that the ES partition function has a microcanonical ensemble form of energy delta function and momentum delta function. The partiton function of an ergodic ES is

$$Z = c \int \prod_{i=1}^{N} d\mathbf{r}_i d\mathbf{p}_i \int ds dP_s \delta(H_{ES} - E) \delta(\sum_{i=1}^{N} \mathbf{p}_i - \mathbf{P_0}), \tag{3.1}$$

where the ES Hamiltonian is expressed in terms of its own canonical variables as

follows[2]:

$$H_{ES}(\mathbf{r}_i, \mathbf{p}_i, s, P_s) = \sum_{i=1}^{N} \frac{\mathbf{p}_i^2}{2m_i s^2} + \phi(\{\mathbf{r}_i\}) + \frac{P_s^2}{2Q} + gk_B T_{ext} ln(s). \tag{3.2}$$

By introducing the center of mass (CM) momenta, $\tilde{\mathbf{p}}_i = \mathbf{p}_i - \mathbf{P_0}/N$, the kinetic energy term becomes a sum of the relative kinetic energy and the CM kinetic energy as follows:

$$\sum_{i=1}^{N} \frac{\mathbf{p}_i^2}{2m_i s^2} = \sum_{i=1}^{N} \frac{\tilde{\mathbf{p}}_i^2}{2m_i s^2} + \frac{\mathbf{P_0}^2}{2Ms^2}, \tag{3.3}$$

where $M = \sum_{i=1}^{N} m_i$. The partition function can be expressed using the CM momenta as follows:

$$Z = c \int \prod_{i=1}^{N} d\mathbf{r}_i d\tilde{\mathbf{p}}_i \int ds dP_s \delta(H_{ES} - E) \delta(\sum_{i=1}^{N} \tilde{\mathbf{p}}_i), \tag{3.4}$$

where H_{ES} is

$$H_{ES} = \sum_{i=1}^{N} \frac{\tilde{\mathbf{p}}_i^2}{2m_i s^2} + \frac{\mathbf{P_0}^2}{2Ms^2} + \phi(\{\mathbf{r}_i\}) + \frac{P_s^2}{2Q} + gk_B T_{ext} ln(s). \tag{3.5}$$

Now, one can eliminate the momentum delta function by performing an integration of $\tilde{\mathbf{p}}_N$ and obtain

$$Z = c \int \prod_{i=1}^{N} d\mathbf{r}_i \prod_{i=1}^{N-1} d\tilde{\mathbf{p}}_i \int ds dP_s \delta(H_{ES} - E), \tag{3.6}$$

where the argument of the energy delta function, $H_{ES} - E$, is

$$\begin{aligned} H_{ES} - E \;=\; & \sum_{i=1}^{N-1} \frac{\tilde{\mathbf{p}}_i^2}{2m_i s^2} + \frac{(\sum_{i=1}^{N-1} \tilde{\mathbf{p}}_i)^2}{2m_N s^2} + \frac{\mathbf{P_0}^2}{2Ms^2} + \phi(\{\mathbf{r}_i\}) \\ & + \frac{P_s^2}{2Q} + gk_B T_{ext} ln(s) - E. \end{aligned} \tag{3.7}$$

[2]The virtual variable formalism (Hamiltonian formalism) and other formalisms are reviewed in [5].

The next step is to diagonalize the inverse mass matrix M^{-1}, where

$$(M^{-1})_{ij} = \frac{1}{m_N} + \frac{1}{m_i}\delta_{ij}. \tag{3.8}$$

This can be done easily by introducing normal mode momenta π_i such that

$$\sum_{i=1}^{N-1} \frac{\tilde{\mathbf{p}}_i^2}{2m_i s^2} + \frac{(\sum_{i=1}^{N-1} \tilde{\mathbf{p}}_i)^2}{2m_N s^2} = \sum_{i=1}^{N-1} \frac{\pi_i^2}{2\lambda_i s^2}. \tag{3.9}$$

If the masses are identical (i.e., $m_i = m$), one then obtains $\lambda_i = m$ for $i = 1, ..., N-2$ and $\lambda_{N-1} = m/N$. After this diagonalization, the partition function becomes

$$\begin{aligned} Z &= c\int \prod_{i=1}^{N} d\mathbf{r}_i \prod_{i=1}^{N-1} d\pi_i \int ds dP_s \\ &\quad \times\delta(\sum_{i=1}^{N-1} \frac{\pi_i^2}{2\lambda_i s^2} + \frac{\mathbf{P_0}^2}{2Ms^2} + \phi(\{\mathbf{r}_i\}) + \frac{P_s^2}{2Q} + gk_BT_{ext}ln(s) - E). \end{aligned} \tag{3.10}$$

Finally, one introduces the physical momenta, $\mathbf{p'}_i = \pi_i/s$, to eliminate the s variable in the kinetic energy term and obtains the partition function as follows:

$$\begin{aligned} Z &= c\int \prod_{i=1}^{N} d\mathbf{r}_i \prod_{i=1}^{N-1} d\mathbf{p'}_i \int ds dP_s s^{3N-3} \\ &\quad \times\delta(\sum_{i=1}^{N-1} \frac{\mathbf{p'}_i^2}{2\lambda_i} + \frac{\mathbf{P_0}^2}{2Ms^2} + \phi(\{\mathbf{r}_i\}) + \frac{P_s^2}{2Q} + gk_BT_{ext}ln(s) - E). \end{aligned} \tag{3.11}$$

This integral has a similar form to the one in the original formulation of Nosé except for the presence of the CM kinetic energy term in the energy delta function and $3N-3$ momentum integration instead of $3N$. In the following, we perform the s integration, and discuss the consequences of the differences between the integral (2.11) and the original intergal of Nosé [32].

In general, if $\mathbf{P_0} \neq 0$, the argument of the energy delta function has two roots of s, s_1 and s_2, as illustrated in Figure 3-1, and the delta function becomes as follows:

$$\sum_{i=1}^{2} \frac{\delta(s - s_i)}{|-K_0/s^3 + gk_BT_{ext}/s|_{s=s_i}}, \tag{3.12}$$

where $K_0 = \mathbf{P_0}^2/2M$. The integration over s gives the following expression:

$$\begin{aligned} Z &= c\int \prod_{i=1}^{N} d\mathbf{r}_i \prod_{i=1}^{N-1} d\mathbf{p}'_i \int ds dP_s s^{3N-3} \sum_{i=1}^{2} \frac{\delta(s-s_i)}{|-K_0/s^3 + gk_BT_{ext}/s|_{s=s_i}}, \\ &= c\int \prod_{i=1}^{N} d\mathbf{r}_i \prod_{i=1}^{N-1} d\mathbf{p}'_i \int dP_s \sum_{i=1}^{2} \frac{s_i^{3N-3}}{|-K_0/s^3 + gk_BT_{ext}/s|_{s=s_i}}. \end{aligned} \tag{3.13}$$

Obviously, the integrand is not the Boltzman factor of a physical Hamiltonian.

In the case of $\mathbf{P_0} = 0$, the problem simplifies considerably, and one can perform the integration over s in (2.1) immediately. For completeness, however, we use (2.13) and set $K_0 = 0$. Since $\mathbf{P_0} = 0$, there is only one root of s, s_0, as shown in Figure 3-1, and one obtains

$$\begin{aligned} Z &= c\int \prod_{i=1}^{N} d\mathbf{r}_i \prod_{i=1}^{N-1} d\mathbf{p}'_i \int dP_s s_0^{3N-3} \frac{s_0}{gk_BT_{ext}} \\ &= c'\int \prod_{i=1}^{N} d\mathbf{r}_i \prod_{i=1}^{N-1} d\mathbf{p}'_i e^{-\beta_{ext}H_0} \int dP_s e^{-\beta_{ext}\frac{P_s^2}{2Q}}, \end{aligned} \tag{3.14}$$

where $g = 3N - 2$ is used, and H_0 is the physical Hamiltonian,

$$H_0 = \sum_{i=1}^{N-1} \frac{\mathbf{p}'^2_i}{2\lambda_i} + \phi(\{\mathbf{r}_i\}). \tag{3.15}$$

Therefore, one obtains a canonical ensemble of the $N-1$ particle system with the mass spectrum $\{\lambda_i\}$ from the N particle system with the mass spectrum $\{m_i\}$ only if total virtual momentum is zero. This completes the proof of the generalized Nosé theorem.

3.3 Numerical Simulations

In this section, we perform numerical simulations of the extended Lennard-Jones (LJ) system with both zero and nonzero total virtual momentum, and test the simulations against the generalized Nosé theorem. In Sec. 3.3.1, we derive the analytic expression for the average moments of the instantaneous temperature and the thermostat kinetic energy from the canonical ensemble. In Sec. 3.3.2, we compare these quantities with

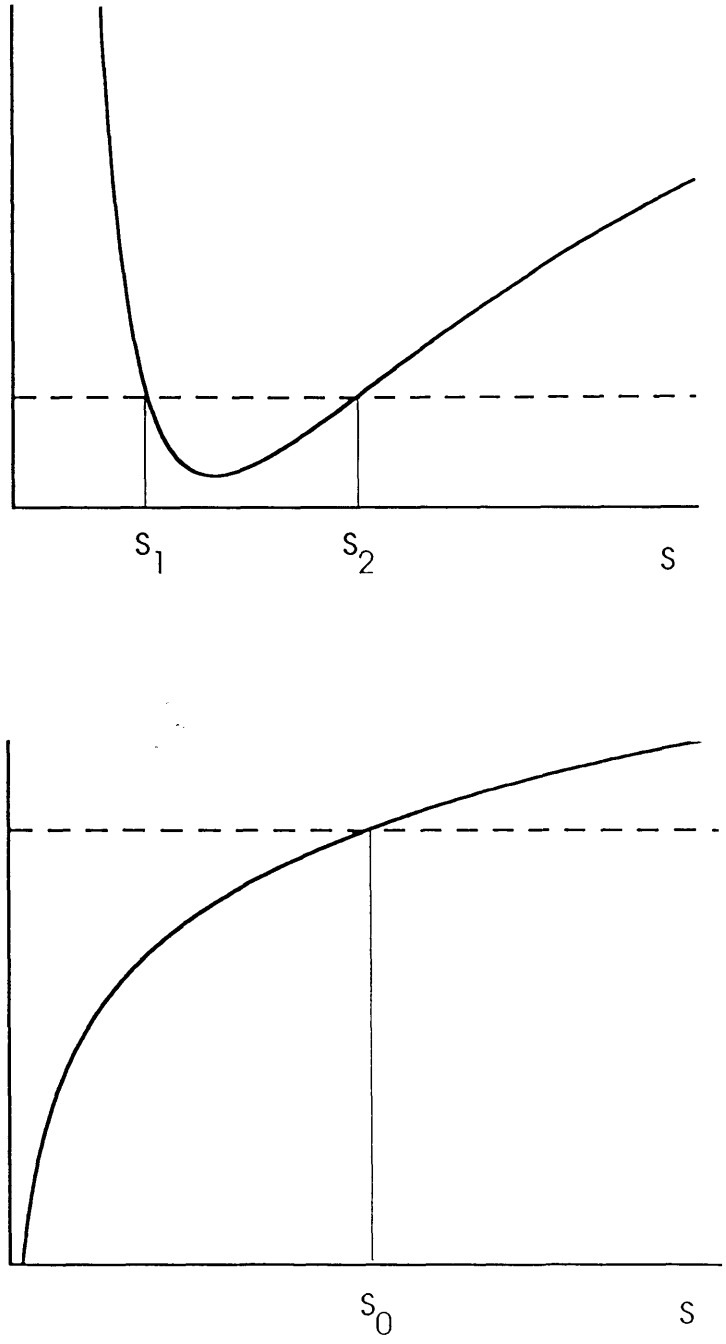

Figure 3-1: Top panel illustrates two solutions of the equation $K_0/s^2 + gk_BT_{ext}ln(s) = E_0$ with $K_0 \neq 0$. Bottom panel illustrates the solution of the equation with $K_0 = 0$.

the results of numerical simulations.

3.3.1 Analytic Expression of Moments

In this section, we describe the canonical ensemble expression of the moments of the instantaneous temperature of the LJ system and the thermostat kinetic energy. The instantaneous temperature T is defined as follows:

$$T = \frac{2}{(3N-3)k_B}K, \tag{3.16}$$

where K is the kinetic energy of $N-1$ particles. The analytic expressions of the moments of the instantaneous temperature fluctuation are obtained from a canonical ensemble as follows:

$$< T > = T_{ext} \tag{3.17}$$

$$< T^2 >_c = \frac{2}{f}T_{ext}^2 \tag{3.18}$$

$$< T^3 >_c = \frac{8}{f^2}T_{ext}^3 \tag{3.19}$$

$$< T^4 >_c = (\frac{2}{f})^3(\frac{3f}{2}+6)T_{ext}^4, \tag{3.20}$$

where $f = 3N-3$, $<>$ represents an ensemble average,
and $< T^m >_c = < (T - < T >)^m >$.

The moments of thermostat kinetic energy are the following:

$$< K_s > = \frac{1}{2}k_B T_{ext} \tag{3.21}$$

$$< K_s^2 >_c = \frac{1}{2}(k_B T_{ext})^2 \tag{3.22}$$

$$< K_s^3 >_c = (k_B T_{ext})^3 \tag{3.23}$$

$$< K_s^4 >_c = \frac{15}{4}(k_B T_{ext})^4, \tag{3.24}$$

where K_s is the thermostat kinetic energy.

Table 3.1: The reduced units of Ne is compared with the conventional units. m_e is the electron mass and a_0 is the Bohr radius.

Quantity	LJ Unit	Conventional Unit
Q	1	$1.05 \times 10^6 m_e a_0^2$
t	1	$2.24 \times 10^{-12} sec$
ρ	1	0.050 Å^{-3}
T	1	$36.23K$

3.3.2 Molecular Dynamics Simulations

In this section, we define the simulation parameters and conditions, and describe the results of the simulations. We then discuss the results by comparing with the generalized Nosé theorem.

In the numerical simulations the reduced units of a LJ system are used. For example, the LJ units of Ne are compared with the conventional units in Table 3.1. The equations of motion are solved using the sixth order Gear predictor-corrector method [1]. To eliminate boundary effects a periodic boundary condition is adapted, and to avoid self-interactions due to the long range interaction, the LJ potential is cut at r_c ($r_c = 2.5$). To compensate the cutoff effect, a long range correction is made by adding the average of the interaction beyond r_c. The precision of the calculation is monitored by preserving the total energy of the extended system within 0.2% drift during the whole simulations (-0.04% drift for nonzero total momentum, and -0.16% drift for zero total momentum).

To obtain a fast convergence of the moments, a small (32-particle) LJ system is chosen for the simulations. The intial configuration of the simulations is a fcc lattice structure, and the initial velocities are randomly assigned with a given mean value determined by T_{ext}. For the case of zero total momentum, the initial velocities are corrected to give a zero sum. On the other hand, for the case of nonzero total momentum, a certain amount of CM velocity is added to the initial velocities. The initial values of thermostat and thermostat velocity are chosen to be 1 for all simulations.

In the simulations, the thermostat effective mass Q is chosen to be 1 which gives a fast convergence for the liquid phase ($T_{ext} = 1.5$, $\rho = 0.8$) of the simulations.

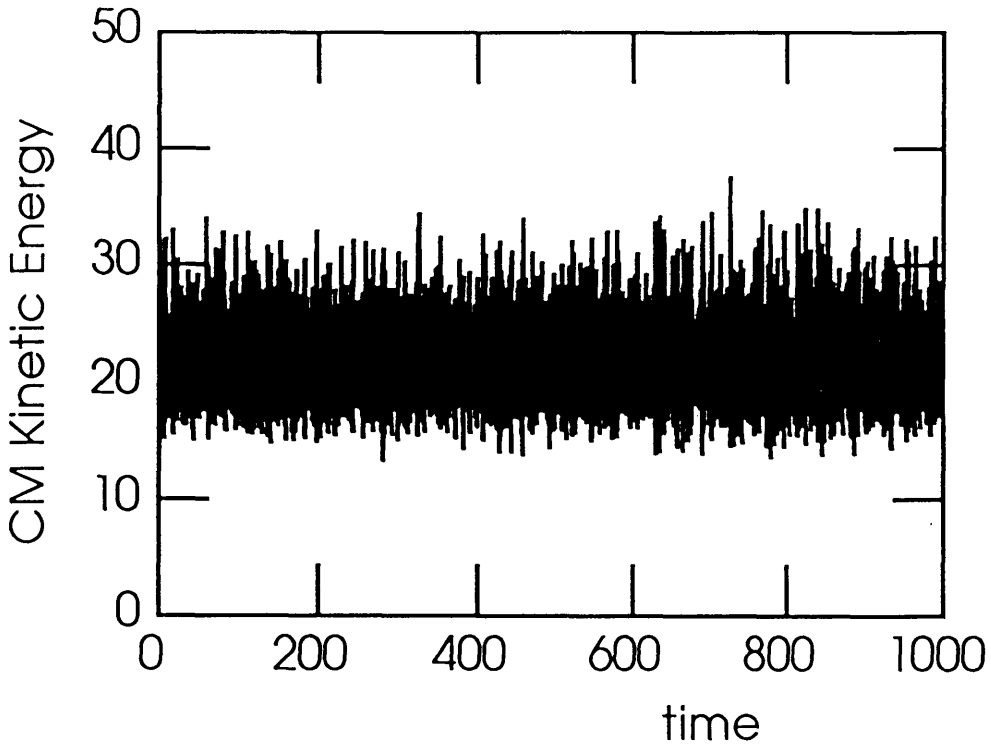

Figure 3-2: CM kinetic energy K_0/s^2 as a funtion of time for the extended LJ fluid ($T_{ext} = 1.5$, $\rho = 0.8$) with nonzero total momentum and thermostat effective mass, $Q = 1$. The time step is $\Delta t = 0.001$, and the total number of time steps is 10^6. Reduced LJ units are used for the energy and the time.

Simulations are done with 10^6 time steps for a liquid phase ($T_{ext} = 1.5$, $\rho = 0.8$) for both zero and nonzero total momentum. The total virtual momentum is found to be constant with $5 - 6$ significant figures.

The results of the simulation for nonzero total momentum are shown in Figures 3-2, 3-3, and 3-4. Figure 3-2 shows the CM kinetic energy K_0/s^2 as a function of time. Figure 3-3 the shows average temperature and the average thermostat kinetic energy, and Figure 3-4 shows the second moments of temperature and thermostat kinetic energy. The final values of the average moments are summarized in Table 3.2. For this simulation, the CM kinetic energy is very large ($\sim 25T_{ext}$), and clearly both the averages and the second moments do *not* converge to the canonical ensemble values shown as dotted lines.

The results of simulations for zero total momentum are shown in Figures 3-5, 3-6,

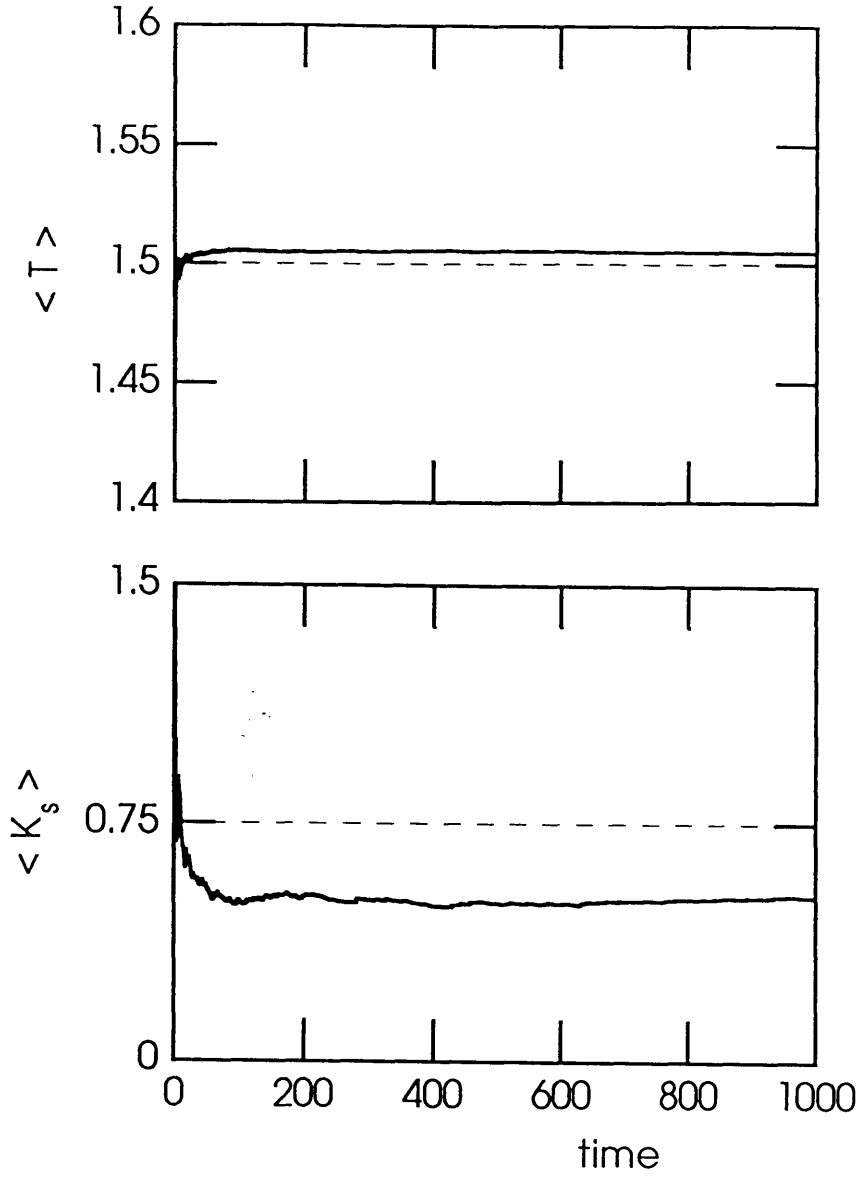

Figure 3-3: Average temperature and average thermostat kinetic energy for the extended LJ fluid ($T_{ext} = 1.5$, $\rho = 0.8$) with nonzero total momentum. The thermostat effective mass is $Q = 1$, the time step is $\Delta t = 0.001$, and the total number of time steps is 10^6. T is the instantaneous temperature of the LJ system, and K_s is the thermostat kinetic energy. Horizontal dashed lines are the theoretical values of the canonical ensemble. Reduced LJ units are used for the temperature and the time.

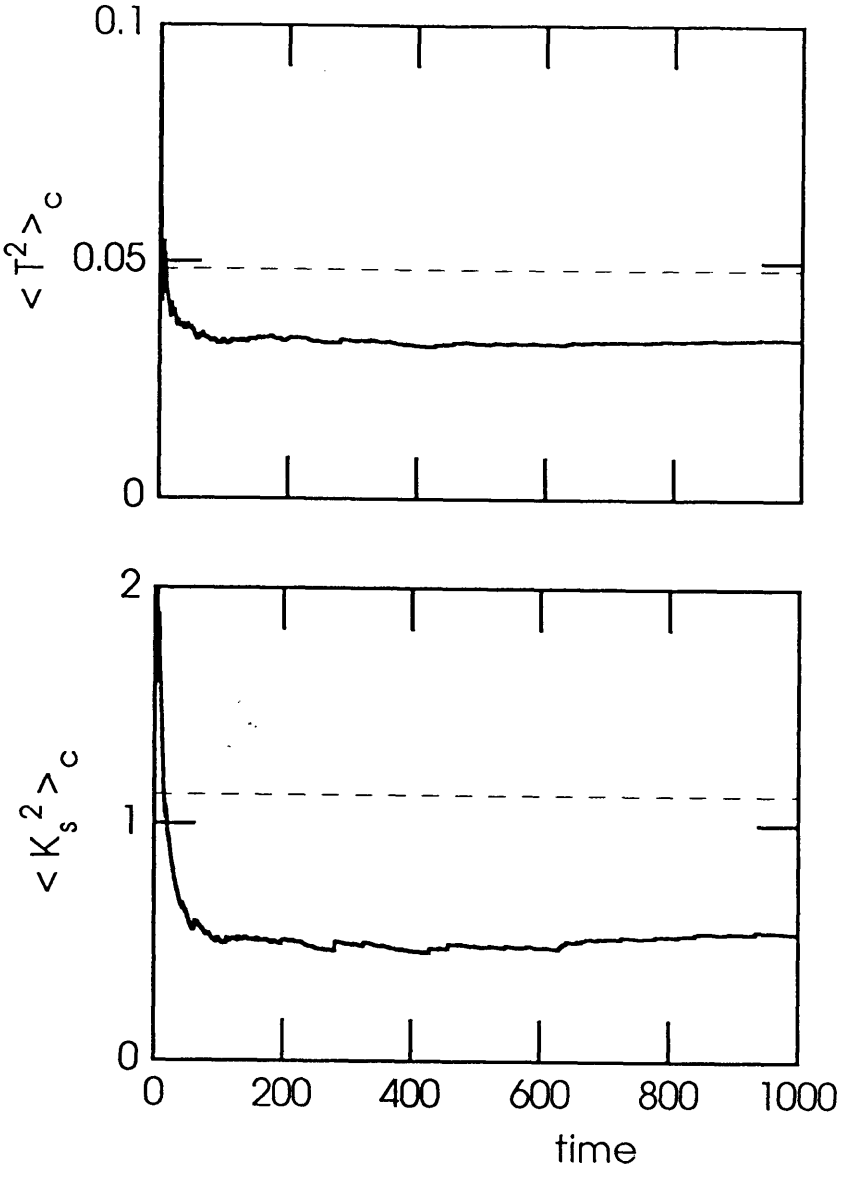

Figure 3-4: The 2nd moment of temperature fluctuation and the 2nd moment thermostat kinetic energy fluctuation for the extended LJ fluid ($T_{ext} = 1.5$, $\rho = 0.8$) with nonzero total momentum. The thermostat effective mass is $Q = 1$, the time step is $\Delta t = 0.001$, and the total number of time steps is 10^6. Horizontal dashed lines are the theoretical values of the canonical ensemble. Reduced LJ units are used for the temperature and the time.

Table 3.2: Four moments of the instantaneous temperature of the LJ system, and four moments of the kinetic energy of s are compared with the predicted values of the canonical ensemble. The results are for simulation in the fluid phase ($T_{ext} = 1.5$, $\rho = 0.8$) of the LJ system with $|\mathbf{P_0}| \neq 0$. The number of time steps is 10^6 and $Q = 1$.

	Simulation	Canonical Ensemble Value
$< T >$	1.50494	1.5
$< T^2 >_c$	0.03364	0.04839
$< T^3 >_c$	0.00141	0.00312
$< T^4 >_c$	0.00344	0.00722
$< K_s >$	0.51999	0.75
$< K_s^2 >_c$	0.54088	1.125
$< K_s^3 >_c$	1.12309	3.375
$< K_s^4 >_c$	4.35128	18.984

Table 3.3: Four moments of the instantaneous temperature of the LJ system, and four moments of the kinetic energy of s are compared with the predicted values of the canonical ensemble. The results are for simulation in the fluid phase ($T_{ext} = 1.5$, $\rho = 0.8$) of the LJ system with $\mathbf{P_0} = 0$. The number of time steps is 10^6 and $Q = 1$.

	Simulation	Theory	Error	Corresponding T_{ext}^{cal}
$< T >$	1.50009	1.5	0.01%	1.50009
$< T^2 >_c$	0.04858	0.04839	0.39%	1.50299
$< T^3 >_c$	0.00304	0.00312	-2.56%	1.48680
$< T^4 >_c$	0.00723	0.00722	0.14%	1.49506
$< K_s >$	0.74467	0.75	-0.71%	1.48934
$< K_s^2 >_c$	1.06167	1.125	-5.63%	1.45717
$< K_s^3 >_c$	2.96659	3.375	-12.1%	1.43688
$< K_s^4 >_c$	15.8016	18.984	-16.8%	1.43274

and 3-7. Each component of the total momentum is smaller than 10^{-5} during the whole simulation. Figure 3-5 shows that the average temperature and the average thermostat kinetic energy are quite well converged to the canonical ensemble values. Figure 3-6 shows that the higher moments of temperature are also very well converged to the canonical ensemble values. The higher moments of K_s in Figure 3-7 show a slower but a reasonable convergence to the canonical ensemble values. The final values of the average moments are summarized in Table 3.3.

Therefore, the simulation with $\mathbf{P_0} \neq 0$ does not produce a canonical ensemble whereas the simulation with $\mathbf{P_0} = 0$ produces a canonical ensemble. Consequently,

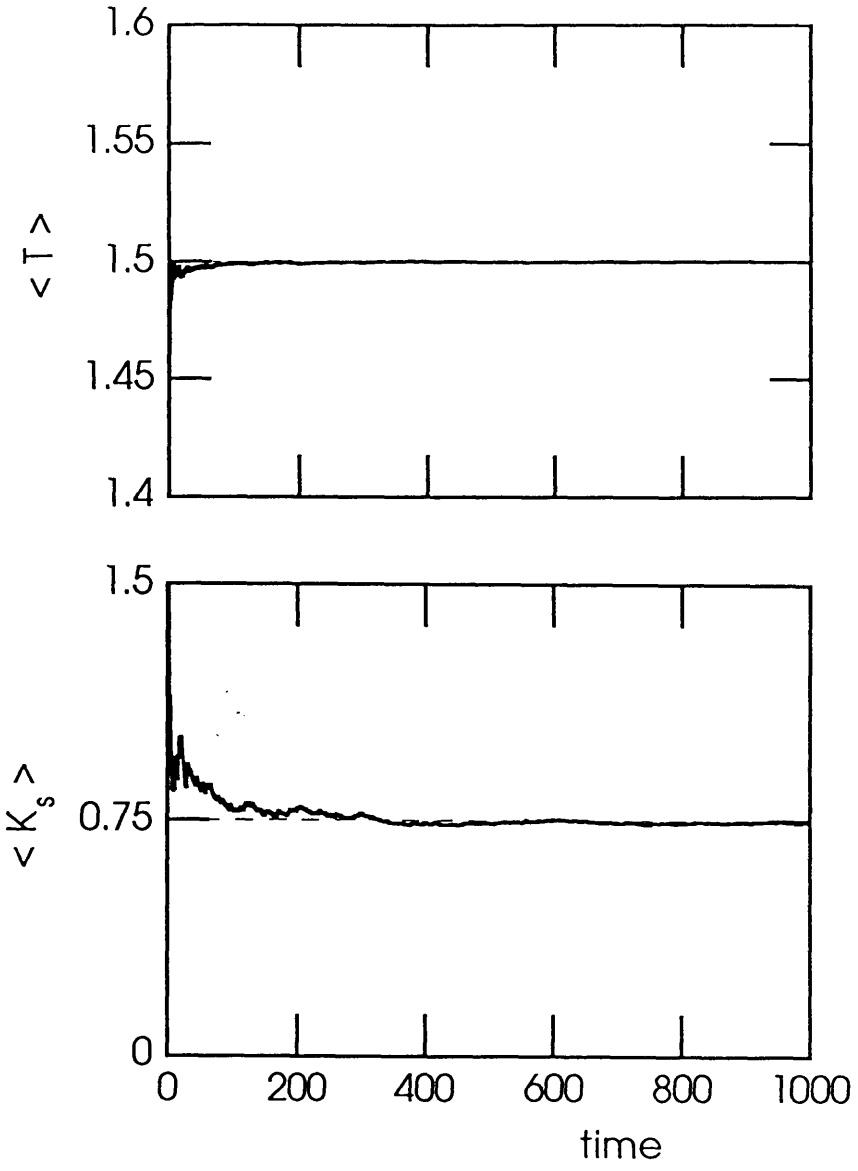

Figure 3-5: Average temperature and average thermostat kinetic energy for the extended LJ fluid ($T_{ext} = 1.5$, $\rho = 0.8$) with zero total momentum. The thermostat effective mass is $Q = 1$, the time step is $\Delta t = 0.001$, and the total number of time steps is 10^6. Horizontal dashed lines are the theoretical values of the canonical ensemble. Reduced LJ units are used for the temperature and the time.

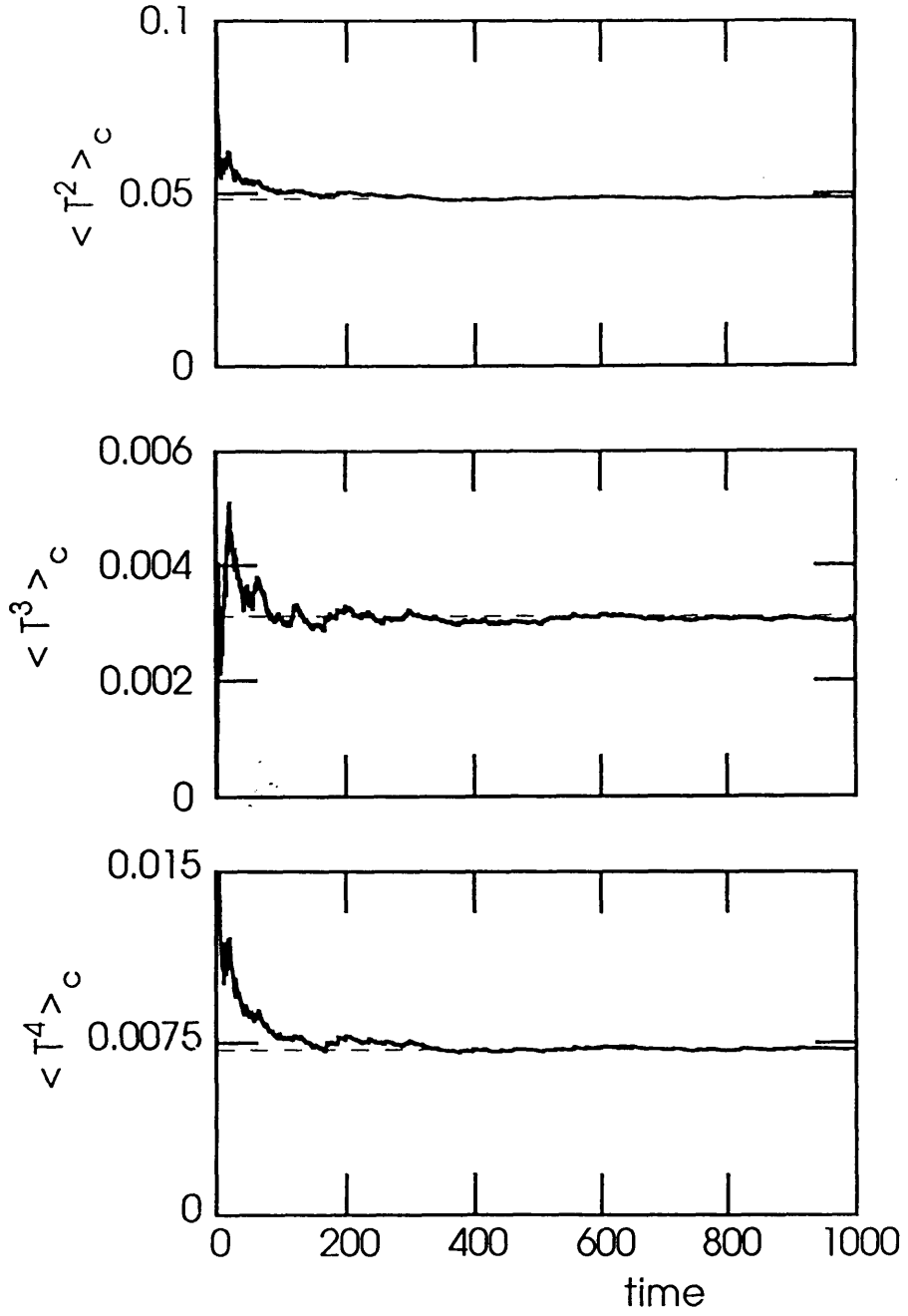

Figure 3-6: The 2nd, 3rd, and 4th moments of the temperature fluctuations for the extended LJ fluid ($T_{ext} = 1.5$, $\rho = 0.8$) with zero total momentum. The thermostat effective mass is $Q = 1$, the time step is $\Delta t = 0.001$, and the total number of time steps is 10^6. T is the instantaneous temperature of the LJ system, and K_s is the thermostat kinetic energy. Horizontal dashed lines are the theoretical values of the canonical ensemble. Reduced LJ units are used for the temperature and the time.

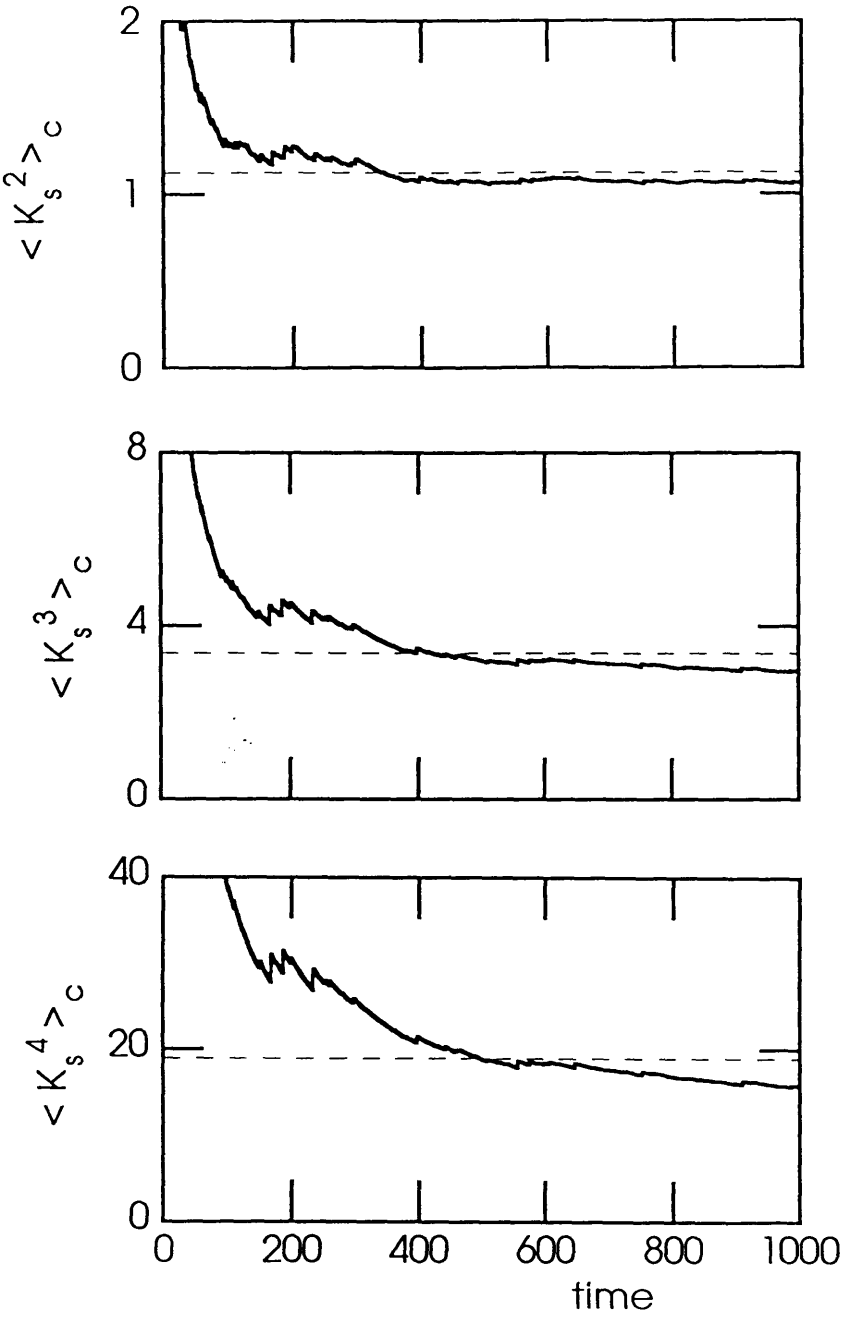

Figure 3-7: The 2nd, 3rd, and 4th moments of the thermostat kinetic energy fluctuations for the extended LJ fluid ($T_{ext} = 1.5$, $\rho = 0.8$) with zero total momentum. The thermostat effective mass is $Q = 1$, the time step is $\Delta t = 0.001$, and the total number of time steps is 10^6. Horizontal dashed lines are the theoretical values of the canonical ensemble. Reduced LJ units are used for the temperature and the time.

both simulations of the LJ potential system with zero and nonzero total momentum satisfy the generalized Nosé theorem.

Simulations are also performmed with different values of CM kinetic energy. For a small CM kinetic energy ($< K_0/s^2 > \leq T_{ext}$) the results are found to be quite similar to those of zero total momentum. This fact suggests that quite a good approximate canonical ensemble can be generated with nonzero total momentum even if the total momentum is on the order of the external temperature. However, as the CM kinetic energy increases ($< K_0/s^2 > \gg T_{ext}$), the deviation from the canonical ensemble values becomes large. These facts guarantee the *numerical stability* of generating a canonical ensemble by ESM in practical applications where computational errors inevitably introduce a small nonzero total momentum. This numerical stability is further discussed in Sec. 3.4.

3.4 Practical Considerations

In this section, we discuss the differences between the Nosé theorem and the generalized Nosé theorem from a practical viewpoint. We discuss three separate topics. The first is the new mass spectrum λ_i of the resulting Hamiltonian satisfying a canonical ensemble. The second is the effect of nonzero total momentum on changing the average moments of temperature and thermostat kinetic energy from canonical ensemble values. The third is the effect of changing the number of degrees of freedom from $3N$ to $3N-3$ on the interpretation of numerical simulations.

First, in the proof of the generalized Nosé theorem one begins with a physical Hamiltonian with mass spectrum $\{m_i\}$, $i = 1, ..., N$ and obtains the final Hamiltonian with mass spectrum $\{\lambda_i\}$, $i = 1, ..., N-1$. In general, the new masses are different from the original masses. For the special case of N identical original masses ($m_i = m$) one finds a final mass spectrum: $\lambda_i = m$ for $i = 1, ..., N-2$ and $\lambda_{N-1} = m/N$. This new mass spectrum will contribute in principle to the difference of the dynamical properties between the conventional MD and the Nosé Dynamics which is discussed in [5]. Of course, as N becomes large, the contribution of the light mass becomes

unimportant in practical considerations. As far as thermodynamic averages are concerned, the difference of mass spectrums is always irrelevant because of the equipartition theorem. The only significant change relevant to the thermodynamic averages is the reduction of the number of degrees of freedom from $3N$ to $3N-3$.

Second, if $\mathbf{P_0} \neq 0$, then the physical system does not satisfy a canonical ensemble as we have shown in Sec. 3.2. However, if $|\mathbf{P_0}|$ is small, one can make the following approximations. For small $|\mathbf{P_0}|$, s_1 is very small so that $s_1^{3N-3} \ll s_2^{3N-3}$. Hence one can neglect the first integral containing s_1 in the partition function (3.12). The remaining integral containing s_2 can be approximated as follows:

$$|-K_0/s_2^3 + gk_BT_{ext}/s_2| \approx |gk_BT_{ext}/s_2|, \tag{3.25}$$

since $K_0/s_2^2 \ll gk_BT_{ext}$ for small $|\mathbf{P_0}|$. After these two approximations, the partition function reduces to the partition function of zero total momentun. The correction is $O(K_0/gk_BT_{ext})$, and this explains why one can still get good average moments for a small nonzero total momentum as discussed in Sec. 3.3.

Third, if one ignores the momentum conservation entirely as is typically done (i.e., one uses the Nosé theorem to interpret a numerical simulation), then one sets $g = 3N+1$ instead of $g = 3N-2$, and defines the instantaneous temperature as $T = 2K/(3Nk_B)$ rather than Eq. (3.1). Since the Nosé theorem is not strictly valid, one introduces a systematic error in the interpretation of numerical simulations as shown in the following.

In a simulation, one compares the average moments of temperature with those of T_{ext} (3.2-5), but the value of T_{ext} is defined only as a portion of the coefficient of the thermostat potential

$$gT_{ext} \cdot k_B ln(s). \tag{3.26}$$

Therefore, when one uses $g = 3N+1$ and T_{ext}, it is equivalent to using the correct

$g' = 3N - 2$ with the actual externally set temperature being

$$T'_{ext} = \frac{g}{g'} T_{ext} = \frac{3N+1}{3N-2} T_{ext}. \tag{3.27}$$

For a 32 particle system, T'_{ext} is 3.2% larger than T_{ext}. This difference could introduce a significant error in many practical applications. For example, one can obtain a wrong melting temperature by using this interpretation. This error becomes large for a small system so that one should be careful when applying the ESM to small clusters.

Finally, we note that this error in actual external temperature, although definitely present in a simulation where $g = 3N+1$, will not be detected if one simply compares $< T = 2K/(3Nk_B) >$ with T_{ext}. To see this recall that the actual instantaneous temperature T' is given by Eq. (3.1) so that

$$T' = \frac{3N}{3N-3} T. \tag{3.28}$$

According to the generalized Nosé theorem, one must have

$$< T' >= T'_{ext}. \tag{3.29}$$

Using (4.3), (4.4), and (4.5) one then obtains

$$\begin{aligned} < T > &= \frac{(3N-3)(3N+1)}{3N(3N-2)} T_{ext}, \\ &= (1 - \frac{3}{3N(3N-2)}) T_{ext}. \end{aligned} \tag{3.30}$$

This relation means that the errors in T_{ext} and T cancel systematically. For the 32 particle LJ system, the difference between $< T >$ and T_{ext} is only 0.03%. We emphasize however that both T_{ext} and $< T >$ are off by about 3% from the correct value T'_{ext}.

Therefore, the use of the Nosé theorem instead of the generalized Nosé theorem in the interpretation of numerical simulations will lead to a systematic error which

cannot be detected by a simple "self consistency" check of comparing $< T >$ and T_{ext}. Of course, since the actual error in T_{ext} scales as $O(1/N)$, this error will be important only for systems with small number of particles.

3.5 Conclusions

The Nosé theorem is correct only when the total energy of the system is conserved. In practical applications, the total virtual momentum is also conserved, and therefore the Nosé theorem is no longer strictly valid. Inclusion of the conservation of the total virtual momentum in the original argument of Nosé leads to a generalized Nosé theorem that is valid in practical applications.

The generalized Nosé theorem is proved analytically. As a consequence of the generalized Nosé theorem, if the ES is ergodic and if the total virtual momentum of N particle system is zero, then the ESM yields a canonical ensemble for an $N-1$ particle system with a different mass spectrum. The consequences of a different mass spectrum are irrelevent to thermodynamic averages, but relevent to the dynamical properties and relaxation times of the system.

The effect of nonzero total momentum is of order K_0/gk_BT_{ext} for small $|\mathbf{P_0}|$. This fact provides a numerical stability of generating a canonical ensemble in practical situations where small nonzero $|\mathbf{P_0}|$ is introduced by computation errors.

Numerical simulations are performed and tested against the generalized Nosé theorem. The simulations are found to satisfy the generalized Nosé theorem and the numerical stability is obtained as expected from the theory.

Chapter 4

Wavelets in Electronic Structure Calculations

A three dimensional (3D) wavelet analysis is employed to develop a new formalism for electronic structure calculations. The wavelet formalism provides a systematically improvable and tractable description of electronic wavefunctions and overcomes limitations of conventional basis expansions. The potential power of the wavelet formalism for *ab initio* electronic structure calculations is demonstrated by a calculation of $1s$ states for all the naturally occurring nuclei on the periodic table and the interaction energies of the hydrogen molecule ion.

4.1 Introduction

Spectral analysis using the Fourier transform (FT) is a powerful method for solving many problems in science and engineering. This method, however, is not appropriate for problems that require a localized description in real space *and* in Fourier space. Although several techniques, such as the windowed Fourier transform, have been invented to attempt to overcome this limitation, by far the most promising new technique is the wavelet transform (WT) [39]. Unlike the plane wave (PW) basis functions of the FT, the wavelet basis functions are localized both in real space *and* in Fourier space [39, 40, 41, 42]. Furthermore, multiresolution analysis (MRA) of the WT

provides a systematic successive approximation scheme for practical applications [39, 40]. Applications of the WT have focused primarily on digital signal processing (1D), compact image coding (2D), and related fast mathematical algorithms [41]. Most recently the WT has been applied to the analysis of chaotic behavior and turbulence in 2D, the coherent states of quantum optics and quantum field theory, and to real space renormalization group theory [42].

In this letter, we introduce a new method for the application of WT, in 3D, to electronic structure investigations of material properties. The traditional *ab initio* total energy density functional pseudopotential methods for electronic structure calculations use either LCAO-type (*e.g.* atomic, Gaussian, or Slater) basis sets or PW basis sets [2]. LCAO-type basis sets typically are capable of describing the electronic structure with a small number of basis functions, but lack an explicit and well-defined procedure for systematic improvement[1], and generally complicate the calculation of forces because of the presence of large Pulay terms [43] which must be compensated through explicit calculation. On the other hand, PW basis sets provide a systematic expansion of electronic wavefunctions, introduce no Pulay terms for supercells of fixed size (thus considerably simplifying the calculation of forces), but suffer from the same limitations as the FT method. Specifically, the description of the rapid variations of the electronic wavefunction close to the atomic nuclei (atomic core) requires a large number of PW functions even though the volume of the atomic core is only a small part of the total volume of the system. In addition PW basis sets are, in principle, not well suited for the description of isolated molecules and surfaces. This is because the periodic nature of the basis introduces unnecessary periodic images and a redundant high resolution description of the vacuum regions.

The "best of all worlds" then would be to have a basis set that, unlike a PW basis, can zoom into the atomic core regions and does not introduce unnecessary periodic images, *and*, unlike an LCAO-type basis, does not introduce Pulay terms which must be calculated explicitly, and provides an explicit prescription for complete

[1]Improvement of LCAO-type basis sets is an art requiring experience and knowledge of the system under study. In contrast PW basis sets offer guaranteed systematic convergence merely by increasing the kinetic energy of the basis set.

expansion of the electronic wavefunctions. The wavelet basis has all these desired properties: multiscale decomposition of the wavefunction, the localized description of the rapid variations, and systematically complete expansion similar to the PW expansion. Therefore, as we demonstrate in this letter, the wavelet basis overcomes the limitations of both conventional basis sets and retains only their advantages.

We begin our discussion with a brief review of the basic concepts underlying wavelets. We then extend the wavelet formalism to the solution of the Schrödinger equation with the introduction of spherically symmetric basis functions. As a simple example we apply our technique to the study of a hydrogen atom. We then demonstrate that a *single* small basis set is capable of calculating accurately the $1s$ states of all the nuclei from Hydrogen through Uranium! Finally we demonstrate that a wavelet basis can easily describe covalent bonding and illustrate its use with the hydrogen molecule ion (H_2^+). We conclude with a discussion of the straightforward extension of the current analysis to periodic systems and all electron calculations.

4.2 Wavelet Transform and Multiresolution Analysis

Given a square integrable function space $L^2(R^3)$, wavelets impose a hierarchical structure of subspaces with different resolutions which forms a multiresolution analysis. The space of functions at resolution 2^{-j} (or more simply at resolution j) is represented by $V_j(R^3)$, and spanned by the basis set of *scaling functions* at resolution j, $\{\phi_{j,\mathbf{n}}(\mathbf{r})\}$, where $\mathbf{n}$ specifies the center of the basis function. The hierarchical structure is then

$$\cdots V_{-2} \subset V_{-1} \subset V_0 \subset V_1 \subset V_2 \cdots. \tag{4.1}$$

The *approximation* space V_j is decomposed into a sum of the coarser approximation space V_{j-1} and the *wavelet* space W_{j-1} which describes the detail at resolution j ($V_j = V_{j-1} \oplus W_{j-1}$) and is spanned by the basis set of the *wavelet functions* at resolution j, $\{\psi_{j,\mathbf{n}}(\mathbf{r})\}$. With a repetition of this decomposition, the $L^2(R^3)$ space

can be expressed as either the sum of the wavelet spaces of all resolutions or the sum of one approximation space and the wavelet spaces of higher resolutions:

$$\bigoplus_j W_j = V_{j_0} \oplus \bigoplus_{j \geq j_0} W_j = L^2(R^3). \tag{4.2}$$

Therefore, any square integrable function $f(\mathbf{r})$ can be expanded either as a sum of the wavelet functions of all resolutions or as a sum of the scaling functions at resolution $j = j_0$ and the wavelet functions of all finer resolutions $j \geq j_0$. In this work, we will use the latter expansion because it introduces approximations only at the high resolution cutoff in practical applications.

With the introduction of two projection operators, $\hat{A}_j$ (approximation operator) and $\hat{D}_j$ (detail operator), which project a function into V_j and W_j respectively, one may express $f(\mathbf{r})$ as

$$f(\mathbf{r}) = \hat{A}_{j_0} f(\mathbf{r}) + \sum_{j \geq j_0} \hat{D}_j f(\mathbf{r}). \tag{4.3}$$

The approximation and the detail of a function $f(\mathbf{r})$ at resolution j are expanded in terms of the basis functions,

$$\hat{A}_j f(\mathbf{r}) = \sum_{\mathbf{n}} a_{j,\mathbf{n}} \phi_{j,\mathbf{n}}(\mathbf{r}), \tag{4.4}$$

$$\hat{D}_j f(\mathbf{r}) = \sum_{\mathbf{n}} d_{j,\mathbf{n}} \psi_{j,\mathbf{n}}(\mathbf{r}). \tag{4.5}$$

Combination of Eqns. (3)-(5) and truncation at the finest resolution j_{max} leads to the wavelet expansion of $f(\mathbf{r})$ as

$$f(\mathbf{r}) = \sum_{\mathbf{n}} a_{j_0,\mathbf{n}} \phi_{j_0,\mathbf{n}}(\mathbf{r}) + \sum_{j=j_0}^{j_{max}} \sum_{\mathbf{n}} d_{j,\mathbf{n}} \psi_{j,\mathbf{n}}(\mathbf{r}). \tag{4.6}$$

This expansion still contains an infinite number of basis functions associated with the lattice $\{\mathbf{n}\}$. Since the scaling functions and the wavelet functions are spatially localized, one may retain only the basis functions that have significantly large coefficients in Eqn (6) for the problem at hand. This leads to an expansion with a finite

number of basis functions and allows one to use different resolutions for different spatially localized regions. In particular, for the description of the rapid oscillations of the electronic wavefunction in an atomic core region, one need add higher resolution scales *only* to the core region and thereby systematically improve the calculation.

4.3 Construction of a Wavelet Basis Set

Although the wavelet and scaling functions are far from unique, we found that the following forms are particularly convenient in practical applications. The wavelet functions $\psi_{j,\mathbf{n}}(\mathbf{r})$ are chosen to be the Mexican-hat functions (the Laplacians of Gaussians) which form a fairly tight frame [39]. The scaling function $\phi_{0,\mathbf{n}}(\mathbf{r})$corresponding to the Mexican-hat function is chosen to be a Gaussian function. Both the Mexican-hat functions and the Gaussian functions are spherically symmetric. The relationship between the Gaussian scaling function and the Mexican-hat wavelet function is not exact, but is quite a good approximation as discussed in Ref. 1. These localized basis functions are spatially arranged so that their centers form a simple cubic lattice[2]. This is shown schematically in the top panel of Figure 4-1. The lattice spacing d_0 at resolution $j = 0$ is chosen small enough to give a fairly tight frame[3] [39]. The basis functions with resolution j are arranged correspondingly on the lattice sites with lattice spacing $d_0/2^j$. The centers of basis functions for different resolutions are selected so as not to overlap, and the centers of *all* the basis functions form a simple cubic lattice with spacing $d_0/2^{j_{max}}$. In order to construct a *finite* basis set we collect the most important basis functions by introducing spheres of finite support radii at each nuclear center. This is illustrated schematically at the bottom panel of Figure 4-1. Correspondingly smaller support radii are chosen for correspondingly higher resolutions so that deep core regions have more resolution scales. We designate this finite basis set as $\{\phi_{0,\mathbf{n}}(\mathbf{r}), \psi_{j,\mathbf{n}}(\mathbf{r}); j_{max} \geq j \geq 0\}$ or more compactly as $\{b_i(\mathbf{r})\}$ where i is a simplified notation for $\{j, \mathbf{n}\}$.

[2]We have also tested fcc and bcc lattices and obtain similar results to the sc lattice.

[3]For the examples treated in this work d_0 is chosen to be $1au$, and the Gaussian width is $1.35au$.

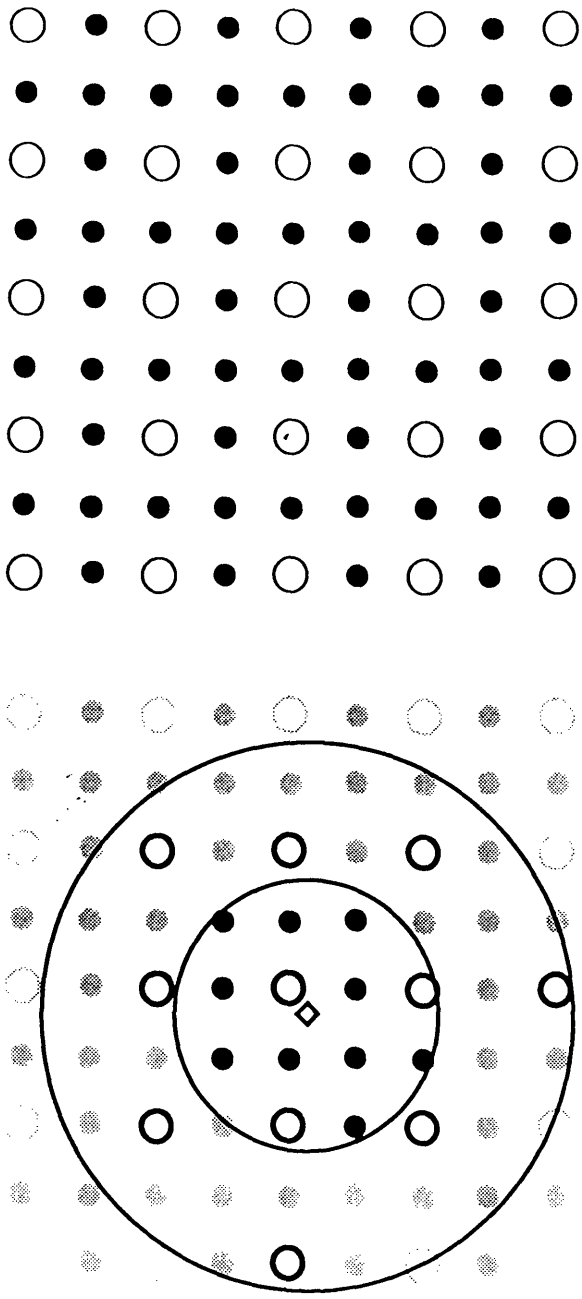

Figure 4-1: Top panel shows a two dimensional arrangement of the centers of basis functions on a simple square lattice. Open circles are the centers of the basis functions at resolution $j = 0$, and filled circles are the centers of the basis functions at resolution $j = 1$. Bottom panel shows the basis functions that lie within each support radius that is centered on an atomic position (diamond-symbol). The larger (smaller) radius corresponds to $j = 0$ ($j = 1$) resolution.

4.4 Solution of Schrödinger Equation

The Schrödinger equation, $\hat{H}|\Psi>=\epsilon|\Psi>$, for electronic structure calculations becomes a generalized eigenvalue problem in a general nonorthogonal wavelet basis. Expansion of the wavefunction in terms of the basis functions ($|\Psi>=\sum_i c_i|b_i>$) leads to the secular equation,

$$\sum_i <b_j|\hat{H}|b_i> c_i = \epsilon \sum_i <b_j|b_i> c_i. \tag{4.7}$$

With our choice of wavelet and scaling functions, all the matrix elements in Eq. (7) can be calculated analytically. Solution of Eq. (7) may then proceed by a number techniques including square root matrix diagonalization[4], Cholesky decomposition [44], molecular dynamics [2], and conjugate gradients [2] approaches. In this work we have used both square root matrix diagonalization and conjugate gradients approaches.

4.5 Hydrogen Atom

In order to gain a sense of the optimal values of the various parameters of the formalism, we chose to study the hydrogen atom as a simple test case. After performing calculations using many different resolution scales and different support radii, we find that a satisfactory minimal basis set for the Hydrogen atom contains 25 basis functions with four resolution scales: (7 scaling functions for $j=0$, plus 6 wavelets for $j=0$, plus 6 wavelets for $j=1$, plus 6 wavelets for $j=2$) which we designate simply as (7 + three 6's). These correspond respectively to support radii of $1au$, $0.5au$, $0.25au$, and $0.125au$. The calculated 1s eigenenergy is within 2% of the exact value, and the calculated 1s radial wavefunction is shown in Figure 4-2. The calculated wavefunction differs from the exact one primarily near the origin (within the resolution limit j_{max}). The small difference at $r=2au$ is due to the finite support radii

[4]This technique reduces a generalized eigenvalue problem to a standard eigenvalue problem by use of the square root of the diagonalized overlap matrix.

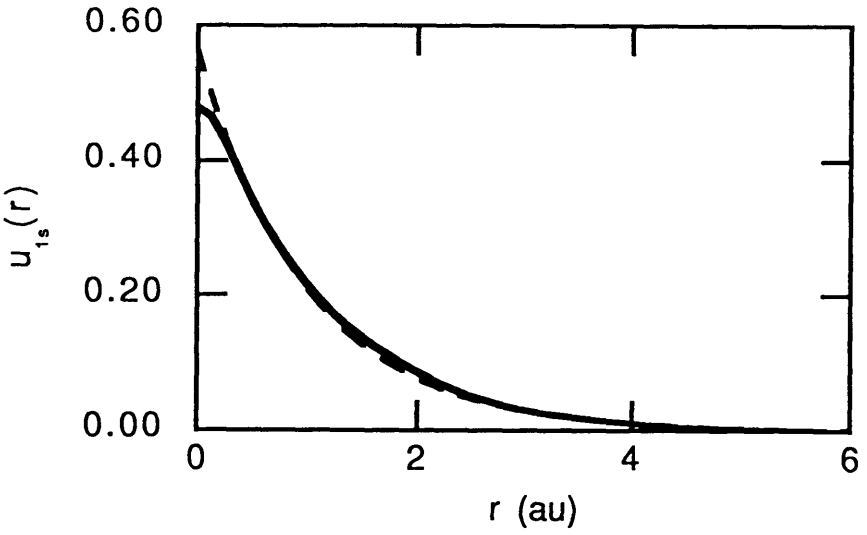

Figure 4-2: The 1s radial wavefunction of a hydrogen atom calculated with 25 basis functions (7 + three 6's). The continuous line in from the wavelet calculation, and the broken line is the exact wavefunction.

used for the basis set. By changing the basis set to 85 functions with three resolution scales (33 + two 26's, with corresponding support radii of $2au$, $1au$ and $0.5au$), this difference reduces to 0.3%, and we can obtain the $1s$ eigenenergy to within 0.5% of the exact value.

4.6 Hydrogen to Uranium

By adding more resolution scales, one can calculate the wavefunctions of heavier nuclei *within the same accuracy* as follows. As the atomic number increases, the Coulomb potential becomes stronger, and consequently higher resolution scales are needed in the core region. However, only *one* additional resolution scale needs to be added each time the atomic number doubles. Therefore, for the description of $1s$ wavefunctions from Hydrogen to Uranium, one needs to use a basis set with eleven resolution scales (7+ ten 6's). Using this fixed basis set consisting of *only* 67 basis functions, one can calculate (to within 3%) the $1s$ eigenvalues of all the naturally occurring nuclei on the periodic table! The results are shown in Figure 4-3 and include, for simplicity, only the even nuclei. Note that the eigenvalue for each nucleus is larger than the

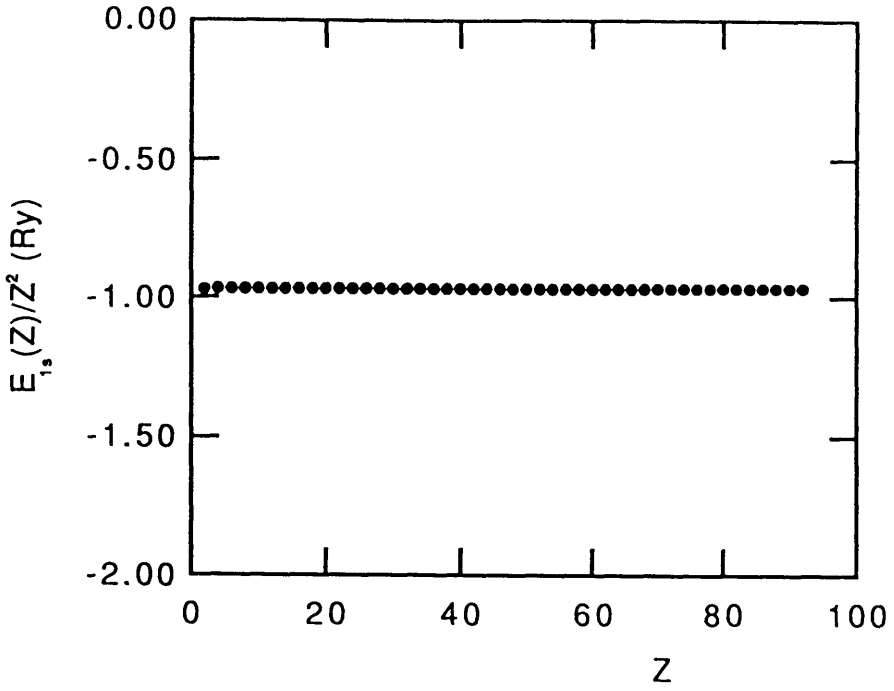

Figure 4-3: The filled circles are the 1s eigenenergies of all the nuclei with even atomic numbers on the periodic table ($Z = 2, 4, ..., 92$) calculated with the fixed 67 basis function set.

exact value by very nearly a constant percentage so that the results appear to lie on a straight line as expected.

4.7 Hydrogen Molecule Ion

We now investigate the efficiency of the wavelet basis for the description of chemical bonds. As a simple example, we consider the energy of an H_2^+ molecule as a function of the separation R between the two protons. The total energy (electronic eigenenergy plus the Coulomb potential energy) is plotted as a function of R in Figure 4-4. The basis set for the calculation is selected using the same support radii as for the hydrogen atom calculation with the larger basis set (33 + two 26's), and the total number of basis functions varies between 141 and 167[5] depending on R. We note that the

[5]Note that this procedure leads naturally to a linear scaling of the basis set size with the number of atoms in the calculations.

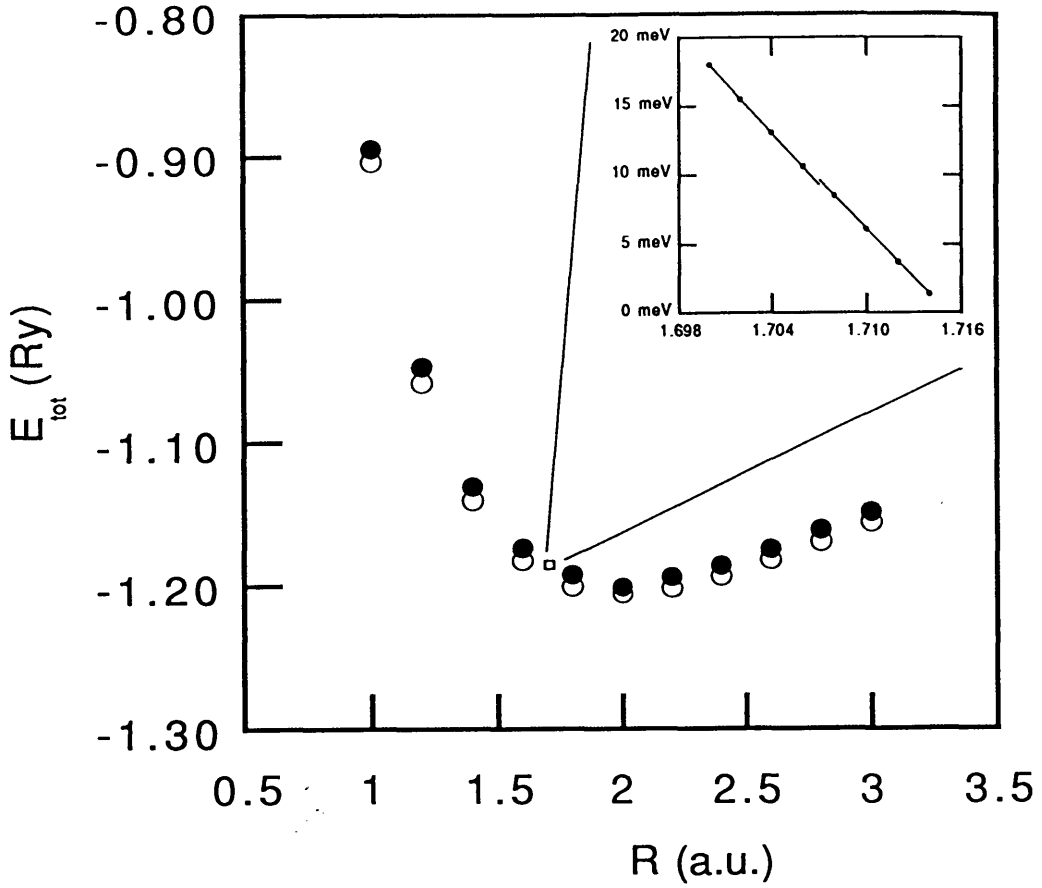

Figure 4-4: The total energy of a molecular hydrogen ion is shown as a function of the separation between the nuclei. The filled circles are the calculations with 141 to 167 basis functions depending on the separation R while the open circles are the exact values. The inset shows fine detail of the calculation in the vicinity of a change in basis, illustrating that basis-change effects are at less than the meV level.

calculated values in Figure 4-4 are very close to the exact values [45] and are larger than them by a nearly constant amount of 1%. This implies that the wavelet basis gives an efficient representation of the chemical bond and also gives an excellent representation of inter-ionic forces.

4.8 Comment on Pulay forces

It is important to note that the centers of the basis functions do not follow the nuclei as they move; the *underlying* basis set is not correlated to the ionic positions.

Just as in the plane wave case, this ensures that the finite underlying wavelet basis introduces *no* Pulay terms for a fixed calculational cell. Although, in practice, it *is* possible to use the full underlying basis, it is much more convenient to introduce the support spheres as we have done above. This does introduce a position dependence into the basis by selecting the basis set as illustrated in the bottom panel of Figure 4-1. However, simply increasing the size of the support radii to where the wavefunction coefficients for the wavelets near the edges of their respective spheres are near zero controls the magnitude of resulting Pulay corrections and eliminates the need for their explicit calculation. Designing the basis to give a good representation of the wavefunctions and their eigenenergies imposes this condition on the coefficients automatically, making the treatment of Pulay forces very simple in the wavelet formalism, as our molecular ion calculation illustrates. Although the cutoff radii for this calculation were chosen only with the representation of the atomic wavefunctions in mind, the effect on the calculation from sudden changes in the basis set is extremely small, as the inset in Figure 4-4 shows. The inset displays a representative example of the detailed behavior of the wavelet calculation on either side of a change in basis set. The discontinuity in the energy is extremely small ($0.3meV$) as is the jump in force/slope ($\approx 1meV/\text{Å}$).

4.9 Conclusions

We have developed a 3D wavelet formalism that is applicable in general to electronic structure investigations of materials, and have demonstrated its potential power by performing calculations of the deepest core states of all the nuclei on the periodic table and the interaction energy of an H_2^+ molecule. The wavelet expansion with a small number of basis functions gives an accurate description of the wavefunction both in an atomic core region and in a chemical bond.

To extend this approach to many-electron systems within LDA, one can simply use traditional techniques for the inclusion of Hartree and exchange-correlation interactions, expanding the charge density and other relevant fields in the wavelet basis

as well. In particular, schemes developed for localized basis sets [46] provide one possible framework for this extension. It is not clear at the moment that the inherent advantages of the wavelet basis will make it more attractive for practical calculations *strictly* within LCAO-type computational frameworks because, at present, the wavelet expansion of atomic states still requires more functions per atom than do corresponding LCAO-type representations. The same is true of plane wave expansions, which nonetheless are competitive with traditional local basis schemes because of the efficiency of the fast Fourier transform. There exists an analogous fast wavelet transform, and work currently is underway to investigate its exploitation and the competitiveness of the resulting computational framework with both LCAO-type basis and plane wave approaches.

In comparison to the plane wave approach, we expect wavelets to prove most advantageous in situations which require a spatial resolution which varies significantly throughout space, including systems involving first row elements or transition metals. Also, the local nature of the wavelet basis ensures that the wavelet transform maps far more naturally than does the fast Fourier transform onto the latest generation of massively parallel computer architectures. On the other hand, it is unlikely that multiple resolutions will benefit systems such as pseudopotential silicon *directly* in terms of numbers of basis functions.

Finally, multigrid approaches provide another possible avenue toward spatially variable resolution. We have not explored this direction in depth, and we do not know what will be the advantages and disadvantages of this approach over the wavelets. It is noteworthy, however, that the basic difference between the two is that wavelets are a set of basis functions whereas multigrid is a method for solving a discretized set of equations.

In conclusion, the trivial process of introducing a Bloch transformation of the wavelet functions extends straightforwardly the current analysis to periodic systems[6]. With the extensions to many-electron systems and periodic systems, the wavelet formalism way open a completely new direction of development for *ab initio* total

[6]The theory of *periodized* wavelets is discussed in [41].

energy calculations.

Chapter 5

Tip-Surface Interactions in Scanning Tunneling Microscopy

The tip-surface interactions in the Scanning Tunneling Microscopy (STM) of the Si(100) surface are investigated with *ab initio* total energy pesudopotential calculations. The results of the calculations lead to a new understanding of the microscopic STM measurement process. It is found that under typical conditions the influence of the tip is large enough to effectively flip a dimer on this surface. This leads to a reinterpretation of the "symmetric" dimer STM image as an asymmetric dimer configuration that flips as it follows the motion of the scanning tip.

5.1 Introduction

Scanning Tunneling Microscopy (STM) provides an image of the structure of a surface at an atomic resolution [47]. This STM image is generated by an electron tunneling between the STM tip and a surface atom under the tip as a result of the overlap between the tip and surface wave functions. Consequently the tip and the surface may in certain cases interact significantly during the process of an STM measurement. The conventional theories of STM, however, are based on a first order perturbation approximation [48, 49, 50] which does not include the tip-surface interaction. STM images are then interpreted simply as a convolution of the tip wavefunction and the

surface wavefunction. Although this interpretation is a very useful approximation for many applications, there may exist systems for which the tip-surface interaction and the surface dynamics play a crucial role in the STM measurement process.

In this letter we use *ab initio* total energy pseudopotential calculations, with a conjugate gradient scheme, to demonstrate that the Si(100) surface is an example of a system for which STM does not provide a direct mapping of the surface atomic structure, and that a conventional interpretation of the STM images is not appropriate. Typically, a room temperature STM image of the Si(100) surface [51, 52, 53] shows the majority[1] of dimers in, what appear to be, unbuckled, symmetric configurations. Such configurations are in apparent disagreement with the theoretical predictions of buckled, *asymmetric* dimer configurations [54]. One might expect that this discrepancy could be reasonably resolved by arguing that thermal fluctuations in the asymmetric dimer configurations will create an averaged or "symmetric" image. Such thermal fluctuations have been predicted to be present on the surface *in the absence of a tip*[2] [55, 56]. In the presence of a tip, however, we propose that a different mechanism is operational. Specifically, we demonstrate that the tip-surface interactions are significant enough to flip and bind an asymmetric dimer to the tip. As the tip is then moved along the surface, dimers are flipped tracking the tip and create what appears to be a symmetric image in the scan.

5.2 Calculational Details

The *ab initio* total energy pseudopotential density functional calculations are performed using the preconditioned conjugate gradients scheme for the electronic energy minimization to the Born-Openheimer surface [2]. The minimum energy ion configuration on the Born-Openheimer surface is obtained by relaxing ions according to the Hellman-Feynman forces. Within the local density approximation (LDA), the total energy functional is calculated with the Perdew-Zunger parameterization of the

[1]The dimers that are in the vicinity of defects appear to be pinned in asymmetric configurations.
[2]At room temperature for dimers not pinned directly to defects.

Table 5.1: Calculated lattice constants and bulk moduli of tungsten crystal and silicon crystal are compared with experimental values.

	Experiment	Calculation	Difference
W lattice constant (Å)	3.16	3.13	0.9%
W bulk modulus ($10^{12} dyn/cm^2$)	3.23	3.47	7.4%
Si lattice constant (Å)	5.431	5.427	0.7%
Si bulk modulus ($10^{12} dyn/cm^2$)	0.988	1.013	2.5%

exchange-correlation energy [57] and the Kleinman-Bylander separable form of the nonlocal ionic pseudopotentials [58]. The pseudopotentials for Silicon and Tungsten are generated by the kinetic energy optimization [59], and contain p and d nonlocal components and a s local component.

The convergence of the plane wave expansions and the transferability of the pseudopotentials are tested for bulk silicon crystal and bulk tungsten crystal. From the test calculations, the plane wave cutoff energy is chosen to be $E_c = 300eV$ at which the total energy of the silicon crystal is converged to within 0.04% and that of the tungsten crystal is to 0.07%. The transferability of the pseudopotentials are fairly good as shown in Table I for the calculations of the bulk lattice constants and the bulk moduli.

The STM tip-surface system is modelled by a supercell (15.35Å$\times$ 8.58Å$\times$ 16.00Å) containing 52 atoms (4 tungsten atoms, 32 silicon atoms, and 16 hydrogen atoms). The corresponding Brillouin zone is sampled with one **k** point (Γ). The 32 silicon atoms form a four layer slab with eight atoms in each layer (15.35Å$\times$ 8.58Å)[3]. The four dimers in the top layer form a $c(4\times 2)$ surface reconstruction, and the slab is vertically separated from the periodic images by 10Å vacuum regions. The bottom layer silicon atoms are fixed at bulk positions, and all the dangling bonds are passivated by 16 hydrogen atoms. To model the STM tip we note that only the atoms at the very edge of the tip need to be adequately represented in order to address the questions raised in this work. Since W atoms on the surface form a closed-packed structure,

[3]The interdimer interaction is stronger along the dimer rows (-0.026eV) than across the dimer rows (0.010eV), and the separation distances are chosen to avoid the correlated interaction of STM tips and the surface.

we have opted to represent the apex of the STM tip simply as a tetrahedron of four W atoms. The tungsten cluster is placed in the vacuum region with an apex atom pointing down to the surface. In the calculations, the silicon atoms in the top three layers and the apex atom are allowed to relax according to the Hellman-Feynman forces.

To gauge the influence and relative importance of the tunneling current or bias voltage, we performed the following exercise. Typically the bias voltage is 2V, and the tip-surface separation is about 5Å so that the electrostatic force on a surface atom is approximately 0.6 eV/Å. This includes a conservative estimate of 1.5 for the enhancement factor caused by inhomogeneous field effects around the surface atoms as discused by Kreuzer, Wang, and Lang [60]. The spring constant of a surface mode is roughly 5eV/Å^2, so that the relaxation energy of the atom due to the applied bias voltage is less than $0.036eV$, which is consistent with *ab initio* calculations of the tip-induced polarization of the Si(100) surface by Huang *et al.* [61]. As we shall see in the results below, this energy is much smaller than our calculation of a tip-surface binding energy of $0.2eV$. We thus neglect the effects of the bias voltage in forthcoming analysis.

In these calculations, we allowed the tip to vary in the range of 4.5 to 5.2Å above the atoms in the outermost surface layer. As shown in Figure 5-1, even for the shortest tip-surface distance of 4.5Å, the surface is not greatly perturbed by the presence of the tip, and no new bonds are formed between them. Nevertheless, as we discuss in the next section, there is enough interaction between tip and surface to significantly alter the dynamics of the surface dimers.

5.3 Interaction Energies

The tip-surface interaction energy is calculated by combining three separately calculated energies: $E(tip)$, $E(surface)$, and $E(tip + surface)$. $E(tip)$ is calculated by retaining the tip in the supercell and removing the Si slab. Similarly, $E(surface)$ is calculated by retaining the slab and removing the tip. Finally, the energy of the

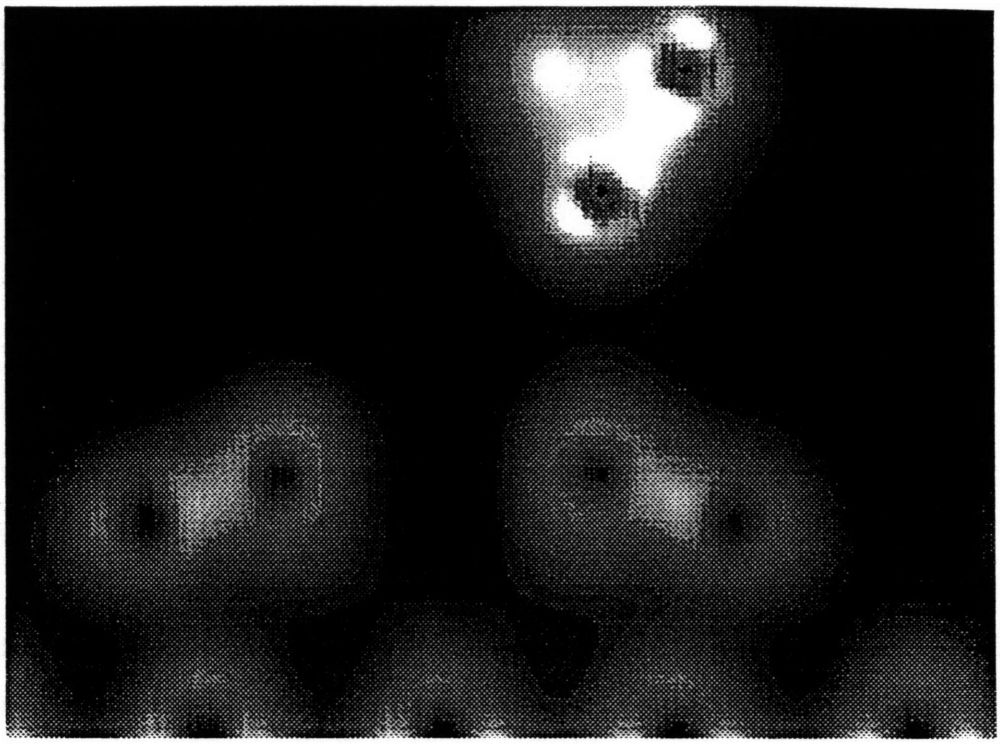

Figure 5-1: This plot shows a cross section of the total charge density of the tip-surface system with the tip directly above an upper dimer atom. The buckling angle of the dimer, the position of the apex tip atom, and the charge density distributions of the tip and the dimer are not significantly changed by the tip-surface interaction, but the interaction energy is significant ($-0.57eV$).

tip-surface system $E(tip + surface)$ is calculated with both the tip and the slab in the supercell. The tip-surface interaction energy is then simply

$$E_{int} = E(tip + surface) - E(tip) - E(surface). \tag{5.1}$$

The results of our calculations for a tip restricted to lie directly above a surface atom are summarized in Figure 5-2. For the configuration shown on the left panel, the tip lies 5.2Å above the lower dimer atom, and the interaction energy is $-0.37eV$. The panel at the center of the figure refers to a symmetric dimer configuration that corresponds to the "saddle-point" or static barrier configuration for flipping the buckled dimer. In the absence of the tip, the barrier is calculated to be $0.08eV$ in good agreement with $0.09eV$ as obtained by Dabrowski and Scheffler [56]. In the presence of the tip, the barrier for an *up-flip* of the buckled dimer is found to be $0.1eV$. The opposite barrier, corresponding to a *down-flip* of the buckled dimer, is obtained from the right panel of Figure 5-2 and is found to be $0.3eV$. Note that the interaction energy in the latter case is correspondingly large at $-0.57eV$ and the distance between tip and dimer atom is 4.5Å.

To determine how this barrier changes with respect to the position of the tip, we perform the calculations illustrated in Figure 5-3. Now the tip is restricted to lie directly above a dimer-*bond*. In this case, we find that the barrier decreases significantly to a value of about $0.05eV$.

5.4 Implications

For a given value of energy barrier, E_b, the average time that a dimer spends in one asymmetric configuration before flipping to the other is simply

$$\tau_b = 10^{-13} e^{E_b/k_B T}, \tag{5.2}$$

where the phonon frequency is estimated to be $10^{13} sec^{-1}$. During an STM measurement, an STM tip typically stays $3 \times 10^{-3} sec \equiv t_{STM}$ above a surface atom and

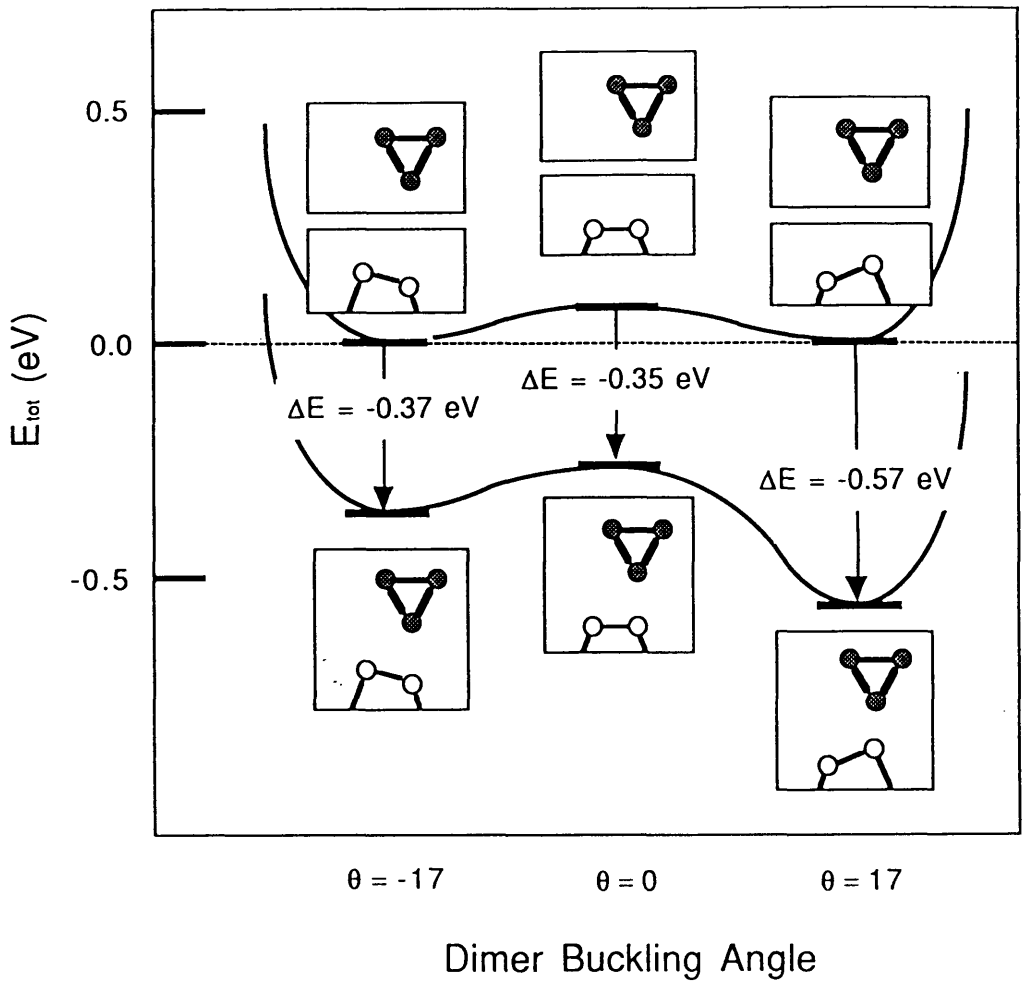

Figure 5-2: Total energy (in eV) of a tip-surface system as a function of surface-dimer buckling angle. The tip (shown schematically as a triangle with filled circles) is situated directly above a surface-dimer atom (open circles). The results at and above the horizontal dashed line correspond to a tip-surface system in the *absence* of interactions. In this case the horizontal bars correspond to $E(tip)+E(surface)$. Note that the barrier for flipping from one asymmetric dimer configuration to the other is about 0.08eV. The panels below the dashed line correspond to the fully interacting tip-surface system. In this case the horizontal bars correspond to $E(tip+surface)$. Note that the barriers for up-flip and down-flip are 0.1eV and 0.3eV respectively.

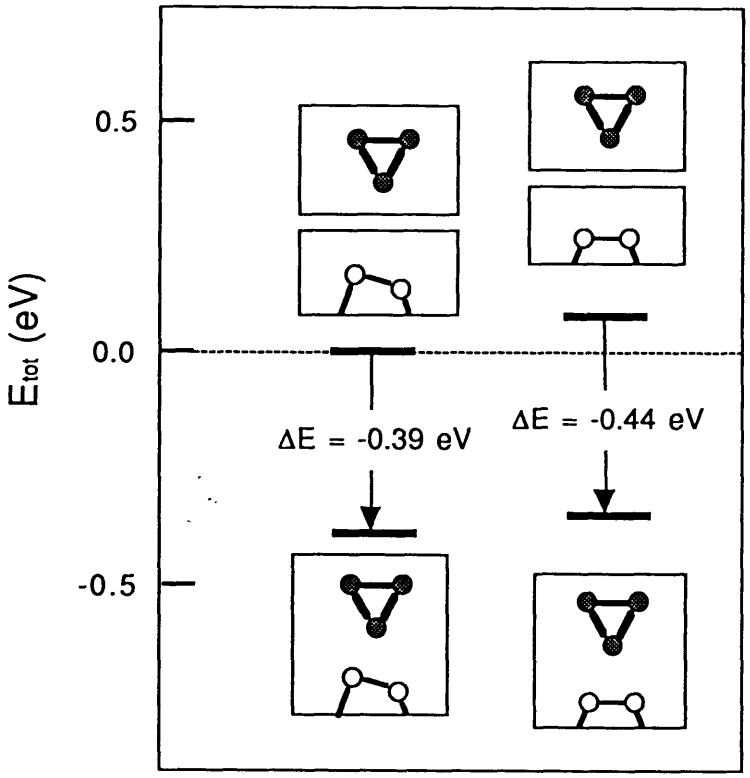

Figure 5-3: Total energy (in eV) of a tip-surface system as a function of surface-dimer buckling angle for a tip situated directly above the dimer bond. Same convention as in Figure 5-2. Note that the barrier for dimer flipping is now reduced to 0.05eV.

therefore the relative values of τ_b and t_{STM} will determine the nature of the STM image. In the *absence of interactions* between the STM tip and surface, a buckled dimer is in a symmetric potential-well as shown in the upper curve of Figure 5-2, and the energy barrier for flipping $(0.08 - 0.09eV)$ is small enough that at room temperature the dimer can flip up and down very frequently ($\tau_b = 2 \times 10^{-12} sec$). This would lead to a symmetric STM image that is the *average* of up-flip and down-flip configurations.

In the *presence of interactions* between the STM tip and surface, a buckled dimer is in an *asymmetric* potential-well as shown in the lower curve of Figure 5-2, and τ_b is different for the down-flip and the up-flip configurations. At room temperature, τ_b's are short enough ($\tau_{down} = 5 \times 10^{-12} sec$ and $\tau_{up} = 1.3 \times 10^{-8} sec$) that, in principle, the dimer can flip up and down freely, and thermal equilibrium between two local energy minima of the asymmetric potential is reached during the STM imaging time. Therefore, the dimer spends different amounts of time in each local energy minimum, and the ratio of the times is given by the Boltzmann factor of the difference of two local minimum energies (4×10^{-4}). Consequently, the dimer stays *in the up-flip configuration* except for intermittent rapid *round-trips* to the down-flip configuration. For all practical purposes, therefore, one is always measuring a dimer in the up-flip position as the tip moves along the surface. The resulting image is then deceptively that of a "symmetric" dimer.

As one decreases the temperature, τ_{down} and τ_{up} increase and eventually both become larger than t_{STM}. This occurs at and below a temperature $T_{freeze} = 48K$ for which the surface dynamics is so slow that a dimer cannot flip during the STM imaging time. Therefore, at this temperature range one can observe frozen buckled dimers in up-flip and down-flip positions from an STM image of the surface.

One possible experimental verification of our prediction regarding the room temperature "symmetric" dimer image would be to analyze the tunneling current while the tip remains above a dimer atom. If tip-surface interactions are *not* important the current should have the characteristics illustrated in the top panel of Figure 5-4. The typical frequency at room temperature in this case should be around $10^{12} Hz$. On the other hand, if tip-surface interactions are important, and result in a "binding" of

the up-flip configuration, one should observe a current as shown schematically in the bottom panel of Figure 5-4. The frequency associated with these "glitches" should be in the neighborhood of $10^8 Hz$.

Finally, a special case can arise if the STM tip is constrained to move precisely along the dimer axis. Recall that in this case there exists a lower barrier when the tip is situated directly above a dimer bond (see Figure 5-3). Consequently, as the STM tip moves along the dimer, the dimer can flip more easily which results in a lower freeze-in temperature of about $24K$.

5.5 Concluding Remarks

In all of this work we have specifically focussed on the defect free regions of the Si(100) surface. However, defects, such as vacancies and step-edges for example, appear to occur frequently on such surfaces. STM images at room temperature reveal *asymmetric* dimer configurations in the vicinity of such defects which would be consistent with a defect-pinning mechanism that leads to either a higher energy barrier for an up-flip and down-flip *or* a larger asymmetry between the barriers for up-flip and down-flip. We have recently begun attempts to investigate these differences but such *ab initio* calculations are beyond the scope of the present work.

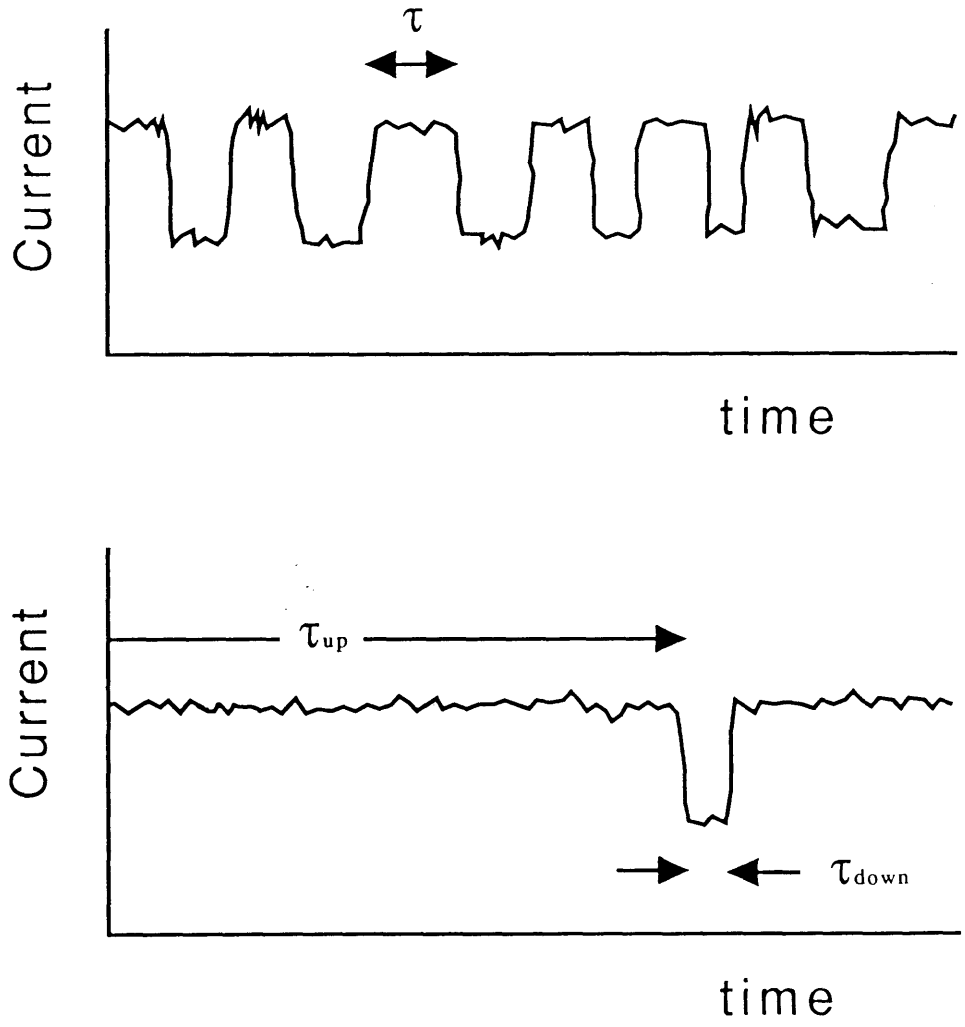

Figure 5-4: Top panel shows a schematic tunneling current in the absence of tip-surface interactions. Bottom panel shows a schematic tunneling current in the presence of tip-surface interactions.

Chapter 6

Mechanical Hysteresis on Atomic Scale

A mechanical hysteresis associated with *intimate* atomic force microscopy (AFM) on the Si(100) surface is studied with *ab initio* total energy pseudopotential density functional calculations. It is found for a tip-surface separation of about 2Å that a vertical movement of the AFM tip can induce a hysteresis effect on the geometry of surface dimers accompanied by a *discontinuous* change of the surface dimer angle. It is also found that a bond may form between the tip apex atom and a surface dimer atom, and this bond facilitates the change of dimer geometry between local minimum energy configurations while the tip moves down and up.

6.1 Introduction

Both atomic force microscopy (AFM) and scanning tunneling microscopy (STM) provide real space images of a crystal surface with atomic scale resolutions [62, 47]. However, the basic principles of AFM and STM are quite different: i.e., AFM is based on the interatomic forces between the AFM tip atoms and surface atoms, whereas STM is based on the tunneling currents between them. Since the interatomic forces do not depend on the details of the electronic structures of the tip and surface surface as much as the tunneling currents do, the interpretation of an AFM image is generally

believed to be much simpler than that of an STM image [63].

For the interpretation of an AFM image or an STM image, the conventional theories make several simplifying assumptions which provide approximate descriptions of the AFM and the STM processes. In the AFM process, the surface atoms are assumed to deform *elastically* under the force applied by an AFM tip, and the tip is generally assumed to be rigid so that the tip-surface interaction is described by a simple force-distance curve [63]. On the other hand, in the STM process the tip-surface interactions and the surface dynamics are generally ignored [48]. However, in Chapter 5 we have shown that the tip-surface interactions and the surface dynamics are crucial for the correct interpretation of the symmetric dimer image on the Si(100) surface [18]. In particular, we have discussed a situation in which the STM tip effectively *captures* a fluctuating surface dimer in an *up-flip* asymmetric dimer configuration at a temperature higher than 48K. In this case, the capture mechanism is possible due to the thermal fluctuations of the dimer configuration, and as the STM tip moves away from the surface dimer, the dimer resumes its normal thermal fluctuations between the up-flip and the down-flip configurations.

In this chapter, we use *ab initio* total energy pseudopotential calculations to study the microscopic mechanical changes associated with intimate AFM on the Si(100) surface. The calculations show that for a tip-surface distance of about 2Å an AFM tip can *push down* a surface dimer from the up-flip configuration to the down-flip configuration as one brings the tip down and *pull* it *up* again as one brings the tip up. In this procedure the dimer geometry follows two different paths with a discontinuous change of the dimer angle along the down path, and exhibits a mechanical hysteresis effect. The energy barrier separating two paths is small (0.05 eV) so that the hysteresis loop is relevant only at low temperature. At room temperature the hysteresis loop will reduce to a thermally averaged curve.

6.2 Calculations

In the *ab initio* total energy pseudopotential calculations, we use the local density approximation (LDA) of the density functional theory and minimize the electronic energy using the preconditioned conjugate gradients scheme [2]. The LDA calculations are performed with the Perdew-Zunger parameterized exchange-correlation energy [57], and the Kleinman-Bylander separable form of optimized pseudopotentials [58, 59].

The tip-surface system is modeled by a supercell (15.35Å × 8.58Å × 16.00Å), and the plane wave cutoff energy is chosen to be $E_c = 300eV$. This system requires a fast Fourier transform (FFT) box size of 128 × 64 × 128 and 33699 plane wave basis functions. The Brillouin zone sampling is performed with one **k** point (Γ).

The supercell contains 32 silicon atoms that form a four layer slab with eight atoms in each layer, 16 hydrogen atoms that are used to passivate the dangling bonds of the bottom layer silicon atoms, and 4 tungsten atoms that are used as a tip. The top layer silicon atoms form a $c(4 \times 2)$ surface reconstruction, and the bottom layer silicon atoms are fixed at bulk positions. The vacuum region between the silicon slab and its periodic image is 10Å. The apex of the AFM tip is modeled by a tungsten tetrahedron cluster, and the cluster is placed in the vacuum region with an apex directed down to the silicon surface.

The tip is placed directly above an upper dimer atom, and the calculations are performed for a series of tip-surface distances, 4.5Å, 3.5Å, 3.0Å, 2.5Å, 2.25Å, 2.0Å, 1.75Å, and 1.5Å for the down path and 2.5Å, 3.0Å, 3.5Å, and 4.5Å for the up path[1]. The calculations are performed in sequence so that the surface geometry of the previous tip position is used as the initial geometry of the calculation with new tip position. For each calculation with a fixed tip-surface distance, the tungsten atom at the apex of the tip and top three layers of silicon atoms are allowed to relax according to the Hellman-Feynman forces so that the three tip atoms and the bottom layer silicon

[1]The tip-surface distance is defined to be the distance between the apex tip atom and the upper dimer atom under the tip before the relaxation of the tip-surface system.

atoms play the role of the macroscopic tip and the bulk silicon crystal. The atoms are relaxed until the Hellman-Feynman forces are smaller than 0.1eV/Å. The force on the AFM tip is then calculated from the Hellman-Feynman forces on the three fixed tip atoms.

6.3 Relaxation of the Tip-Surface System.

- When the tip and the surface are initially combined into a single system, there are large forces on the tip atoms and the dimer atoms. For example, at the tip-surface distance of $d_{tip-surface} = 1.5$Å, the vertical force on the tip apex atom is 49.6 eV/Å, and the vertical force on the upper dimer atom under the tip is -56.3 eV/Å, and at $d_{tip-surface} = 3.5$Å, -1.38 eV/Å and 0.98 eV/Å respectively. These forces lead to the relaxation of the tip apex atom position and the surface dimer structure. Figure 6-1 shows the cross sections of the total charge density of the tip-surface system after the relaxation. Four panels in Figure 6-1 correspond to the sequence of decreasing the tip-surface distances, 2.5Å, 2.25Å, 2.0Å, and 1.75Å. This sequence shows that as the AFM tip moves down, it *pushes down* and *flips* the surface dimer. The sequence (a), (b), and (c) shows a gradual decrease of the dimer angle (17°, 12°, and 2°), but the change of the dimer angle between (c) and (d) appears *discontinuous* (from 2° to -24°). To test the discontinuity of the dimer angle as a function of $d_{tip-surface}$, we performed the following exercise. We start from the relaxed atomic positions of the calculation at $d_{tip-surface} = 2.0$Å, slightly move down the AFM tip to $d_{tip-surface} = 1.9$Å, and let the tip-surface system relax. This small change of 0.1Å is found to be large enough to push the dimer over the static barrier of symmetric configuration, and the dimer geometry relaxes toward the flip-down configuration.

However, as the AFM tip moves up, the dimer configuration changes continuously as shown in Figure 6-2. From the sequence of top to bottom, the tip-surface distance increases from 1.75Å to 2.5Å to 3.0Å to 3.5Å, and the dimer angle increases gradually. This different behavior of dimer geometry indicate that the dimer configuration follows two different local minimum energy paths as the tip moves down and up.

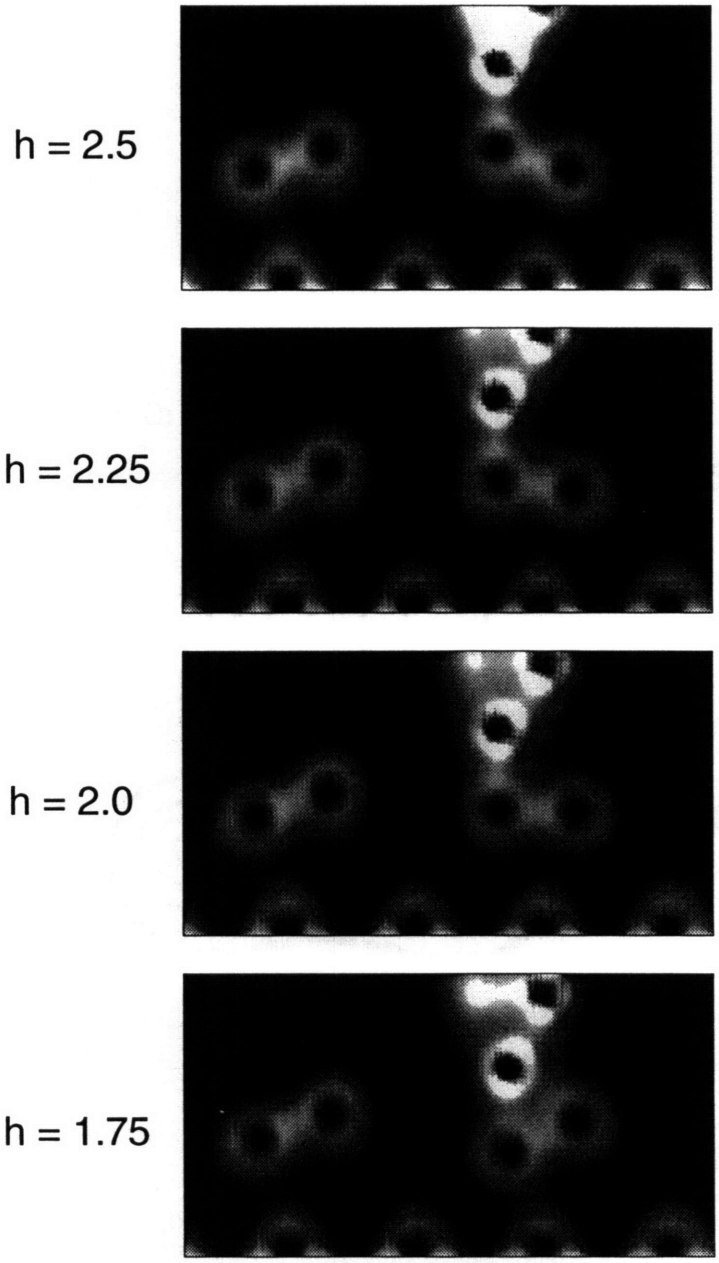

Figure 6-1: The sequence of charge density cross sections (from top to bottom) as the tip pushes down and flips the dimer.

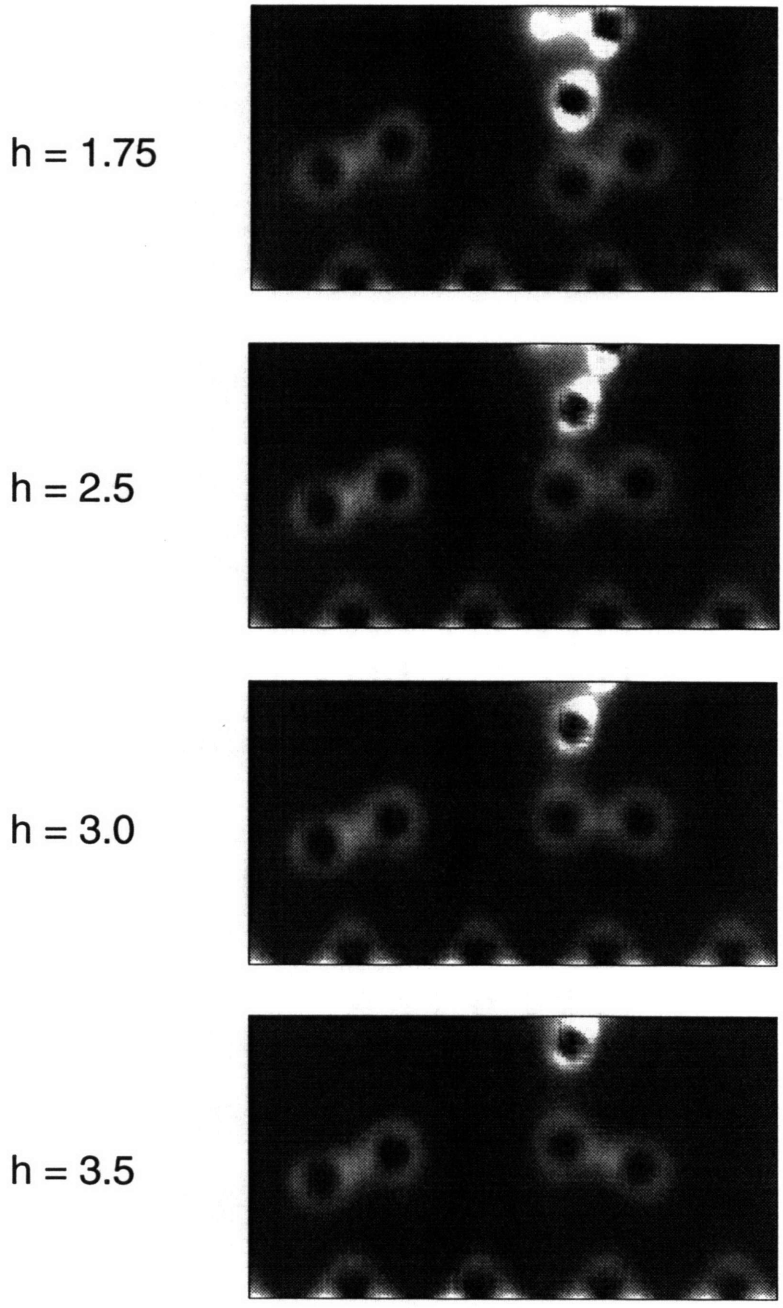

Figure 6-2: The sequence of charge density cross sections (from top to bottom) as the tip pulls up and flips the dimer.

6.4 Hysteresis Loops

The change of dimer geometry in response to the tip-surface interaction is quantitatively characterized by the dimer angle and the center of mass (CM) of dimer atoms. These two parameters provide a quantitative measure of the hysteresis effect observed in Figures 6-1 and 6-2. Figure 6-3 plots the dimer angle as a function of the tip distance from the surface for both paths of bringing the tip down and up as indicated by arrows in the plot. As noted before the down path shows a discontinuous change of the dimer angle, whereas the up path shows a continuous change. To test the temperature effect on the hysteresis effect, the static energy barrier of symmetric dimer configuration at the tip-surface distance of 2.5Å is calculated. The barrier height is 0.05 eV, and this value is small enough that the hysteresis loop will reduce to an average curve at room temperature.

Figure 6-4 shows the hysteresis loop projected onto the dimer CM height as a function of the tip-surface distance. This plot shows that the dimer CM height is about 0.5 Å larger for the up path, and indicate that the dimer is bound to the tip. However, it also indicate that the tip-dimer binding is not strong enough to break the dimer-substrate binding so that at a larger tip-surface distance the dimer is separated from the tip and returns the initial ground state geometry.[2]

6.5 Experimental Implications

The hysteresis loop of the dimer geometry can be detected by measuring the force on the AFM tip in a low temperature AFM experiment. The theoretical prediction of the force-distance hysteresis loop is shown in Figure 6-5. As the tip approaches the surface from the distance of 5.0 Å along the down path, the force becomes quite attractive at $d_{tip-surface} = 3.5$Å, decreases to zero as $d_{tip-surface}$ decreases, and becomes slightly repulsive at $d_{tip-surface} = 2.0$Å. This part of the curve is consistent with the simple

[2]Even though this tip-surface binding fails to break the dimer from the surface, it is possible to break a weakly bound atom from the surface. Bias voltage induced transfer of Si adatom on the Si(111)-(7 × 7) surface is an example of large enough tip-surface binding.

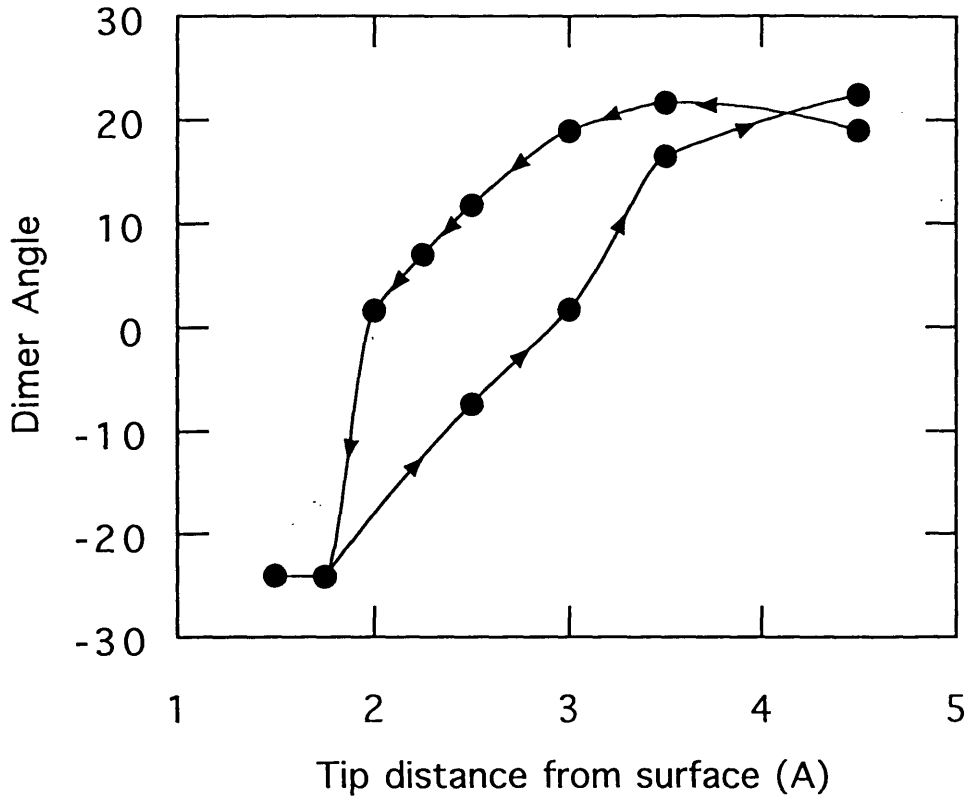

Figure 6-3: The projection of the hysteresis loop onto the dimer angle component. Left arrows indicate the path of bringing the tip down to the surface, and right arrows indicate the path of bringing the tip up from the surface.

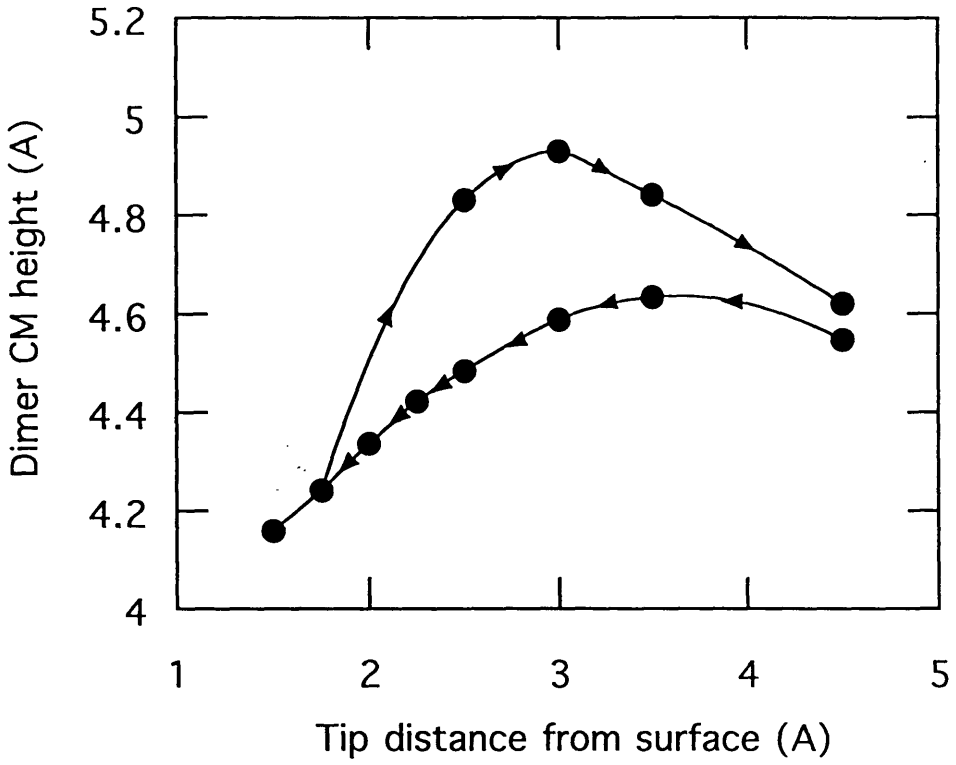

Figure 6-4: The projection of the hysteresis loop onto the dimer CM height component. Left arrows indicate the path of bringing the tip down to the surface, and right arrows indicate the path of bringing the tip up from the surface.

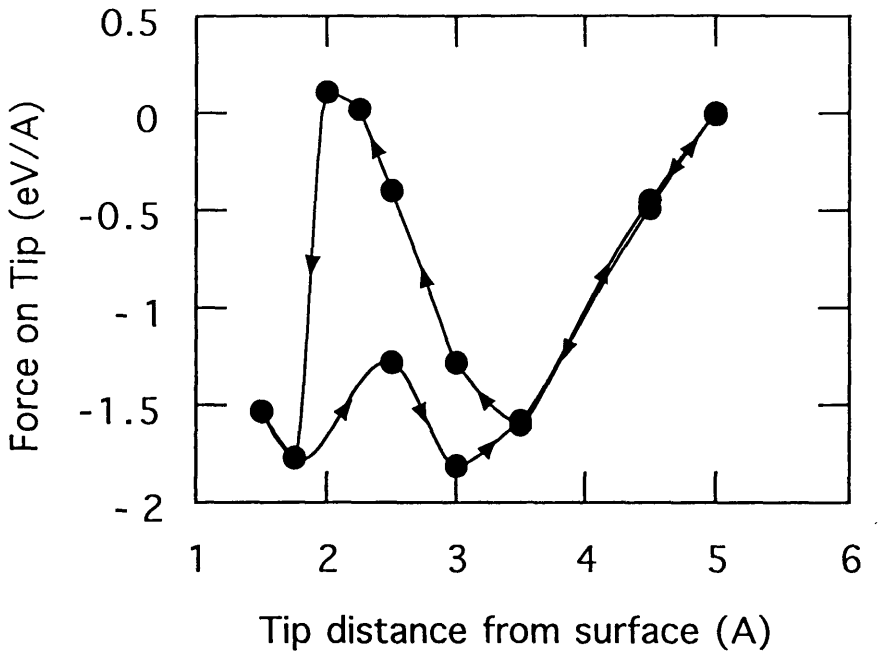

Figure 6-5: Hysteresis loop of the force on the AFM tip as the tip moves down (left arrows) and up (right arrows).

force-distance curve, but as the tip moves down further the simple force-distance curve is not valid any more. The force becomes quite attractive discontinuously as the dimer flips for $d_{tip-surface} < 2.0$Å and starts to be repulsive again.

However, as the tip moves up, the force on the tip shows less dramatic behavior. The attractive force shows a slight decrease and increase as the dimer flips from the down configuration to up configuration, and then follows the same curve as that of the down path.

This hysteresis loop of the force illustrates the limitation of the simplifying assumption on the tip-surface interaction which assumes that the tip-surface interaction is similar to interatomic interactions. Since the surface has multiple local minimum energy configurations, the tip-surface interaction involves the relaxation of the surface geometry leading to a hysteresis effect. If an AFM experiment is performed at low temperature, this hysteresis effect will strongly influence the AFM image. If an AFM experiment is performed at room temperature, the hysteresis loop reduces to an average curve due to surface dynamics, and an AFM image is influenced by both

the hysteresis effect and the surface dynamics. Therefore, an image obtained in an AFM experiment is not a direct mapping of the surface structure, but a result from the combination of surface structure, surface dynamics, and the hysteresis effect.[3]

6.6 Concluding Remarks

We have studied the microscopic details of the AFM process on the Si(100) surface and discovered the complicated nature of the tip-surface interaction which leads to the tip-surface bond formation and the mechanical hysteresis of the surface dimer. All these microscopic behaviors of the tip-surface system show that the simplifying assumptions of the conventional AFM theories are generally not valid. The tip induced modifications of the surface structure are also relevant to the surface defect structures, the surface adatom clusters, and the surface steps. The study of these systems will provide an understanding of the microscopic process of the imaging of complicated surface structures in the AFM.

[3]This result is very similar to the interpretation of the STM image of Chapter 5.

Chapter 7

Microplastic Deformations in Atomic Force Microscopy

The microscopic deformations associated with *intimate* atomic force microscopy (AFM) on the Si(100) surface are studied with *ab initio* total energy pseudopotential density functional calculations. It is found for a tip-surface separation of about 2Å that the AFM tip can induce a *plastic* deformation of the surface. It is also found that a bond may form between the tip apex atom and a surface atom. These results show that the conventional interpretation of an *elastic* response of the surface atoms to the force applied by the AFM tip does not hold under the present conditions. The ramifications of these results for using Si(100) as an ultra-high density storage device are briefly discussed.

7.1 Introduction

Both atomic force microscopy (AFM) and scanning tunneling microscopy (STM) provide real space images of a crystal surface with atomic scale resolutions [62, 47]. However, the basic principles of AFM and STM are quite different: i.e., AFM is based on the interatomic forces between the AFM tip atoms and surface atoms whereas, STM is based on the tunneling currents between them. Since the interatomic forces do not depend on the details of the electronic structures of the tip and the surface as

the tunneling currents do, the interpretation of an AFM image is generally believed to be much simpler than that of an STM image [63].

For the interpretation of an AFM image or an STM image, the conventional theories make several simplifying assumptions which provide approximate descriptions of the AFM and the STM processes. In the AFM process, the surface atoms are assumed to deform *elastically* under the force applied by an AFM tip, and the tip is generally assumed to be rigid [63]. On the other hand, in the STM process the tip-surface interactions and the surface dynamics are generally ignored [48]. However, in a recent work we have shown that the tip-surface interactions and the surface dynamics are crucial for the correct interpretation of the symmetric dimer image on the Si(100) surface [18]. In particular, we have discussed a situation in which the STM tip effectively *captures* a fluctuating surface dimer in an *up-flip* asymmetric dimer configuration at a temperature higher than 48K. In this case, the capture mechanism is possible due to the thermal fluctuations of the dimer configuration, and as the STM tip moves away from the surface dimer, the dimer resumes its normal thermal fluctuations between the up-flip and the down-flip configurations.

In this chapter, we use *ab initio* total energy pseudopotential calculations to study the microscopic deformations associated with intimate AFM on the Si(100) surface. The calculations show that for a tip-surface distance of about 2Å another capture mechanism of tip-surface interactions is operational in which an AFM tip can *capture* a surface dimer in the down-flip configuration and then *pull* it *up* to the up-flip configuration. This second mechanism leads to a *plastic* deformation of the surface dimer when the thermal fluctuations of the dimer are suppressed. This suppression can occur conservatively for temperatures lower than 48K, or at higher temperatures if the dimer is in the vicinity of a defect.

7.2 Calculations

In the *ab initio* total energy pseudopotential calculations, we use the local density approximation (LDA) of the density functional theory and minimize the electronic

energy using the preconditioned conjugate gradients scheme [2]. The LDA calculations are performed with the Perdew-Zunger parameterized exchange-correlation energy [57], and the Kleinman-Bylander separable form of optimized pseudopotentials [58, 59].

The tip-surface system is modeled by a supercell (15.35Å $\times$ 8.58Å $\times$ 16.00Å), and the plane wave cutoff energy is chosen to be $E_c = 300eV$. This system requires a fast Fourier transform (FFT) box size of 128 $\times$ 64 $\times$ 128 and 33699 plane wave basis functions. The Brillouin zone sampling is performed with one **k** point (Γ).

The supercell contains 32 silicon atoms that form a four layer slab with eight atoms in each layer, 16 hydrogen atoms that are used to passivate the dangling bonds of the bottom layer silicon atoms, and 4 tungsten atoms that are used as a tip. The top layer silicon atoms form a $c(4 \times 2)$ surface reconstruction, and the bottom layer silicon atoms are fixed at bulk positions. The vacuum region between the silicon slab and its periodic image is 10Å. The apex of the AFM tip is modeled by a tungsten tetrahedron cluster, and the cluster is placed in the vacuum region with an apex directed down to the silicon surface.

The tip is placed directly above a lower dimer atom, and the calculations are performed in two sequences of tip-surface distances, the capture sequence (5.2Å, 4.3Å, 4.2Å, 3.95Å, 3.7Å, and 3.2Å) and the pull-up sequence (3.2Å, 4.35Å, 4.45Å, 5.2Å). For each calculation with a fixed tip-surface distance, the tungsten atom at the apex of the tip and top three layers of silicon atoms are allowed to relax according to the Hellman-Feynman forces so that the three tip atoms and the bottom layer silicon atoms play the role of the macroscopic tip and the bulk silicon crystal. The atoms are relaxed until the Hellman-Feynman forces are smaller than 0.1eV/Å. The force on the AFM tip is then calculated from the Hellman-Feynman forces on the three fixed tip atoms.

7.3 Tip-induced Plastic Deformation of Surface

The results of the calculations are summarized in Figure 7-1. Top two panels show charge density cross sections of the initial and the final states of the capture sequence. At the tip-surface distance of 3.2Å, the dimer is captured by the tip, and the bonding charge is visible between the tip atom and the dimer atoms. Bottom two panels show an intermediate and the final state of the pull-up sequence. By these two sequences of tip movement the dimer is flipped from the down-configuration to the up-configuration.

The relaxation of the tip-surface system shows that the intrinsic dimer structure on the Si(100) surface determines the response of the surface atoms to the force applied by the AFM tip. The double potential well structure of the dimer configuration makes it possible for a dimer to stay in either local minimum energy configuration, and leads to a change of the surface structure under the influence of the AFM tip. In the absence of the thermal flipping of the dimer at a low temperature, the surface dimer will stay in the deformed configuration even after the AFM tip moves away from the dimer. Therefore, this mechanism leads to a *microscopic* scale *plastic deformation* of the Si(100) surface in the AFM.

Generally, this type of plastic deformation of the surface is expected to happen for any reconstructed surfaces with the reconstruction unit which has multiple minimum energy configurations. An AFM tip can induce a transition between local minimum energy configurations by lowering the potential barrier and stabilizing one configuration as shown in this work.

Furthermore, we have seen an indication that a bond is formed between the tip apex atom and a surface dimer atom, and this bonding is responsible to the change of dimer geometry between local minimum energy configurations. The tip-surface bonding length is about 2.35Å and changes only 0.05Å as the tip moves over the range of 3Å. This stability of the tip-surface bond is combined with the surface dimer structure to produce a complicated relaxation of the tip-surface system. Therefore, most generally the microscopic process of a low temperature AFM experiment involves

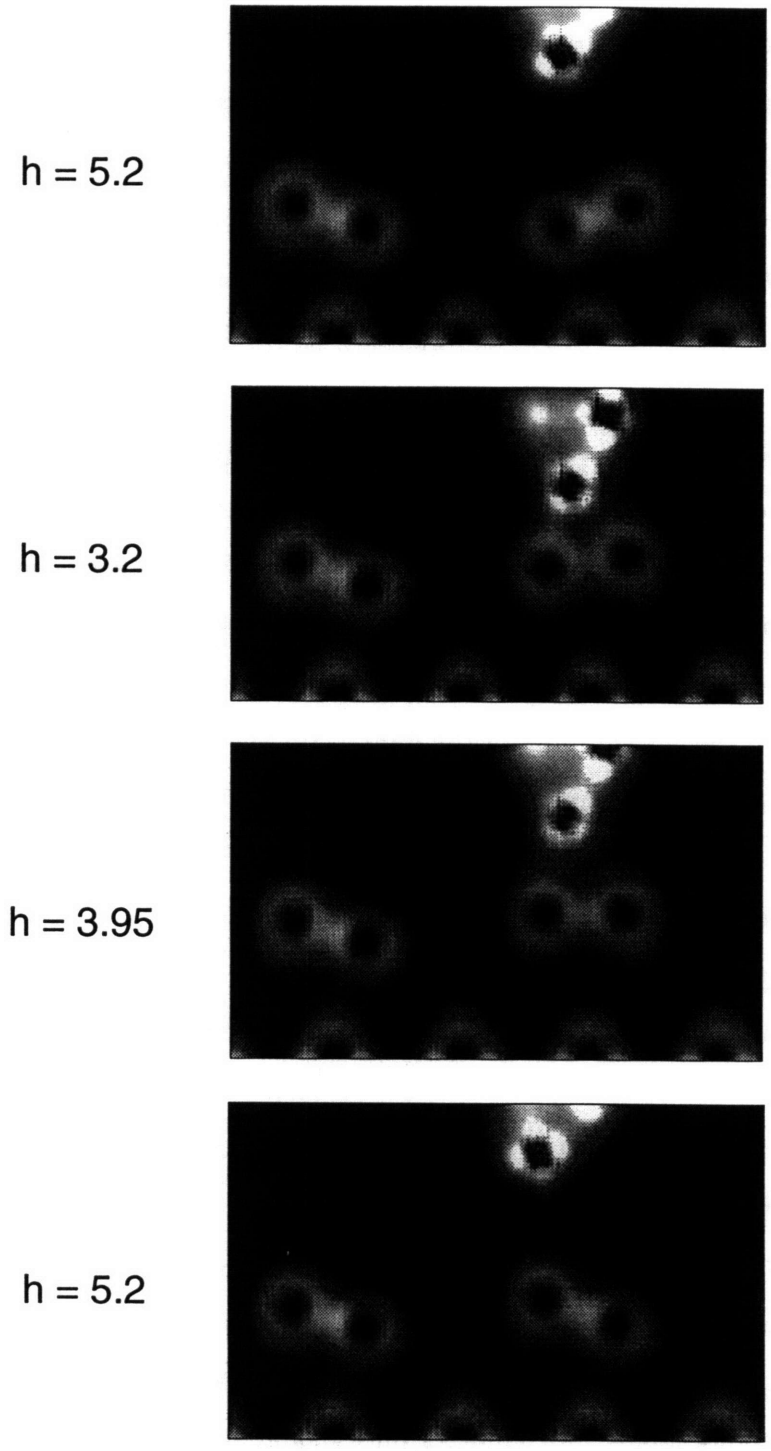

Figure 7-1: This plot shows a sequence of charge density cross sections in which the tip is lower to capture the dimer, and pull it up. The top panel and the bottom panel show the same tip-surface distance with different dimer configurations.

a complicated relaxation of the tip and surface system which depends on the intrinsic surface structures and the tip-surface interactions.

7.4 Application to Memory Device

This section describes an application of the microplastic deformation to the invention of a memory device which can store and retrieve data at ultra high density. The basic units of the device are a metallic scanning tip and the (100) surface of the diamond structure (silicon, germanium, or carbon).[1] The scanning tip operates as an atomic force microscope (AFM) to *store* the data on the (100) surface by modifying the configuration of the asymmetric dimers existing on the surface, and as a scanning tunneling microscope (STM) to *retrieve* the data from the (100) surface by reading the dimer configurations. This device can store one bit of information in a surface dimer so that the storage density is one bit per two surface atoms. For silicon this corresponds to 1 bit per 30Å^2 or 420 Gbytes per mm^2. Therefore, this invention represents several orders of magnitude increase of the storage density over conventional memory devices and closely approaches the ultimate limit of possible memory devices.

7.4.1 Introduction

A storage device has two basic units: a writing and reading device and a storage medium. The storage density of a storage device is determined by the size of the basic storage unit which can store one bit of data. This size is determined by the resolution of the writing and reading device which modifies the storage medium and retrieves the stored data.

One can easily imagine that the ultimate limit of a surface storage density is one bit of data per surface atom, and this limit provides an enormously higher storage density than any conventional storage devices. The realization of this limit requires both a writing and reading device with atomic resolution and a storage medium with

[1] As we discussed in section 7.3, any surface with multiple minimum energy configuration can be used as a storage medium.

a storage unit of atomic scale.

In this section, we describe a storage device which closely approaches this ultimate limit. This device uses the atomically sharp scanning tip of the atomic force microscope and the scanning tunneling microscope as the writing and reading device, and the (100) surface of the diamond structure (silicon, germanium, or carbon) as the storage medium with the surface dimer as the storage unit.

7.4.2 Basic Principle of Memory Storage at an Atomic Scale

The basic principles of the ultra high density storage device is the utilization of the interactions between the atomically sharp scanning tip and the surface atoms on the (100) surface. In the strong interaction limit, the tip can modify the configuration of surface dimers as a writing device. On the other hand, in the weak interaction limit, the tip is used as a reading device by a standard STM image scanning mode.

The storage of data on the (100) surface is realized by changing the configuration of a surface dimer between two energetically equivalent asymmetric dimer configurations. One can assign 0 and 1 for each dimer configuration. This is shown schematically in Figure 7-2. The microscopic process of changing the dimer configuration from one to the other is shown in Figure 7-1. The results here are for silicon and show four charge density cross sections of the tip-dimer system as the tip captures the dimer and pull it up.

7.4.3 Practical Considerations of Device Operation

The operation of the storage device requires a low temperature (e.g. for silicon 24K) and a high vacuum chamber. The low temperature condition is necessary to avoid the thermal fluctuations of the dimer configurations. The high vacuum condition is necessary to keep the (100) surface clean from contamination.

Under the above operation condition, the storage process and the retrieval process require the scanning rate of one scan per dimer row. In both processes, the scanning tip needs to be constrained to scan along the direction of dimer rows as illustrated in

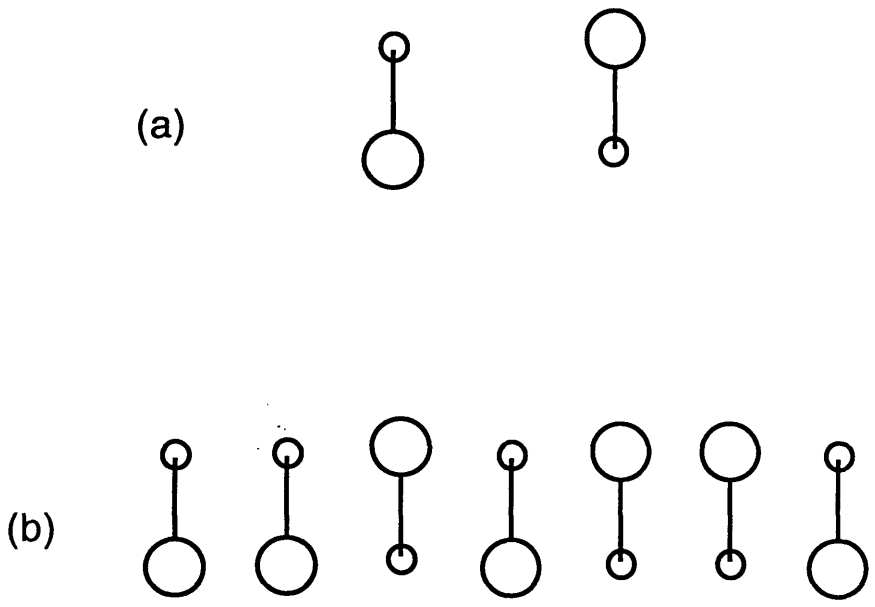

Figure 7-2: The top panel (a) shows two different dimer configurations of equivalent energy. The large open circles represent the upper dimer atoms, and the smaller open circles represent the lower dimer atoms. The dimers are represented as the connected unit of large and small circles. When one assigns 0 and 1 for each dimer configuration in (a), the bottom panel (b) shows a sequence of dimers corresponding to 0010110.

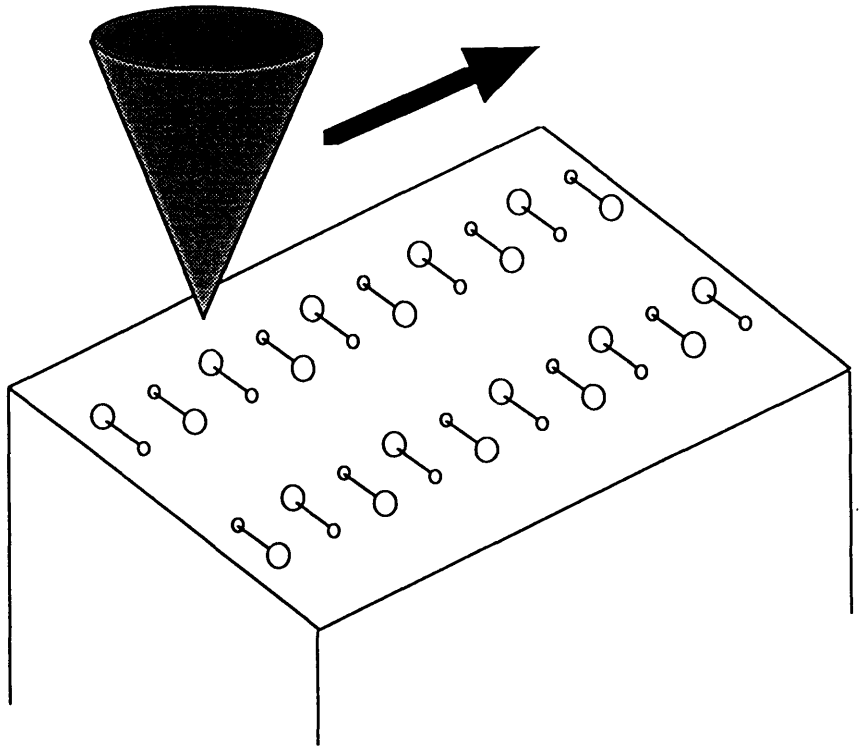

Figure 7-3: This plot illustrates the operation of the scanning tip above the (100) surface. The arrow indicates the direction of scanning along the dimer row.

Figure 7-3. The storage process requires a more complicated motion of the tip along the scanning direction. In order to save a sequence of data bits on a dimer row, the tip should move in such a way that it changes the configurations of the dimers in the row. This change of the configuration is achieved by the following sequence of motions: place the tip above the lower dimer atom, push the tip down and up until the dimer flips, and proceed to the next dimer. For the given sequence of data bits, the motion of the tip can be programmed and performed very fast.

On the other hand, the retrieval process is rather simple. The tip can scan over the dimer row along a straight line, and the measurement of the tunneling current simply determines the configurations of the dimers.

This device may also be able to operate at a higher temperature (possibly even room temperature) by preparing the (100) surface with surface defects which pin the nearby dimer configurations.

7.5 Concluding Remarks

We have studied the microscopic details of the AFM process on the Si(100) surface and discovered the complicated nature of the tip-surface interaction which leads to the tip-surface bond formation and the plastic deformation of the surface dimer. All these microscopic behaviors of the tip-surface system show that the simplifying assumptions of the conventional AFM theories are generally not valid. The tip induced modifications of the surface structure are also relevant to the surface defect structures, the surface adatom clusters, and the surface steps. The study of these systems will provide an understanding of the microscopic process of the imaging of complicated surface structures in the AFM. Finally, we note that the *plastic* deformation of the surface dimer can be utilized for the construction of an atomic scale data storage device. The storage density of this device will be much higher than any conventional devices.

Chapter 8

Ab initio Dynamics Study of Si(100) Surface

Ab initio dynamics study of the Si(100) surface at finite temperature shows the dynamical changes of the surface structures with microscopic details. The configuration of surface dimers changes from the ground state geometry as the surface system evolves dynamically at 900 K. The dimer bond length oscillates at $f = 10^{13} sec^{-1}$, and the dimer flipping time scale is about 100 fsec. The surface layer expands into the vacuum by 0.1 Å due to the thermal expansion. The dynamical change of the surface electronic structure shows the dynamic changes of the dimer bond strength and the Kohn-Sham eigenvalues which lead to the dynamical change of surface chemical reactivity.

8.1 Introduction

Most *ab initio* studies of surface structures are performed to investigate the ground state structure of a surface such as the surface reconstruction and the surface electronic structure. For a surface with a simple structure, the ground state structure is a good approximation to the surface structure at finite temperature so that one can directly compare the theoretical calculations with the experimental results obtained at finite temperature. However, for certain surfaces the surface structure may change

in a complicated way so that the ground state structure is *not* a good approximation to the surface structure at finite temperature.

To investigate this issue, we choose to perform an *ab initio* dynamics simulation of the Si(100) surface. The Si(100) surface has a simple unit of surface reconstruction, i.e., surface dimer, but the inter-dimer interaction leads to a larger reconstruction unit of $c(4 \times 2)$ which contains four surface dimers. A surface dimer can be in two equivalent asymmetric configurations, and the barrier for flipping a dimer from one configuration to another is about 0.1 eV.

One can see that the thermal fluctuations will lead to a complicated behavior of the surface as the dimers flip up and down at the same time interacting with each another. In addition to the geometrical change of the surface atoms, the electronic structure of the surface is also changing dynamically. In the following sections, I discuss the results of the dynamical calculations for the Si(100) surface at 900 K.

8.2 Calculations

The total energy pseudopotential density functional calculations are performed with the *ab initio* molecular-dynamics scheme implemented on Thinking Machines CM-2. Within the local density approximation (LDA), the total energy is calculated using the Perdew-Zunger parameterized exchange-correlation energy [57] and the Kleinmann-Bylander separable form for the ionic pseudopotentials with s and p nonlocal components and d local component [58, 59].

The supercell for the Si(100) surface calculation is chosen to include 256 silicon atoms with an inversion-symmetric geometry. This supercell contains a eight layer slab with four $c(4 \times 2)$ reconstruction units on each surface[1] and a vacuum region of 10 Å. The supercell size is 30.7Å$\times$ 15.4Å$\times$ 19.5Å, and the corresponding Brillouin zone is sampled with the Γ point. The calculation uses a 7.5 Ry cutoff for the plane wave basis expansion corresponding to 22,528 basis functions, and the fast Fourier transform box size is $128 \times 64 \times 64$.

[1] We chose this supercell so that each surface contains 16 asymmetric dimers.

Initially, the geometry of the surface atoms are optimized by moving the atoms according to the Hellmann-Feynman forces until they become smaller than 0.1 eV $Å^{-1}$ with two inner-most layer atoms fixed at bulk positions. This configuration corresponds to the zero potential energy configuration of ionic dynamics at zero temperature. To heat up the system to higher temperature, initial random velocity distribution of 900 K is assigned, and the dynamical trajectories of the ions are calculated with Verlet algorithm.

Since the ion system is not in a typical equilibrium configuration, the initial kinetic energy of ions flows into potential energy, and this flow of energy is compensated by rescaling the kinetic energy to 900 K until the system reaches a balance between the kinetic energy and the potential energy. After 20 iterations of dynamic evolution with a timestep of 3 fsec, the ion system reaches a balance of the kinetic energy and the potential energy. Subsequently, the system dynamics is performed without the velocity rescaling. The simulation has been performed for 80 fsec, and in the next sections I discuss the results from this preliminary calculation.

8.3 Dynamical Change of Surface Geometry

To study the dynamical change of surface geometry, we selected three components of each dimer's degrees of freedom to be observed during a dynamical evolution of the surface: the dimer bond length, the dimer angle, and the dimer center of mass (CM) height. During the simulation time of 80 fsec, sixteen surface dimers already show quite complicated microscopic processes of the surface dynamics. Each dimer shows different degree of dynamical change of the dimer configuration from from the other dimers, but as a whole the three components of a dimer geometry shows oscillating behaviors.

The bond length typically changes about 10%, and Figure 8-1 shows an oscillation of the bond length for a surface dimer. The dimer angle also changes from the ground state value, and Figure 8-2 shows a dimer which is in the process of flipping from one asymmetric configuration to another asymmetric configuration.

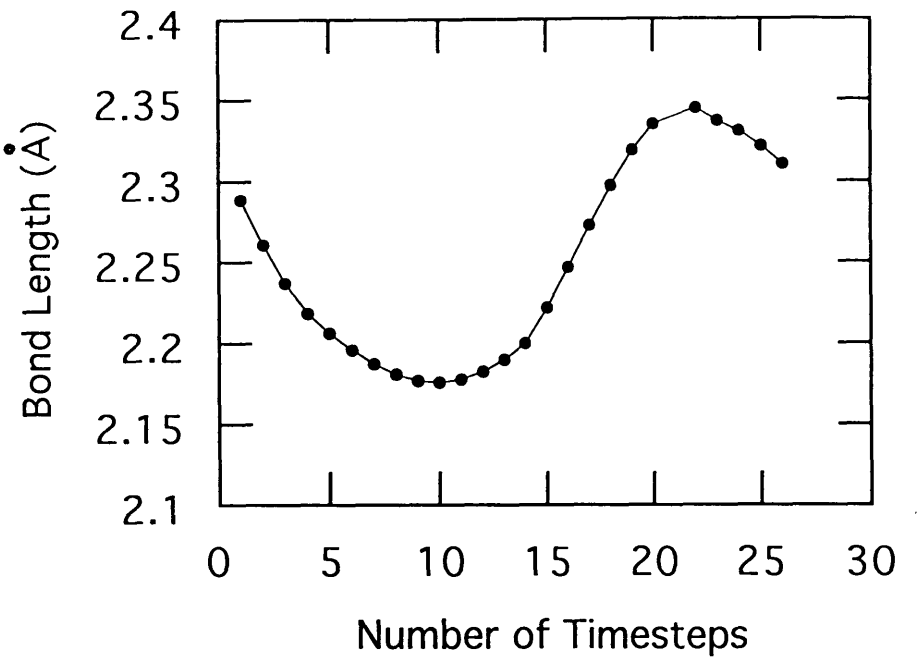

Figure 8-1: This plot shows the dynamical change of the bond length of a surface dimer for 25 timesteps ($\Delta t = 3.3 fsec$). The period of the oscillation is about 100 fsec.

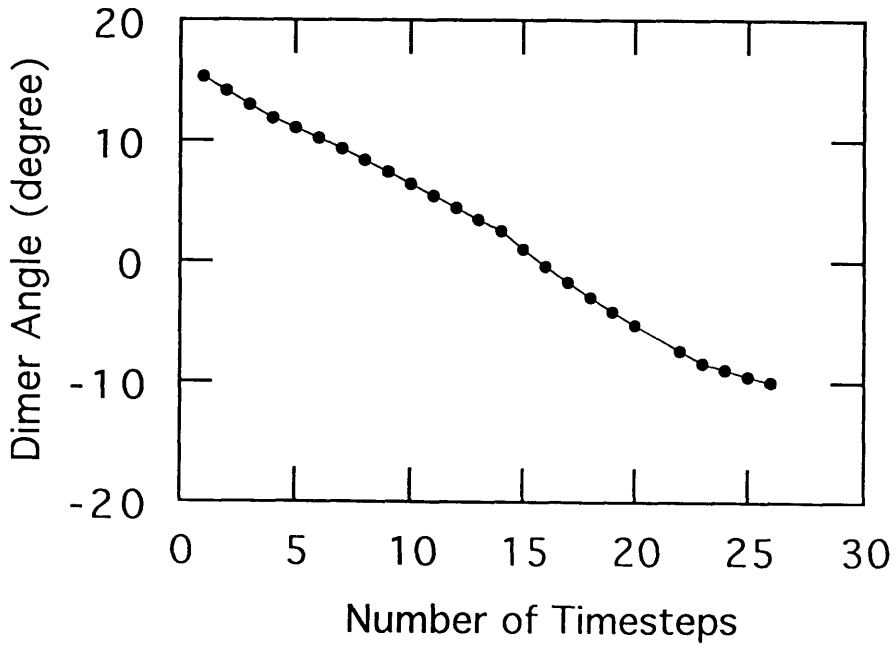

Figure 8-2: This plot shows the dynamical change of the buckling angle of a surface dimer for 25 timesteps ($\Delta t = 3.3 fsec$). The time scale of the dimer flipping corresponds to about 100 fsec.

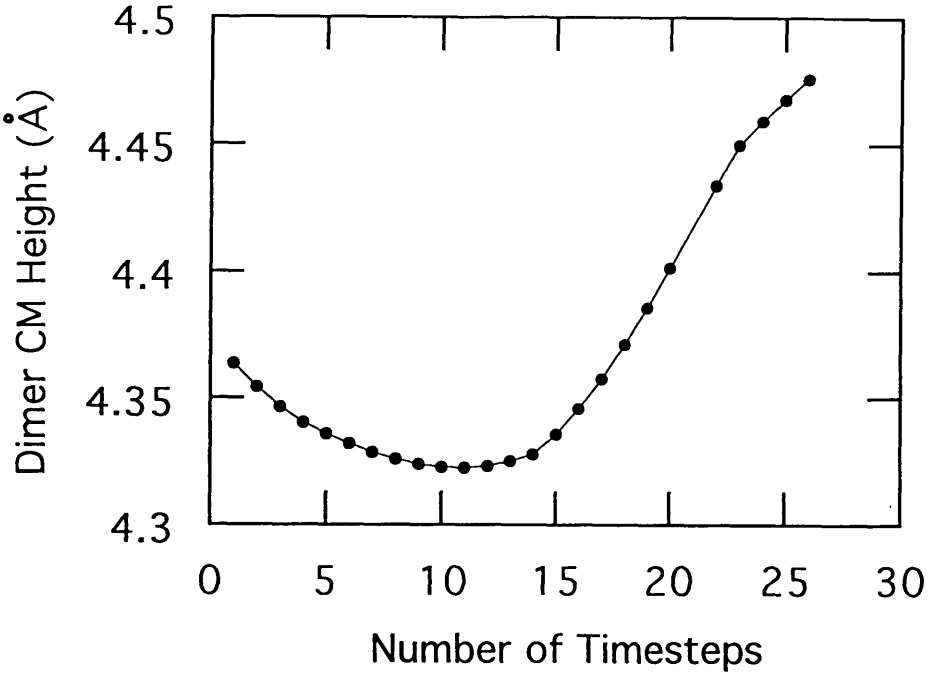

Figure 8-3: This plot shows the dynamical change of the center of mass height of a surface dimer for 25 timesteps ($\Delta t = 3.3 fsec$). The period of the oscillation corresponds about 100 fsec, and the oscillation amplitude is asymmetric with respect to the ground state value.

The dimer CM height shows an asymmetric oscillation around the the ground state value as illustrated for a surface dimer in Figure 8-3. The average dimer CM height over 16 surface dimers increases by 0.1Å, and this increase corresponds to a thermal expansion of the surface layer into the vacuum at finite temperature.

8.4 Dnamical Change of Surface Electronic Structure

As the surface atoms move as a function of time, the surface electronic structure changes correspondingly. This change is illustrated with the valence charge density cross section and the Kohn-sham eigenvalues as shown in Figure 8-4 and Figure 8-5.

Figure 8-4 shows a sequence of frames of the charge density cross section containing two surface dimers. The first frame clearly shows the covalent bonds of two

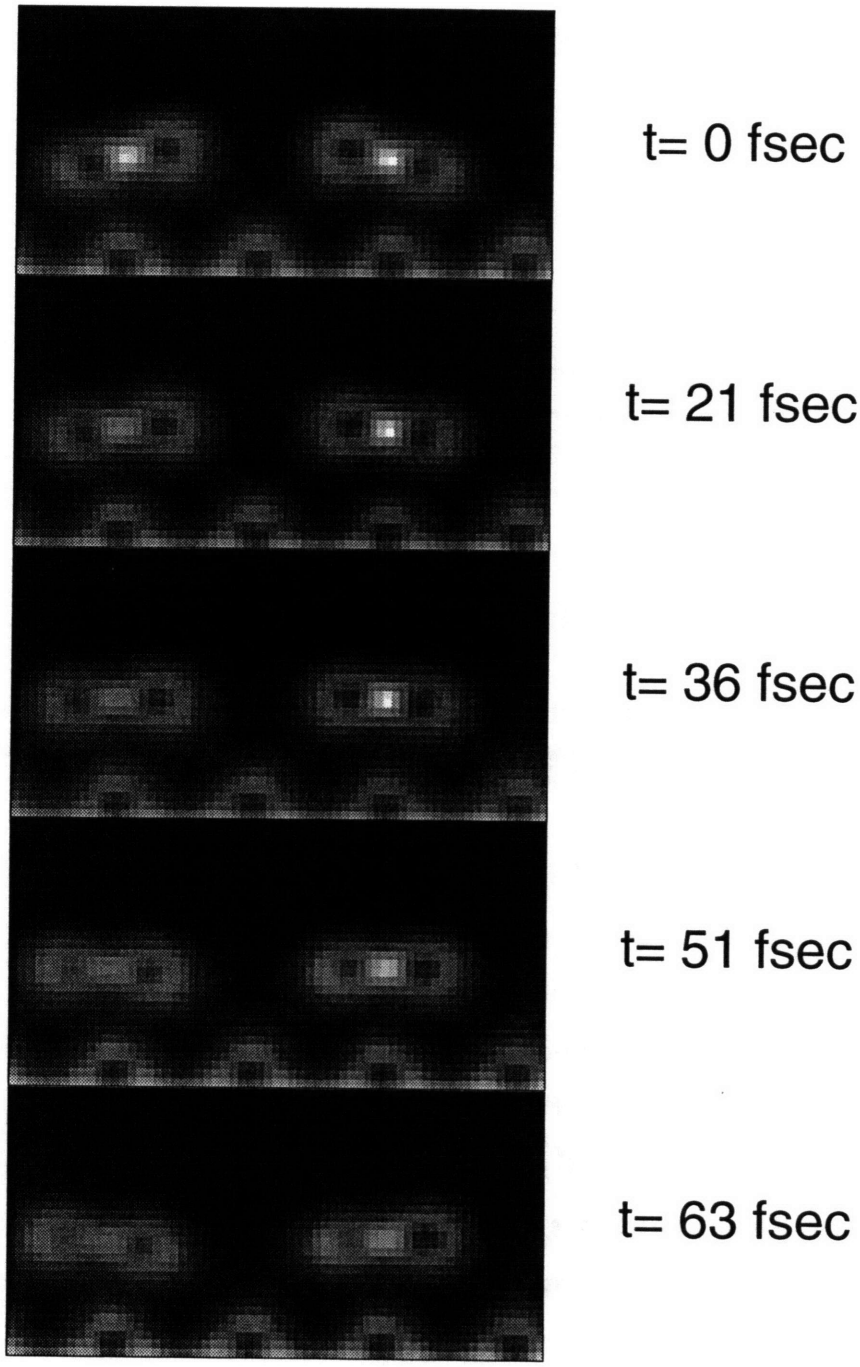

Figure 8-4: This plot shows a sequence of frames of the charge density cross section containing two surface dimers in gray scale. Small black dots within gray clouds are the core regions of the of the surface dimer atoms, and the white dots represent the covalent bonding charge density. Both dimers are in the process of flipping.

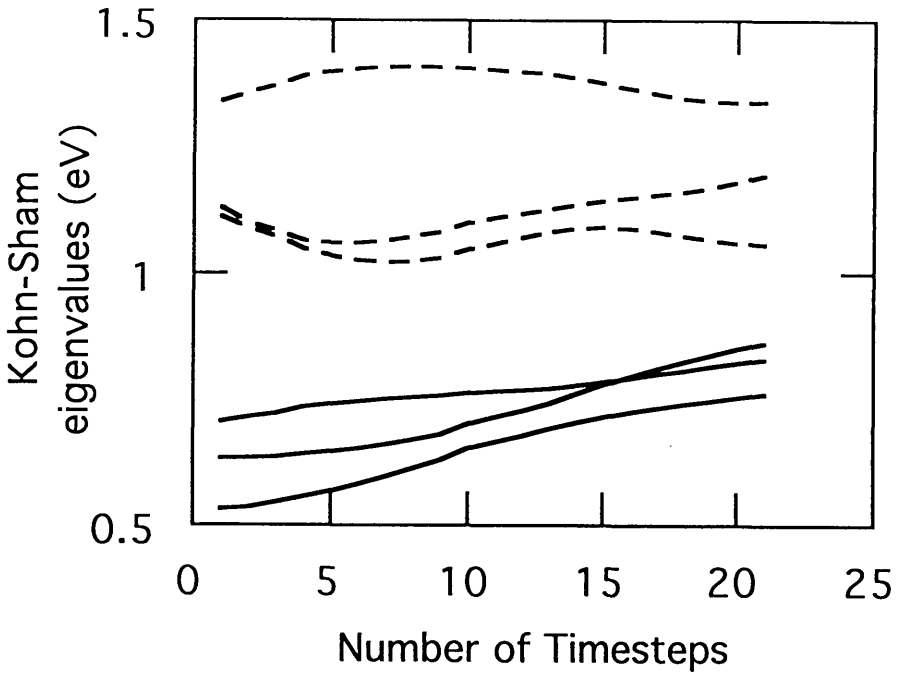

Figure 8-5: This plot shows the dynamical change of the Kohn-Sham eigenvalues of surface electronic states. The continuous lines are the occupied states, and the broken lines are the empty states.

asymmetric surface dimers, and the bonding charge distribution changes as the surface evolves dynamically. The left dimer shows that the bonding becomes weak as the dimer bond length increases, and the right dimer shows the weakening and the subsequent strengthening of the bonding. One can also see that both dimers are in the process of flipping as noted in Figure 8-2.

Figure 8-5 shows the dynamical change of the Kohn-Sham eigenvalues of surface electronic states. Three continuous lines are the occupied surface states, and three broken lines are the empty surface states. The change of eigenvalues shows that there are several different time scales, and the change can be as large as a few tenth of an eV. This change indicates that the surface chemical reactivity and the electronic transition properties (optical transitions and photoemission spectra) changes dynamically.

8.5 Concluding Remarks

Since the results shown in this chapter is only preliminary, further calculations will show more details of the microscopic dynamical changes of the surface structure. From the calculations with enough number of timesteps, we can calculate the surface phonon spectrum and the dynamical change of the surface electronic band structure, the surface reactivity, and the STM image.

Chapter 9

Vicinal Si(100) Surface under External Strain

The phase diagram of a vicinal Si(100) surface is calculated as a function of misorientation angle, temperature, and applied external strain. This work is generalizing the finite temperature phase diagram of vicinal Si(100) surfaces by introducing an applied external strain as an additional parameter. It is shown that a change of the applied external strain can drive the phase transition between the single layer step surface phase and the double layer step surface phase. The order parameter of the surface phase transition is also calculated to make it possible to measure the phase transition experimentally.

9.1 Introduction

When a Si crystal is cut by a plane slightly misoriented toward (011) direction from the (100) surface, the crystal surface accommodates the misorientation by generating low energy steps on the Si(100) surface. Consequently, a vicinal Si(100) surface consists of terraces separated by steps. There are two different single layer steps (SA and SB) and two different double layer steps (DA and DB) depending on the orientations of the dimers on the terraces separated by the step (Figure 9-1). The calculation of the energies of the steps [64] shows that the DB double layer step has the lowest

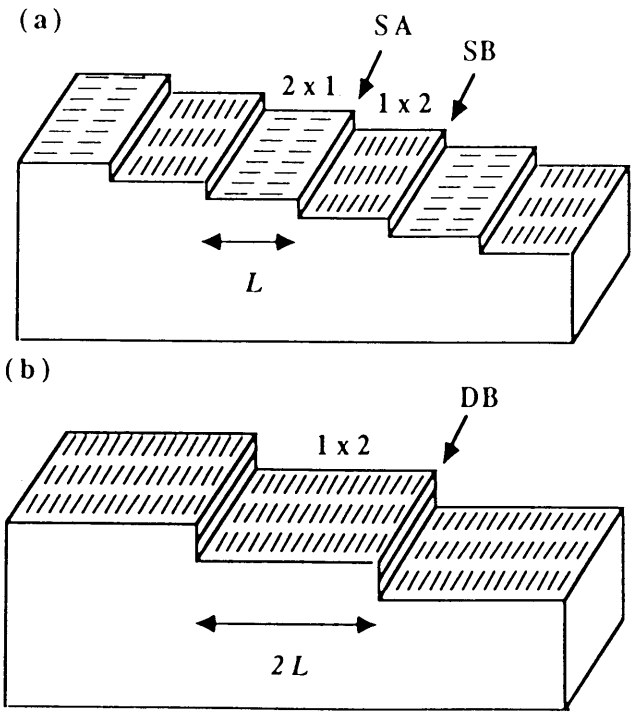

Figure 9-1: Schematic representation of the (a) single-layer and (b) double-layer structures of a vicinal Si(100) surface taken from [65].

energy so that the DB double layer step surface is the ground state structure at zero temperature.

However, when one includes the effect of the strain relaxation of the alternating (2×1) and (1×2) terraces of a single layer step surface, the single layer step surface becomes the lowest energy surface for a small misorientation angle ($\theta < \theta_c = 0.05$) at zero temperature [65, 66] since this strain relaxation does not exist for double layer step surfaces. Furthermore, at a finite temperature steps are not straight but fluctuating, and the fluctuations lower the step free energies. The SB step has the lowest energy of the kink generation, and consequently shows the largest fluctuation. The large fluctuation of the SB step lowers the surface free energy of the single layer step surface relative to the DB double layer step surface so that the critical angle θ_c increases as the temperature increases [66]. Therefore, the temperature vs misorientation angle phase diagram has two phase, DB double layer step surface and single layer step surface, divided by a first order phase transition line [66].

This temperature vs misorientation angle phase diagram of the vicinal Si(100) surface is studied both theoretically and experimentally [67, 68, 69, 70, 71]. These studies are focused on the nature of phase transition [68, 69, 70, 71] and the shape of the phase transition line [67]. A study shows that the phase transition may be much more complicated than a simple first order phase transition [69, 70].

However, one needs to consider the following facts about the temperature vs misorientation angle phase diagram. The approximation of the continuum elastic theory is used in the calculation of the strain relaxation. This approximation assumes that the distance between two steps on both sides of a terrace is much larger than the lattice constant. At a large misorientation angle where the average terrace width is small or at a high temperature where a large fluctuation of steps generates regions with small terrace width, this approximation is not valid. This approximation also affects the nature of the phase diagram as a whole because the approximation is valid only for small misorientation angles at low temperatures. Therefore, to determine the exact nature of the phase transition one needs to calculate the strain relaxation rigorously.

On the other hand, the experimental determination of the phase diagram presents the following problems. One is the problem of using different samples for different misorientation angles which makes it difficult to determine the θ dependence of the phase transition. Another is the problem of the kinetic constraint at a low temperature to adjust the surface configuration. As the temperature decreases, the surface might have the same structure below a certain temperature during the finite time of the experiment.

Finally, one cannot exclude the possibility of the roughening transition at a high temperature. The rough profile of the fluctuating steps can lead to the fluctuation of the terrace width. If this fluctuation of the terrace width diverges, the surface becomes rough and one cannot use the equations based on the constant average terrace width.

Therefore, when one considers the problems associated with the temperature vs misorientation angle phase diagram, the most significant and experimentally established property of the phase diagram is the existence of two different surface phases:

DB double layer step surface for a large misorientation angle at a low temperature; single layer step surface for a small misorientation angle at a high temperature.

In this paper, we calculate a more general phase diagram of the three dimensional parameter space: the misorientation angle θ, the temperature T, and the applied external strain ϵ. We calculate the free energies following the calculation of ref. 3, and we focus on the diverse structure of the phase diagram rather than on the exact nature of the phase transition. We discuss the possible phases of the surface and several two dimensional cross sections of the phase diagram.

9.2 Calculations

The Si(100) surface reconstructs by forming a regular array of surface dimers. A dimer is formed by combining two surface atoms so that it has a periodicity of 2×1 or 1×2 relative to the periodicity of the bulk Si depending on the plane where the crystal is cut. Therefore, the array of dimers can have two possible directions, and different directions are related by a 90 degree rotation. This direction defines two possible domains of a reconstructed surface.

One can cut the crystal along the plane which is slightly misoriented toward the [011] direction by an angle θ. For a small misorientation angle (less than a few degrees) the surface consists of domains of the Si(100) surface connected by single layer steps or double layer steps (Figure 9-1).

There are two single layer steps, SA and SB, and two double layer steps, DA and DB depending on the orientations of the two domains relative to the direction of the step between them. If one thinks only about the formation energies of these steps [64], then the surface with DB double layer steps is the lowest energy surface. However, one should consider two more things: the strain relaxation energy and the effect of temperature. When these effects are combined with the step formation energies, the single layer step surface can be the lowest energy surface depending on the misorientation angle and the temperature [66].

The phase diagram of the vicinal Si(100) surface can be generalized by introducing

an additional parameter such as an applied external strain. Now one can obtain different phases of the surface as a function of three parameters: the misorientation angle θ, the temperature T, and the applied external strain ϵ.

The free energy of a surface has three terms: the step energy, the renormalization of the step energy due to the roughening of the step at a finite temperature, and the strain energy. First, λ_{SA} and λ_{SB} are the energies per unit length for SA step and SB step. As a result, the step energy per unit area for a single step surface is:

$$E_{step}(L) = \frac{\lambda_{SA} + \lambda_{SB}}{2L}, \tag{9.1}$$

where L is related to θ by $tan(\theta) = 1.36\mathring{A}/L$ ($1.36\mathring{A}$ is the height of a single layer step). λ_{DA} and λ_{DB} are the energies per unit length for DA step and DB step, and the step energy per unit area for a double step surface is $\lambda_{DA}/2L$ for a DA step surface and $\lambda_{DB}/2L$ for a DB step surface.

Second, the effect of thermal fluctuation of steps renormalizes the step energies. At a finite temperature a step is not straight but becomes rough by generating a lot of kinks. The degree of roughness depends on the energy needed to generate a kink for a given step. The SB step has the smallest kink formation energy, and so the SB step has the roughest profile. The roughening of the SB step is calculated by using the Hamiltonian of a one dimensional SOS (Solid On Solid) model [66]. The roughening of other steps are not included because of their small effect on the step energies. The free energy per unit length of the rough SB step is:

$$\lambda_{SB} - (k_B T)^{-1} ln Z_H, \tag{9.2}$$

where Z_H is the partition function of the one dimensional SOS model.

Third, the strain energy consists of two terms: the strain relaxation energy and the strain energy due to an applied external strain. For a single layer step surface the surface energy is lowered through the strain relaxation at the single layer steps (both SA step and SB step). The reconstructed surface has an anisotropic surface stress tensor: the stress tensor has a positive component $\sigma_{||}$ along the dimer direction

and a negative component $\sigma_\perp$ perpendicular to the dimer direction. For a single layer step surface two phases with perpendicular dimer directions alternate at each single layer step. This leads to the strain relaxation at the single layer steps. The strain relaxation energy per unit area is [65]:

$$E_{strain}(L) = L^{-1}\lambda_\sigma ln(\frac{L}{\pi a}cos\frac{\pi p}{2}), \tag{9.3}$$

where λ_σ is determined by surface stress anisotropy, and p is the fraction of increased domain due to an applied external strain (i.e. the alternating domains have unequal widths $(1+p)L$ and $(1-p)L$, respectively). On the other hand there is no strain relaxation for a double layer step surface.

The strain energy per unit area due to an applied external strain ϵ is $1/2\epsilon p(\sigma_{||}-\sigma_\perp)$ for a single layer step surface, $\epsilon\sigma_{||}$ for a DA double layer surface, and $\epsilon\sigma_\perp$ for a DB double layer surface.

Therefore, the free energies per unit area of three phases (single layer step, DA double layer step, and DB double layer step) of a surface are the following:

$$\begin{aligned} F_{SL}(L,T,\epsilon) &= \frac{\lambda_{SA}+\lambda_{SB}-(k_BT)^{-1}lnZ_H}{2L} - L^{-1}\lambda_\sigma ln(\frac{L}{\pi a}cos\frac{\pi p}{2}) \\ &\quad +1/2\epsilon p(\sigma_{||}-\sigma_\perp) \qquad (9.4) \\ F_{DA}(L,T,\epsilon) &= \frac{\lambda_{DA}}{2L}+\epsilon\sigma_{||} \qquad (9.5) \\ F_{DB}(L,T,\epsilon) &= \frac{\lambda_{DB}}{2L}+\epsilon\sigma_\perp. \qquad (9.6) \end{aligned}$$

Here the fraction p in the F_{SL} is determined by minimizing the strain energy with fixed L [65].

9.3 Phase Diagram and Order Parameter

The phase diagram in the three dimensional parameter space (θ, T, and ϵ) is determined in the following way: the surface free energies of three phases are calculated for a given set of θ, T, and ϵ; and the phase with the lowest free energy is chosen to

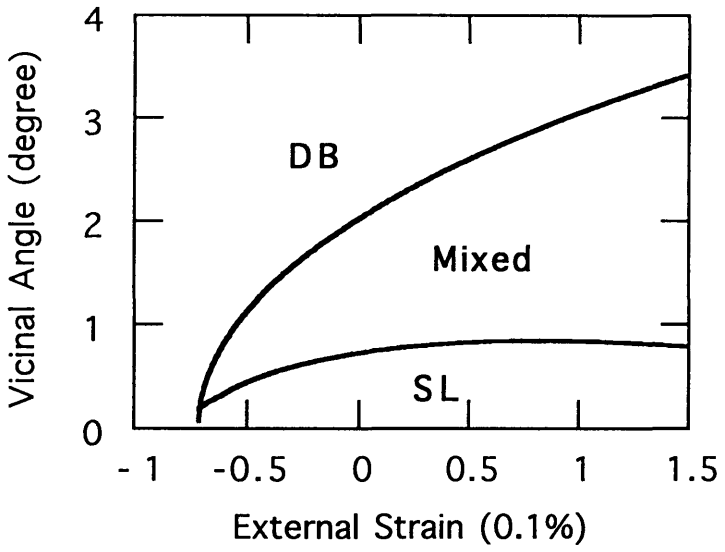

Figure 9-2: Phase diagram on the plane of the external strain and the vicinal angle. Three phases are indicated as DB, Mixed, and SL: the DB double layer step surface, the mixed layer surface phases, and the single layer surface.

be the phase of the given parameter set. As a result, the three dimensional paramter space is divided into three different phase regions: the single layer step surface phase, the DA double layer step surface phase, and the DB double layer step surface phase.

Figure 9-2 shows the phase diagram in the plane of the vicinal angle and the external strain. The three phases are separated by two first order phase transition surfaces. The intersection lines between $T = 0$ plane and the phase transition surfaces are the lines of critical angle, $\theta_c(\epsilon)$ and $\theta_{c'}(\epsilon)$.

The temperature dependence of the surface phase is very small for the temperature change from 0 K to 500 K, and at about 500 K the phase difference vanishes. This result agrees with the θ-T phase diagram of Pehlke and Tersoff [66], and consequently Figure 9-2 describes most of the distinct phases at $T < 500K$.

The order parameter of the surface phase is defined as the fraction of the increased domain, p. Figure 9-3 shows the order parameter as a function of the external strain at four vicinal angles (0.001°, 0.1°, 0.3°, and 0.5°). For a flat surface the external strain induces a discontinuous change of the order parameter, but as the vicinal angle increases the order parameter depends less sensitively to the external strain.

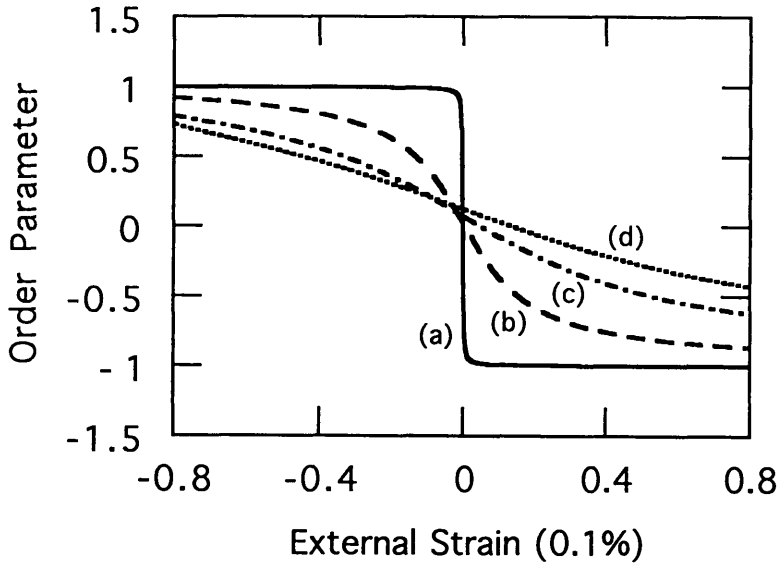

Figure 9-3: Plot of order parameter as a function of the external strain at vicinal angles (a) 0.001°, (b) 0.1°, (c) 0.3°, and (d) 0.5°.

Figure 9-4 shows the order parameter as a function of the vicinal angle at fixed external strains. The general trend is that the order parameter increases as the vicinal angle increases. However, at small vicinal angles the order parameter changes rapidly with the external strain.

Since the order parameter measures the relative fraction of two types surface terraces, it can be measured directly in a low energy electron diffraction (LEED) experiment.

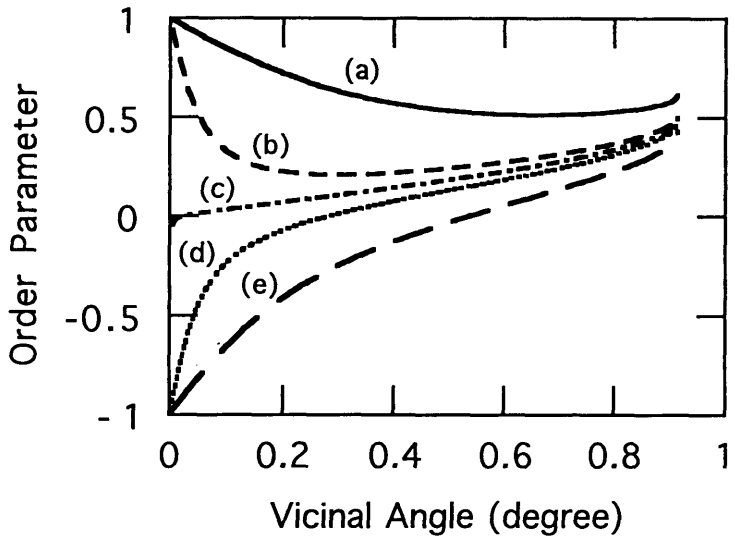

Figure 9-4: Plot of order parameter as a function of the vicinal angle at the external stain (a) -0.05%, (b) -0.01%, (c) 0%, (d) 0.01%, and (e) 0.05%.

Chapter 10

Ab initio Study of Si(113) Surface

Ab initio total energy calculations of Si(113) help resolve a long standing problem related to the unusual stability of this high index surface. It is found that the surface energy of the (3×1) reconstruction is considerably lower than both the surface energy of the (3×2) reconstruction and the minimum stabilization energy. These results are consistent with very recent high resolution STM and X-ray scattering measurements and predict that the observed stability of (3×1) is *intrinsic*.

10.1 Introduction

The high index crystal surfaces are generally unstable toward formation of low index facets. However, several stable high index surfaces are observed in many experiments, and specifically the Si(113) surface is observed to be *particularly* stable [72]-[76]. From the direct observation of the equilibrium shape of the silicon crystal, large facets of the Si(113) surface are clearly identified [72, 73], and this surprising stability has led to several experimental and theoretical attempts to understand the nature of this surface [74]-[82].

Early LEED measurements revealed that both (3×1) and (3×2) reconstructions could be observed on Si(113). More recent STM measurements also observe some domains with (3×1) and (3×2) symmetry on this surface. However, theoretical calculations using tight-binding methods on the (3×1) reconstruction [77] and *ab initio*

methods on the (3×2) reconstruction [80] indicate that both reconstructions have surprisingly large surface energies, in direct contradiction to the observed stability. To explain this problem, Bird *et al.* argued reasonably that the observed stability may be *extrinsically* induced by contaminants [80]. Most recent experiments have been able to isolate the (3×1) reconstruction as stable with the (3×2) as metastable [81].

In this work we have performed *ab initio* calculations on the (3×1) surface which reveal that in contrast to the early tight-binding calculations, it is considerably lower in energy than the (3×2) reconstruction. Moreover, the surface energy of the (3×1) reconstruction is found to be lower than the minimum stabilization surface energy! Furthermore, calculated surface energy ratios of Si(113) and Si(100) to Si(111) are found to be in quantitative agreement with experimental measurements. Thus, these theoretical results are consistent with the prediction that the (3×1) reconstruction is indeed the more stable geometry and that its stability is in fact *intrinsic*.

10.2 Calculations

The total energy pseudopotential density functional calculations are performed with the *ab initio* molecular-dynamics scheme implemented on Thinking Machines CM-2 and CM-5 [83, 84]. Within the local density approximation (LDA), the total energy is calculated using the Perdew-Zunger parameterized exchange-correlation energy [57] and the Kleinmann-Bylander separable form for the ionic pseudopotentials [58].

The supercell for the Si(113) surface calculation is chosen to include 140 silicon atoms with an inversion-symmetric geometry. This supercell contains a six bilayer slab with two (3×1) reconstruction units on each surface and a vacuum region of 12.5 Å. The supercell size is 12.74Å$\times$ 11.52Å$\times$ 30.00Å, and the corresponding Brillouin zone is sampled with the Γ point. The calculation uses a 10 Ry cutoff for the plane wave basis expansion corresponding to 15,360 basis functions, and the fast Fourier transform box size is $64 \times 64 \times 128$.

The ionic positions are initially assigned to maintain the bonding configuration of

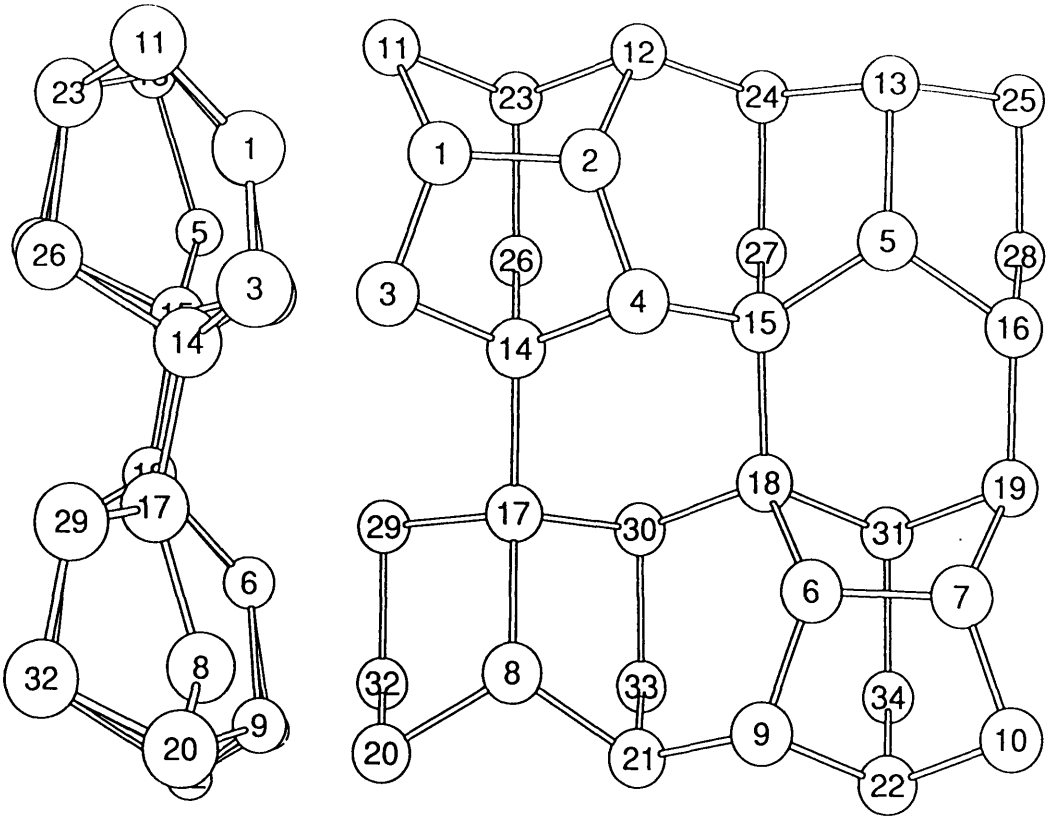

Figure 10-1: Ball and stick model representation of the relaxed geometry of the Si(113)-(3 × 1) surface. This plot shows only three surface layer atoms listed in Table 10.1. The left panel shows the side view of the surface, and the right panel shows the top view of he surface.

the (3 × 1) reconstructed Si(113) surface (Figure 10-1), and a geometric optimization is performed until the Hellmann-Feynman forces on the ions become smaller than 0.1 eV $Å^{-1}$. During this optimization, the innermost two layers are fixed in the bulk position. Figure 10-1 shows the ball and stick model representation of the optimized relaxed surface ion locations, and the Table 10.1 lists the ionic positions associated with the top three layers[1].

The surface energy is obtained from the difference between the energy of the surface system and the bulk system. For this purpose, the bulk silicon calculation is performed with an equivalent k-point sampling at 10 Ry cutoff energy. The calculated

[1]During the geometric optimization of the Si(113)-(3 × 1) reconstruction, no signature of a spontaneous change of the surface structure to a (3 × 2) reconstruction was found.

Table 10.1: This table lists the optimized ion locations as (X,Y,Z). X, Y, and Z are the fractions along the supercell vectors, $\vec{R_1}$, $\vec{R_2}$, and $\vec{R_3}$ where $\vec{R_1} = l_1(\frac{3}{\sqrt{11}}\hat{x} - \sqrt{\frac{2}{11}}\hat{z})$, $\vec{R_2} = l_2\hat{y}$, and $\vec{R_3} = l_3\hat{z}$. Here, $l_1 = 12.74$Å, $l_2 = 11.52$Å, and $l_3 = 30.00$Å are the supercell sizes, and $\hat{x}$, $\hat{y}$, and $\hat{z}$ are unit vectors along the crystal directions (110), ($\bar{1}$10), and (001) respectively. Because of the periodic boundary condition, an addition of integers to (X,Y,Z) represent the same ion in different supercell.

	Atom	X	Y	Z
First-layer	1	-0.248	-0.266	0.320
atoms	2	-0.243	-0.067	0.319
	3	-0.081	-0.332	0.323
	4	-0.069	-0.000	0.329
	5	-0.178	0.331	0.292
	6	0.253	0.234	0.319
	7	0.257	0.432	0.319
	8	0.322	-0.167	0.292
	9	0.422	0.168	0.325
	10	0.432	0.498	0.330
Second-layer	11	-0.427	-0.329	0.264
atoms	12	-0.423	-0.002	0.265
	13	-0.386	0.334	0.267
	14	-0.057	-0.165	0.286
	15	-0.095	0.163	0.280
	16	-0.095	0.499	0.278
	17	0.113	-0.166	0.267
	18	0.073	0.171	0.264
	19	0.075	0.496	0.264
	20	0.404	-0.337	0.280
	21	0.406	0.000	0.279
	22	0.440	0.335	0.285
Third-layer	23	-0.413	-0.167	0.219
atoms	24	-0.417	0.164	0.219
	25	-0.417	0.503	0.220
	26	-0.237	-0.165	0.208
	27	-0.254	0.164	0.202
	28	-0.255	0.507	0.201
	29	0.082	-0.335	0.220
	30	0.083	0.002	0.220
	31	0.084	0.333	0.218
	32	0.245	-0.336	0.202
	33	0.246	0.005	0.202
	34	0.261	0.335	0.207

Table 10.2: This table compares the calculated surface energies of the Si(111)-(7 × 7), the Si(100)-c(4 × 2), the Si(113)-(3 × 1), and the Si(113)-(3 × 2) surfaces. The unit is eV Å^{-2}.

Surface	*ab initio* calculation	Keating correction	surface energy
Si(111)-(7 × 7)	0.092	-0.003	0.089
Si(100)-c(4 × 2)	0.096	-0.001	0.095
Si(113)-(3 × 1)	0.094	0.000	0.094
Si(113)-(3 × 2) [80]	0.138		0.138

(3 × 1) Si(113) surface energy is found to be 0.094 eV Å^{-2}, and this energy is much lower than the (3 × 2) reconstructed surface energy of 0.138 eV Å^{-2} obtained using very similar techniques by Bird *et al.* [80].

To make contact with experimental measurements of the ratios of the surface energies of Si(113) and Si(100) to Si(111), we also performed ab initio total energy calculations for Si(100) using the following parameters. The supercell for the Si(100) surface contains 256 silicon atoms and its dimensions are 30.7Å× 15.4Å× 19.5Å. The silicon atoms form eight layers with inversion-symmetry, and the surface is reconstructed with c(4 × 2) symmetry. The calculated surface energy is 0.096 eV Å^{-2} for the Si(100) surface. The Si(111) surface energy is taken to be 0.092 eV Å^{-2}. This result is from the (7 × 7) reconstructed surface calculations of Brommer *et al.* [85] which use the same code.

To check the importance of including the relaxations of many layers of atoms below each surface and thereby improve the accuracy of the calculated surface energies, we performed a Keating correction for each system. The systems corresponding to the Si(113), Si(111), and Si(100) surfaces contain respectively 17, 12, and 16 additional bulk layers below the surface layers determined from the *ab initio* calculations. The resulting surface energy corrections were quite small as shown in Table 10.2.

Table 10.3: This table compares the calculated surface energy ratios with the experimentally determined ratios [73].

	$\gamma_{113}/\gamma_{111}$	$\gamma_{100}/\gamma_{111}$
Experiment	1.12	1.11
Calculation	1.06	1.07

10.3 Stability of the Si(113) Surface

The criterion for the stability of the Si(113) surface against the Si(100) and the Si(111) facets is determined by a simple geometric consideration as

$$\gamma_c = 0.522\gamma_{111} + 0.603\gamma_{100}. \tag{10.1}$$

Using the values of the Si(100) and Si(111) surface energies of Table 10.2, we find that $\gamma_c = 0.104$ eV Å^{-2}. Consequently, the Si(113) facet is 20 meV Å^{-2} more stable than the combination of Si(100) and Si(111) facets, and this will lead to a spontaneous formation of the Si(113) facet at the expense of Si(100) and Si(111) facets, as observed in many experiments. This result, therefore, finally accounts for the observed stability of the Si(113) facet and predicts that it is a purely *intrinsic* effect.

10.4 Equilibrium Shape Experiment

Recently, the ratios of the surface energies among many silicon surfaces have been determined [73] from equilibrium crystal shape experiment with: $\gamma_{113} = 1.12\gamma_{111}$ and $\gamma_{100} = 1.11\gamma_{111}$. These experiments reveal two salient features of the surface energies. First that γ_{113} and γ_{100} are nearly equal to each other, and second that they are about 10% larger than γ_{111}.

Our calculated ratios are $\gamma_{113} = 1.06\gamma_{111}$ and $\gamma_{100} = 1.07\gamma_{111}$ as summarized in Table 10.3 and in good quantitative agreement with the experimental measurements.

Chapter 11

Future Developments

The direction of my future research plan is closely related to the future developments of the computational science both in software and harware. As the more efficient algorithms and the faster supercomputers are developed, one can study more complicated and larger systems using the *first principles calculations.* My current research interests are both in the development of new techniques and the applications to larger systems. In addition to that, I plan to study the optoelectric properties of condensed matter systems.

11.1 New Techniques

I am currently testing a new projection technique for the molecular dynamics simulation. This technique is developed to overcome the difficulties of the force convergence in *ab initio* calculations[1]. I am also searching for a possibility of including the full two electron correlation in the density functional theory through the two electron orbitals[2]. My long term perspective is to implement the Dirac equation in the form of spin density functional theory to investigate heavy elements.

[1] In an *ab initio* calculation, the error in the total electronic energy is second order in the electronic wave function error, but the error in the forces on ions is first order. This error in force leads to a loss or gain of the total energy of the ionic system.

[2] This idea is similar to the spin density functional theory in which the electronic correlation leading to the magnetic instability of the electron system is included from the beginning.

11.2 Applications

The current computational capacity is increasing very fast and already powerful enough for large scale first principles calculations. To take advantage of this computational power, we started to study the Si(111)-(7 $\times$ 7) surface which has a large surface reconstruction unit with 47 unreconstructed units. This investigation focuses on the hydrogen adsorption on the surface, the self diffusion of silicon adatoms, the dynamical change of surface structures at finite temperature, and the adatom transfer between the tip and the surface. On the other hand, we started a preliminary research for a first principles study of biochemical systems. The ultimate goal of this research is to study the biochemical processes, and understand them from the first principles.

Another direction of applications is to understand more details of the microscopic processes of physical systems without requiring huge computational resources. One of them is to study the chemical shifts of the photoelectrons due to the relaxation of the surface electronic structure in the presence of a core hole. Another example is to calculate the electronic structures of quantum dots and quantum wires, and study the change of the electronic properties such as the dielectric constant due to the quantum confinement effects. One more example is to study the quantum chaotic behavior of the electronic structure using the *ab initio* dynamics simulations.

I am also planning to continue the investigation of the tip-surface system for the STM, the AFM, and the friction force microscopy (FFM).

Appendix A

Extended Hard-Sphere Potential System

In this appendix, we will give a rigorous proof that the ESM does not generate a canonical ensemble for a hard sphere (HS) potential system. We will also show that the temperature fluctuations do not agree with the canonical ensemble values even though the average temperature of the HS system agrees very well with T_{ext} of the ESM. This behavior of the average temperature comes from the fact that the instantaneous temperature of the HS system is dynamically controlled by the attached thermostat.

A dynamical system is not ergodic if there exists an additional conserved quantity to the total energy, the total momentum, and the total angular momentum. So we will prove the non-ergodicity by finding an additional conserved variable.

The ES Hamiltonian of a HS potential system is the following:

$$H_{ES}(\mathbf{r}_i, \mathbf{p}_i, s, P_s) = \sum_{i=1}^{N} \frac{\mathbf{p}_i^2}{2ms^2} + \phi_{HS}(\{\mathbf{r}_i\}) + \frac{P_s^2}{2Q} + gk_BT_{ext}ln(s).$$

From this Hamiltonian one obtains the following equations of motion:

$$\begin{aligned} \frac{d\mathbf{r}_i}{dt} &= \frac{\mathbf{p}_i}{ms^2} \\ \frac{d\mathbf{p}_i}{dt} &= -\nabla_i \phi_{HS}. \end{aligned}$$

By taking the product of these two equations and summing over i, one is led to

$$\frac{d}{dt}\sum_i \mathbf{p_i}^2 = -ms^2\frac{d}{dt}\phi_{HS} = 0.$$

Therefore, the sum of the square of momenta is conserved (note that this not the kinetic energy of the HS system) and the extended system is *not ergodic.*

To investigate the consequences of this we define K_0 as:

$$K_0 = \sum_{i=1}^{N}\frac{\mathbf{p}_i^2}{2m}$$

By using the two conserved quantities, ϕ_{HS} and K_0, the ES Hamiltonian can be transformed to a one dimensional potential well problem for s as follows:

$$E = \frac{K_0}{s^2} + \frac{P_s^2}{2Q} + gk_BT_{ext}ln(s)$$

The first and third terms of this equation can be combined into an effective potential so that

$$E = \frac{P_s^2}{2Q} + V_{eff}(s).$$

The effective potential, V_{eff}, is shown in Figure A-1. Therefore, s and the kinetic energy of the HS system, K_0/s^2, will oscillate periodically with time. The fluctuations of the kinetic energy (or temperature) of the HS system depend on the initial choice of s for a simulation and consequently will not agree with the canonical ensemble values in general.

Figure A-2 shows the behavior of the instantaneous temperature of the HS system as a function of time where T_{ext} is changed from 1.5 to 1 in the middle of the simulation. This figure shows that the average temperature agrees with T_{ext} and follows the change of T_{ext} immediately even though the system is not ergodic. This behavior of the temperature arises from the fact that the temperature is dynamically controlled as shown in equation (2.10) whether the extended system is ergodic or not.

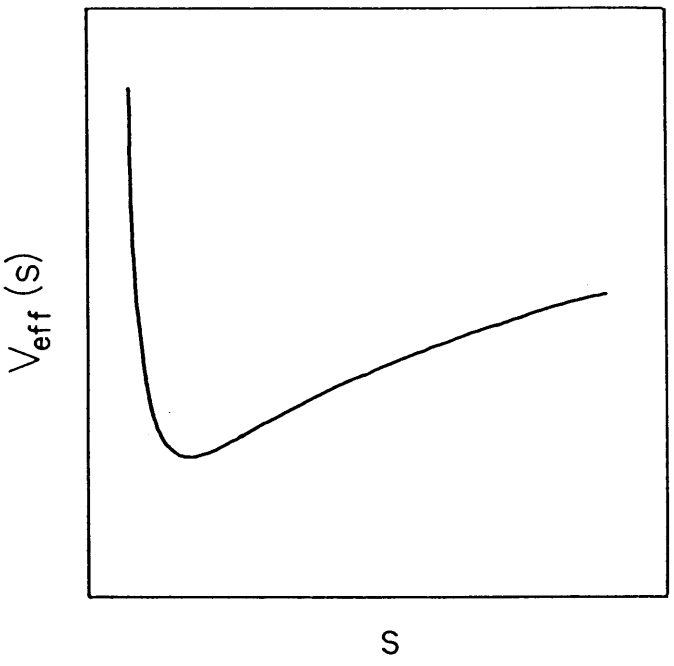

Figure A-1: The effective potential, $V_{eff}(s)$, for a HS potential system.

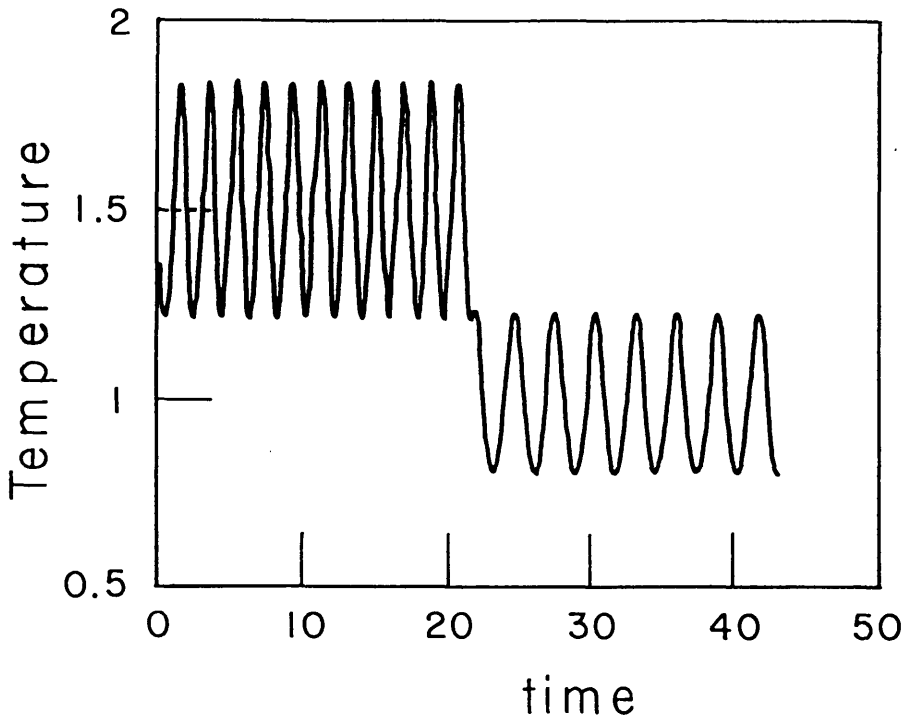

Figure A-2: The instantaneous temperature of a HS system as a function of simulation time. $Q = 1$ and T_{ext} changes from 1.5 to 1 in the middle of the simulation. The units are the reduced units of a LJ system.

Bibliography

[1] M. P. Allen and D. J. Tildesley, *Computer Simulation of Liquids* (Clarendon, New York, 1987).

[2] M. C. Payne, M. P. Teter, D. C. Allan, T. A. Arias, and J. D. Joannopoulos, Rev. Mod. Phys. **64**, 1045 (1992).

[3] J. D. Joannopoulos, R. D. Meade, and J. Winn, *Photonic Crystals* (to be published).

[4] W. H. Press, S. A. Teukolsky, W. T. Vetterling, and B. P. Flannery, *Numerical Recipes* 2nd Ed. (Cambridge University, London, 1989).

[5] K. Cho and J. D. Joannopoulos, Phys. Rev. A **45**, 7089 (1992).

[6] K. Cho and J. D. Joannopoulos, Telluride Summer Research Center Report (1991).

[7] K. Cho, J. D. Joannopoulos, and Leonard Kleinman, Phys. Rev. E **47**, 3145 (1993).

[8] K. Cho, T. A. Arias, J. D. Joannopoulos, and Pui K. Lam, Phys. Rev. Lett. **71**, 1808 (1993).

[9] T. A. Arias, K. Cho, J. D. Joannopoulos, Pui K. Lam, and M. P. Teter, Proceedings of Mardi Gras Conference on Teraflop Computation (1994).

[10] A. Devenyi, K. Cho, T. A. Arias, and J. D. Joannopoulos, Phys. Rev. B (May 15, 1994).

[11] R. Capaz, K. Cho, and J. D. Joannopoulos, to be published in Phys. Rev. Lett.

[12] K. Cho and S.-J. Oh, Phys. Rev. B **39**, 9576 (1989).

[14] K. Cho, M.Sc. Thesis, Seoul National University (1988).

[15] K. Cho and J. D. Joannopoulos, review article in Int. J. Mod. Phys. **B** (1994).

[16] K. Cho and J. D. Joannopoulos, review article in Scanning Microscopy (1994).

[17] K. Cho and J. D. Joannopoulos, Proceedings of Mardi Gras Conference on Teraflop Computation (1994).

[18] K. Cho and J. D. Joannopoulos, Phys. Rev. Lett. **71**, 1387 (1993).

[19] K. Cho and J. D. Joannopoulos, to be published in Phys. Rev. Lett.

[20] K. Cho and J. D. Joannopoulos, to be published in Science.

[21] K. Cho and J. D. Joannopoulos, U.S. Patent (applied in 1994).

[22] K. Cho and J. D. Joannopoulos (to be published).

[23] K. Cho. R. D. Meade, J. D. Joannopoulos, and O. L. Alerhand, to be published in Phys. Rev. B.

[24] K. Cho and J. D. Joannopoulos, to be published in Phys. Rev. Lett.

[25] Wm. G. Hoover, *Molecular Dynamics* (Springer-Verlag, Berlin, 1986).

[26] F. F. Abraham, Adv. Phys. **35**, 1 (1986).

[27] D. J. Evans and G. P. Morriss, Chem. Phys. **77**, 63 (1983).

[28] D. J. Evans *et al.*, Phys. Rev. A **28**, 1016 (1983).

[29] G. Ciccotti and A. Tenenbaum, J. Stat. Phys. **23**, 767 (1980).

[30] H. C. Anderson, J. Chem. Phys. **72**, 2384 (1980).

[31] M. Parrinello and A. Rahman, J. Appl. Phys. **52**, 7182 (1981).

[32] S. Nosé, J. Chem. Phys. **81**, 511 (1984).

[33] S. Nosé, Mol. Phys. **52**, 255 (1984).

[34] S. Nosé, Prog. Theo. Phys. Suppl. **103**, 1 (1991).

[35] Wm. G. Hoover, Phys. Rev. A **31**, 1695 (1985).

[36] A. Bulgac and D. Kusnezov, Phys. Rev. A **42**, 5045 (1990).

[37] S. M. Kay and S. L. Marple, Jr., Proc. IEEE, **69**, 1380 (1981).

[38] Duane C. Wallace and Galen K. Straub, Phys. Rev. A **27**, 2201 (1983).

[39] see *e.g.* Ingrid Daubechies, *Ten Lectures on Wavelets* (SIAM, Philadelphia, 1992), and references therein.

[40] Charles K. Chui, *An Introduction to Wavelets* (Academic Press, Boston, 1992).

[41] *Wavelets: A Tutorial in Theory and Applications*, edited by Charles K. Chui (Academic Press, Boston, 1992).

[42] *Wavelets and their Applications*, edited by M. B. Ruskai *et al.* (Jones and Bartlett, Boston, 1992).

[43] P. Pulay, Mol. Phys. **17**, 197 (1969).

[44] J. Stoer and R. Bullirsch, *Introduction to Numerical Analysis* (Springer-Verlag, New York, 1980).

[45] D. R. Bates, K. Ledsham, and A. L. Stewart, Phil. Trans. Roy. Soc. London **246**, 215 (1953).

[46] W. J. Hehre, L. Radom, P. v.R. Schleyer, and J. A. Pople, *Ab initio Molecular Orbital Theory* (John Wiley and Sons, New York, 1986).

[47] G. Binnig and H. Rohrer, Phys. Rev. Lett. **49**, 57 (1982).

[48] J. Tersoff and D. R. Hamman, Phys. Rev. Lett. **50**, 1998 (1983).

[49] C. Julian Chen, Phys. Rev. Lett. **65**, 448 (1990).

[50] H. Kageshima and M. Tsukada, Phys. Rev. B **46**, 6928 (1992).

[51] R. M. Tromp, R. J. Hamers, and J. E. Demuth, Phys. Rev. Lett. **55**, 1303 (1985).

[52] R. J. Hamers, R. M. Tromp, and J. E. Demuth, Phys. Rev. B **34**, 5343 (1986).

[53] Robert A. Wolkow, Phys. Rev. Lett. **68**, 2636 (1992).

[54] D. J. Chadi, Phys. Rev. Lett. **43**, 43 (1979).

[55] J. Ihm, D. H. Lee, J. D. Joannopoulos, and J. J. Xiong, Phys. Rev. Lett. **51**, 1872 (1983).

[56] Jaroslaw Dabrowski and Matthias Scheffler, Appl. Surf. Sci. **56-58**, 15 (1992).

[57] J. P. Perdew and Alex Zunger, Phys. Rev. B **23**, 5048 (1981).

[58] Leonard Kleinman and D. M. Bylander, Phys. Rev. Lett. **48**, 1425 (1982).

[59] Andrew M. Rappe, Karin M. Rabe, Efthimios Kaxiras, and J. D. Joannopoulos, Phys. Rev. B **41**, 1227 (1990).

[60] H. J. Kreuzer, L. C. Wang, and N. D. Lang, Phys. Rev. B **45**, 12050 (1992).

[61] Z.-H. Huang, M. Weimer, R. E. Allen, and H. Lim, J. Vac. Sci. Technol. A **10**, 974 (1992).

[62] G. Binnig, C. F. Quate, and Ch. Gerber, Phys. Rev. Lett. **56**, 930 (1986).

[63] D. Tománek, G. Overney, H. Miyazaki, S. D. Mahanti, and H. J. Güntherrodt, Phys. Rev. Lett. **63**, 876 (1989).

[64] D. J. Chadi,Phys. Rev. Lett. **59**, 1691 (1987).

[65] O. L. Alerhand, David Vanderbilt, Robert D. Meade, and J. D. Joannopoulos, Phys. Rev. Lett. **61**, 1973 (1988).

[66] O. L. Alerhand, A. Nihat Berker, J. D. Joannopoulos, David Vanderbilt, R. J. Hamers, and J. E. Demuth, Phys. Rev. Lett. **64**, 2406 (1990).

[67] Tze Wing Poon, Sidney Yip, Paul S. Ho, and Farid F. Abraham, Phys. Rev. Lett. **65**, 2161 (1990).

[68] X. Tong and P. A. Bennett, Phys. Rev. Lett. **67**, 101 (1991).

[69] E. Pehlke and J. Tersoff, Phys. Rev. Lett. **67**, 465 (1991).

[70] E. Pehlke and J. Tersoff, Phys. Rev. Lett. **67**, 1290 (1991).

[71] J. J. de Miguel, C. E. Aumann, R. Kariotis, and M. G. Lagally, Phys. Rev. Lett. **67**, 2830 (1991).

[72] J. M. Gibson, M. L. McDonald, and F. C. Unterwald, Phys. Rev. Lett. **55**, 1765 (1985).

[73] D. J. Eaglesham, A. E. White, L. C. Feldman, N. Moriya, and D. C. Jaconson, Phys. Rev. Lett. **70**, 1643 (1993).

[74] B. Z. Olshanetsky and V. I. Mashanov, Surf. Sci. **111**, 414 (1981).

[75] U. Myler and K. Jacobi, Surf. Sci. **220**, 353 (1989).

[76] Yu-Nong Yang and Ellen D. Williams, J. Vac. Sci. Technol. A **8**, 2481 (1990).

[77] D. J. Chadi, Phys. Rev. B **29**, 785 (1984).

[78] W. Ranke, Phys. Rev. B **41**, 5243 (1990).

[79] J. Knall, J. B. Pethica, J. D. Todd, and J. H. Willson, Phys. Rev. Lett. **66**, 1733 (1991).

[80] D. M. Bird, L. J. Clarke, R. D. King-Smith, M. C. Payne, I. Stich, and A. P. Sutton, Phys. Rev. Lett. **69**, 3785 (1992).

[81] M. J. Hadley, S. P. Tear, B. Röttger, and H. Neddermeyer, Surf. Sci. **280**, 258 (1993).

[82] D. L. Abernathy, Ph. D. thesis, MIT, 1993 (unpublished).

[83] R. Car and M. Parrinello, Phys. Rev. Lett. **55**, 2471 (1985).

[84] K. D. Brommer, B. E. Larson, M. Needels, and J. D. Joannopoulos, Computers in Physics **7**, 350 (1993).

[85] K. D. Brommer, M. Needels, B. E. Larson, and J. D. Joannopoulos, Phys. Rev. Lett. **68**, 1355 (1992).

Biographical Note

I was born in 1963 in Seoul, Korea. I had my undergraduate training at the Physics Department of Seoul National University from 1982 to 1986. This training was focused on the mathematical formulations, and the curriculum provided a general overview of practically all areas of physics. For the undergraduate thesis, I have studied the electronic structure of amorphous materials. The thesis was on how the two level states change the heat capacity of the amorphous materials. After graduation I entered the M.Sc. program at the Physics Department of Seoul National University in 1988, and joined the experimental research group of Professor S.-J. Oh. During the master thesis work, I joined the installation of the surface X-ray photoemission spectroscope, and gained familiarity with the experimental procedures and data processings. For the master thesis, I have combined the experimental, theoretical, and computational works. A part of the master thesis was published in *Physical Review B* in 1989.

After studying six years at Seoul National University, I have decided to go abroad to expand the range of my experience. I entered Massachusetts Institute of Technology in 1988, and after one semester I began to work with Professor Kerson Huang on the topological excitations in a confined 3-dimensional superfluid. After working with him for one year and working with Professor Patrick A. Lee for one semester, I decided to work with Professor John D. Joannopoulos for my PhD degree, and joined his research group in 1990. During my doctoral thesis research, I gained a diverse experience in computational science and engineering. I learned several programming languages and a lot of programing skills for different supercomputers including Cray vector supercomputers, Thinking Machines parallel supercomputers CM-2 and CM-5, and nCube. I also gained much understanding of the microscopic processes of condensed matter systems.

Publication List

1. K. Cho, M.Sc. Thesis, Seoul National University (1988).

2. K. Cho and S.-J. Oh, '$M_{4,5}N_{4,5}X$ Auger line shapes of La compounds from one-step model calculations', Phys. Rev. B **39**, 9576 (1989).

3. K. Cho and J. D. Joannopoulos, 'Ergodicity and Dynamical Properties of Constant Temperature MD', Telluride Summer Research Center Report (1991).

4. K. Cho and J. D. Joannopoulos, 'Ergodicity and dynamical properties of constant-temperature molecular dynamics',Phys. Rev. A **45**, 7089 (1992).

5. K. Cho, J. D. Joannopoulos, and Leonard Kleinman, 'Constant-temperature molecular dynamics with momentum conservation', Phys. Rev. E **47**, 3145 (1993).

6. K. Cho and J. D. Joannopoulos, 'Tip-Surface Interactions in Scanning Tunneling Microscopy', Phys. Rev. Lett. **71**, 1387 (1993).

7. K. Cho, T. A. Arias, J. D. Joannopoulos, and Pui K. Lam, 'Wavelets in Electronic Structure Calculations', Phys. Rev. Lett. **71**, 1808 (1993).

8. A. Devenyi, K. Cho, T. A. Arias, and J. D. Joannopoulos, 'Adaptive Riemannian metric for all-electron calculations', Phys. Rev. B (May 15, 1994).

9. K. Cho and J. D. Joannopoulos, 'The Devilish World of Surfaces', Proceedings of Mardi Gras Conference on Teraflop Computation (1994).

10. T. A. Arias, K. Cho, J. D. Joannopoulos, Pui K. Lam, and M. P. Teter, 'Wavelet-Transform Representation of the Electronic Structure of Materials', Proceedings of Mardi Gras Conference on Teraflop Computation (1994).

11. K. Cho and J. D. Joannopoulos, 'Ab initio Theory of STM and AFM', review article in Int. J. Mod. Phys. **B** (1994).

12. K. Cho and J. D. Joannopoulos, 'Tip-induced Modifications in STM and AFM', review article in Scanning Microscopy (1994).

13. K. Cho and J. D. Joannopoulos, 'Ultra-High Density Dimer Memory Device', U.S. Patent (applied in 1994).

14. K. Cho and J. D. Joannopoulos, 'Ab initio Study of Si(113) Surface', Phys. Rev. Lett. (submitted Apr. 6, 1994).

15. K. Cho and J. D. Joannopoulos, 'Microplastic Deformations in AFM', to be published in Science.

16. K. Cho and J. D. Joannopoulos, 'Mechanical Hysteresis on Atomic Scale', to be published in Phys. Rev. Lett.

17. K. Cho. R. D. Meade, J. D. Joannopoulos, and O. L. Alerhand, 'Vicinal Si(100)

Surface under External Strain', to be published in Phys. Rev. B.